TECHNISCHE UNIVERSITÄT MÜNCHEN

Fakultät für Maschinenwesen

Lehrstuhl für Flugsystemdynamik

Total System Performance of GBAS-based Automatic Landings

Dipl.-Tech. Math. Univ.

Michael Felux

Vollständiger Abdruck der von der Fakultät für Maschinenwesen der Technischen Universität München zur Erlangung des akademischen Grades eines

Doktor-Ingenieurs (Dr.-Ing.)

genehmigten Dissertation.

Vorsitzender:	Prof. Dr.-Ing. Oskar J. Haidn
Prüfer der Dissertation:	1. Prof. Dr.-Ing. Florian Holzapfel
	2. Prof. Jiyun Lee, Ph.D. Korea Advanced Institute of Science and Technology, Daejeon, Republic of Korea

Die Dissertation wurde am 21.02.2018 bei der Technischen Universität München eingereicht und durch die Fakultät für Maschinenwesen am 25.07.2018 angenommen.

TU München

Michael Felux

Acknowledgements

First of all, I would like to thank Florian Holzapfel for his continuous support and his very motivating way of supervising this thesis. Even though I was not working at the Institute of Flight System Dynamics at the TUM, he was always available for discussions about my work and progress and kept supporting my efforts. It was a great pleasure working with him!

Next, I would like to thank Jiyun Lee for her very helpful co-supervision of this work. Despite the long distance between Munich and Daejeon, she kept giving very helpful advice concerning my research and supported me in an excellent way throughout the work.

I conducted the research and produced this thesis while working at the German Aerospace Center's Institute of Communications and Navigation. I would like to thank the head of the Institute Prof. Günther, as well as the head of the Navigation Department, Prof. Meurer, for the opportunity to do the research presented in this thesis and their continuous support of my work. I furthermore want to thank my colleagues Simona Circiu, Gertjan Looye, Fabian Morschek, Thomas Dautermann, Thomas Ludwig, Hayung Becker, Robert Geister and Markus Rippl, for their direct help, guidance and support to this work and all my other colleagues at DLR for all the fruitful discussions and inspiration and great time at work.

Finally, I want to thank my whole family, especially of course my parents as well as my wife Gosia for their continuous support over all the years!

KURZFASSUNG

Diese Arbeit untersucht automatische Landungen von Flugzeugen, basierend auf Navigationssignalen von globalen Satellitennavigationssystemen (GNSS), welche durch ein bodengestütztes Augmentierungssystem (GBAS) korrigiert werden. Durch die Betrachtung von verfügbaren Informationen, in Verbindung mit einer realistischeren Modellierung werden Verbesserungsvorschläge für GBAS gemacht, welche das Potential haben die Verfügbarkeit des Dienstes zu erhöhen.

Zunächst werden hierfür das Instrumentenlandesystem (ILS) als derzeitiges Standard-System für die Führung von Luftfahrzeugen im Landeanflug und das GBAS als künftiges Führungssystem beschrieben und auf die Genauigkeit der Anflugführung im Flugversuch hin verglichen. Die Ergebnisse zeigen, dass GBAS ein deutlich weniger störanfälligeres, weniger verrauschtes und präziseres Führungssignal zur Verfügung stellt, als dasjenige des ILS.

Als nächstes wird die Ableitung von Anforderungen an ein Landesystem für Flugzeuge diskutiert. Die erlaubte Gesamtunsicherheit im Hinblick auf den Aufsetzpunkt des Flugzeugs ist dabei aufzuteilen auf einen Anteil des Autopiloten und einen Anteil des Navigationssystems. Dieser Prozess wird kritisch begutachtet und Verbesserungen vorgeschlagen, wo es möglich ist konservative Annahmen durch in Echtzeit verfügbare Informationen zu ersetzen. So können die Anforderungen an die GBAS Monitore reduziert und damit die Verfügbarkeit des Dienstes erhöht werden.

Als nächstes folgt eine Untersuchung der Verteilung der Aufsetzpunkte bei automatischen Landungen. Diese Untersuchungen werden exemplarisch anhand eines Simulationsmodells durchgeführt. Die Ergebnisse zeigen, dass eine Modellierung des Aufsetzverhaltens als Normalverteilung nicht gut geeignet ist. Entweder ist eine konservative Abschätzung vorzunehmen, um das Risiko außerhalb des erlaubten Bereiches auf der Bahn aufzusetzen nicht zu unterschätzen. Alternativ wird die Modellierung mittels einer Johnson-Verteilung untersucht, welche eine deutlich realistischere und weniger konservative Beschreibung des Aufsetzverhaltens zulässt.

Schließlich wird noch der Einfluss des Navigationssystems auf den Gesamtfehler untersucht. Die größten potentiellen Fehler in differentieller Navigation können durch ionosphärische Störungen entstehen. Dieses Phänomen wird deshalb näher beschrieben und im Anschluss ein verbessertes Monitoring im Bodensystem entwickelt. Dieses basiert auf einem zusätzlichen Empfänger für das Monitoring und berücksichtigt die aktuelle Satellitengeometrie. Schließlich wird für zukünftige Zweifrequenz-Dienste noch ein Monitoring im Bordsystem entwickelt und diskutiert. Dieses verwendet Informationen, sowohl über die aktuelle Satellitenkonstellation, als auch über die Leistungsfähigkeit des Autopiloten und benötigt deshalb deutlich weniger konservative Annahmen als ein gegenwärtiges GBAS.

ABSTRACT

In this work, automatic landings of aircraft based on signals from Global Navigation Satellite Systems (GNSS), augmented by a Ground Based Augmentation System (GBAS), are investigated. By taking into account available knowledge that is currently not used and a more realistic modelling of the autoland performance several suggestions for improving GBAS are made.

After a short discussion of the Instrument Landing System (ILS) and GBAS a motivation for the use of GBAS is given by comparing the performance of both guidance systems in flight trials. The results show that GBAS is much less susceptible to disturbances and provides more precise and smoother guidance.

The next chapter continues with a description and a discussion of the derivation of navigation requirements for GBAS from the definition of a safe landing. The total error budged has to be split between the autopilot and the navigation system. A critical review of the derivation process proposes adjustments by taking into account available knowledge about the satellite geometry in order to reduce the monitoring requirements and thus increase system availability.

This discussion is followed by an investigation of the autoland performance based on one example autopilot implementation. The results show that the currently used way to model the touchdown performance by a Gaussian distribution is not well suited. Either very conservative inflation is necessary or the tail probability of landing outside the required touchdown zone may be significantly underestimated. It is therefore suggested to model the touchdown performance by a Johnson distribution, better fitting to the obtained results.

Finally, the contribution of the navigation system to the total system error is discussed. As the main concern in differential navigation techniques, such as GBAS, results from ionospheric disturbances these phenomena are discussed more in detail. For the GBAS ground system an improved ionospheric monitor is proposed, based on adding an additional reference receiver for monitoring purposes. Furthermore, an ionospheric monitor for future dual-frequency GBAS modes is developed. Such a monitor is necessary if positioning is to be done based on single frequency modes, which seems to be a very likely way forward. Shifting this monitoring task to the airborne system has the advantage that all knowledge about current navigation performance and autopilot performance for that specific aircraft type can be exploited, facilitating the ionospheric monitoring task significantly.

TABLE OF CONTENTS

LIST OF FIGURES

LIST OF TABLES

LIST OF SYMBOLS

Symbol	Latin capital	Units (where applicable)
$B(i, j)$	B-value for satellite i and receiver j	m
D_l , D_v	Lateral and vertical difference between position solution based on 30s and 100s smoothing (absolute value)	m
E_v	Vertical position error	m
$E_{monitor}$	Monitoring threshold for ionospheric monitor	m
E_r , E_{range}	(Pseudo-)Range error	m
F_{pp}	Vertical to slant projection factor	
G	Geometry matrix of line-of-sight vectors between user position and satellites and clock offset matrix	
GPA	Glide path angle	degrees
I	Ionospheric delay	m
$\tilde{I}$	Pseudo-ionospheric delay estimate in ionospheric monitor, specified by index (air: experienced at the aircraft; PRC: as calculated from the PRCs)	m
I_{air} , I_{PRC}	Ionospheric delay measures of the ionospheric monitor	m
I_{test}	Test statistic of the ionospheric monitor	m
K_{ffmd}	Fault-free missed detection multiplier	
K_{md}	Missed detection multiplier	
$M(i)$	Number of reference receivers tracking satellite i	
MDE	Minimum detectable error	m
N	Number of satellites	
N_R	Refractivity index	
NTDP	Nominal touch down point as distance behind runway threshold	m
P	Probability, further specified by index (fa: false alarm; fault: fault occurs; md: missed detection; UL: unsuccessful landing; UL|E_v: unsuccessful landing given vertical error E_v)	

Q	Q-function defined as $Q(x) = \frac{1}{\sqrt{2\pi}} \int_{-\infty}^{x} e^{\frac{t^2}{2}} dt$	
S	Weighted pseudoinverse of the Geometry and clock offset matrix transferred in approach coordinates	
T	Tropospheric delay	m
T_c	Commanded thrust	
TC	Tropospheric correction	m
$PRC_{s,\tau}$	Pseudorange correction, index s describes type (prel: preliminary, sca: smoothed and clock adjusted, tx: transmitted) and τ the smoothing time	m
RRC	Range-rate correction	m
V	Speed, further specified by index (app: approach; s: stall)	m/s
VAL	Vertical alert limit	m
VPL	Vertical protection level, index specifying type of protection level (eph: ephemeris, H0: fault-free, H1: single-fault)	m
W	Diagonal weighting matrix	

Symbol	**Latin lower case**	**Units (where applicable)**
b_{TGD}	Tim group delay	m
Δb_I	Differential ionospheric delay between two reference receivers	m
c	Speed of light, according to WGS84 specification $c = 2.99792458 \cdot 10^8$ m/s	m/s
d	Rectilinear deviation, index specifies direction (lat: lateral, vert: verical)	m
$d_{monitor}$	Distance between GBAS reference point and monitoring receiver	m
$\vec{e}$	Line of sight unit vector from reference receiver to satellite	
f	PDF of a Johnson distribution, index specifying type (SB: bounded; SL: log-normal; SU: unbounded)	
f_{L1}, f_{L5}	Carrier frequency of the L1/L5 signal	
g	Slope of ionospheric gradient (in wedge model)	mm/km
h	Height	m
h_0	Tropospheric scale height	m

k	Weighting/inflation factor	
Δn	Single difference of integer ambiguities in IGM	
p	Probability specified by index (fa: false alarm; iono: occurrence of ionospheric gradient; md: missed detection)	
$r_{i,j}$	Geometrical range between satellite i and receiver j	m
$\vec{r}$	Position vector of GBAS reference points in ECEF coordinate frame, index specifies point reference (GARP: GBAS azimuth reference point, GERP: GBAS elevation reference point, GRP: Guidance reference point)	
s	Test statistic of the IGM	m
$s_{x,y}$	Entry of the $\mathbf{S}$-matrix	
s_{vert}	Projection factor from pseudorange domain into vertical position domain in approach coordinates	
t_{rx}	Time, index specifies to object to which time applies (rx: receiver; SV: satellite; usr: user; zcount: time of correction applicability)	s
$\vec{u}$	Unit vector with origin at the LTP, index determining direction (lat: lateral direction, rw: runway direction, vert: vertical)	
v	Speed of ionospheric front (in wedge model)	m/s
v_{air}	Horizontal speed of aircraft	m/s
w	Width of ionospheric gradient (in wedge model)	m
x_{air}	Slant distance between aircraft and GBAS reference point	m
$\vec{x}$	Position vector in ECEF coordinates, index specifies to which object position applies	
$\mathbf{x}$	4-dimensional position and clock offset vector	
$\vec{x}_b$	Baseline vector between two reference receivers	
z	Gaussian distributed random variable (in Johnson distribution section)	

Symbol	**Greek capital**	**Units (where applicable)**
Φ	CDF of Gaussian distribution defined as $\Phi(x) = \int_{-\infty}^{x} \frac{1}{\sqrt{2\pi\sigma^2}} \exp\left(-\frac{(x-\mu)^2}{2\sigma^2}\right) dx$	

Symbol	Greek lower case	Units (where applicable)
α	Smoothing filter time constant $\alpha = 0.5s / \tau$	
α	Angular deviation, index specifies direction (lat: lateral, vert: vertical)	degrees
β	Squared ratio between the L1and L5 frequency	
δ	Parameter of Johnson distribution	
δ_T	Thrust setting	
ε	Residual errors	m
ϕ	Carrier-phase based range measurement	m
ϕ_c	Commanded roll angle	rad
$\Delta\phi$	Single difference of carrier phase measurements	m
γ	Parameter of Johnson distribution	
η	Measurement noise (in positioning)	m
η_c	Commanded elevator deflection (relating to flight controls)	
λ	Wave length of carrier frequency specified by the index (in the satellite navigation context), Parameter of Johnson distribution (in the context of FTE modelling by Johnson distribution)	m
μ	Mean value of Gaussian distribution	
θ	Satellite elevation angle	degrees
θ_c	Commanded pitch angle (relating to flight controls)	rad
ρ , $\hat{\rho}$	Pseudorange, smoothed pseudorange	m
σ	Standard deviation of Gaussian distribution, index determines application (B,j: B-value of receiver j; FTE: Flight technical error; GS: Glide slope error; GBAS: GBAS guidance error; i: uncertainty in pseudorange measurement towards satellite i; iono: ionospheric error; LOC: localizer error; n: refracractivity uncertainty; monitor: monitoring noise; NSE: navigation system error; overbound: overbounding distribution; pr,air: Pseudorange measurement in airborne system; pr,gnd: Pseudorange measurement in ground system; tropo: tropospheric error; TSE: Total system error; vert: vertical; vig: vertical ionospheric gradient)	
τ	Smoothing time constant	s
$\Delta\tau$	Differential receiver clock bias in IGM	s

ξ	Parameter of Johnson distribution	
ξ_c	Commanded aileron deflection (relating to flight controls)	
ψ_c	Commanded yaw angle	rad
ζ_c	Commanded rudder deflection (relating to flight controls)	

LIST OF ACRONYMS

AL	Alert Limit
APV	Approach with Vertical Guidance
ATM	Air Traffic Management
C/A	Coarse / Acquisition
CAS	Control Augmentation System
CAT	Approach Category
CCD	Code-Carrier Divergence
CDF	Cumulative Distribution Function
CG	Center of Gravity
CONUS	Contiguous United States
CORS	Continuously Operating Reference Stations
CS-AWO	Certification Specifications for All-Weather Operations
DA	Decision Altitude
DDM	Difference in Depth of Modulation
DH	Decision Height
DME	Distance Measuring Equipment
DSIGMA	Dual Solution Ionospheric Gradient Monitoring Algorithm
EASA	European Aviation Safety Agency
ECEF	Earth-Centered Earth-Fixed
EGNOS	European Geostationary Navigation Overlay Service
FAA	Federal Aviation Administration
FAS	Final Approach Segment
FTE	Flight Technical Error
GARP	GBAS Azimuth Reference Point
GAST	GBAS Approach Service Type
GBAS	Ground Based Augmentation System
GERP	GBAS Elevation Reference Point
Glonass	Globalnaya navigatsionnaya sputnikovaya sistema (russ.)

GLS	GBAS Landing System
GNSS	Global Navigation Satellite System(s)
GPA	Glide Path Angle
GPS	Global Positioning System
GRP	Guidance Reference Point
GS	Glide Slope
ICAO	International Civil Aviation Organization
IGM	Ionospheric Gradient Monitor
ILS	Instrument Landing System
INS	Inertial Navigation System
LAL	Lateral Alert Limit
LOC	Localizer
LOCA	Local Object Consideration Area
LPL	Lateral Protection Level
LTP	Landing Threshold Point
MAC	Mean Aerodynamic Chord
MDA	Minimum Decision Altitude
MDE	Minimum Detectable Error
MDH	Minimum Decision Height
METAR	METeorologic Aerodrome Report
MLA	Multipath-limiting Antenna
MLS	Microwave Landing System
MLW	Maximum Landing Weight
MMR	Multi-Mode Receiver
NDB	Non-directional Beacon
NextGen	Next Generation Air Transport System
NSE	Navigation System Error
NTDP	Nominal Touchdown Point
PBN	Performance Based Navigation
PDF	Probability Density Function
PL	Protection Level
PPD	Personal Privacy Device

PRC	Pseudorange Correction
PRN	Pseudo Random Number
QQ	Quantile-Quantile
RFI	Radio Frequency Interference
RMS	Root Mean Square
RRC	Range-Rate Correction
RVR	Runway Visual Range
SARPS	Standards And Recommended Practices
SAS	Stability Augmentation System
SB	Bounded System of Johnson distribution
SBAS	Space Based Augmentation System
SESAR	Single European Sky Aviation Research
SL	Log-normal System of Johnson distribution
SU	Unbounded System of Johnson distribution
TAP	Terminal Area Path
TC	Tropospheric Correction
TCP	Threshold Crossing Point
TEC	Total Electron Content
TECS	Total Energy Control System
TSE	Total System Error
UL	Unsuccessful Landing
US	United States
VAL	Vertical Alert Limit
VDB	VHF Data Broadcast
VHF	Very High Frequency
VOR	VHF Omnidirectional Ra
VPL	Vertical Protection Level
WAAS	Wide Area Augmentation System

1 INTRODUCTION AND OVERVIEW OF CONTRIBUTIONS

1.1 BACKGROUND OF THE WORK

Fast and reliable air transport of passengers and cargo has become essential for society as well as the economy. Different studies come to the conclusion that it is to be expected that air traffic will continue to grow at a rate of about 2-5% per year depending on the geographic region and economic development in that area [1], [2]. This is a challenging development in terms of airport and airspace capacity. Air traffic control sectors over central and north-western Europe in the area Frankfurt – Amsterdam – London are extremely busy and are operating near or at their capacity limit during most of the time already today. When low visibility conditions prevail, the capacity of airports is reduced due to increased spacing of arriving aircraft on the approach and during taxi operations on ground. The SESAR program in Europe and the NextGen program in the US are development programs for ATM solutions that ensure that the increase in air traffic can be handled and all safety targets are met. One key enabler in this context is the use of Global Navigation Satellite Systems (GNSS), such as the United States' (US) GPS constellation, as primary means of navigation. Compared to conventional navigation aids, a significantly increased navigation performance in terms of accuracy and integrity can be achieved using GNSS. This better performance is exploited by the performance based navigation (PBN) concept which allows for a more efficient use of the airspace. For different phases of flight different levels of performance are required. The most stringent performance requirements are in effect for guidance of aircraft on precision approaches and automatic landings. Currently, this task is accomplished mostly by the Instrument Landing System (ILS). However, it can only provide straight-in guidance, requires operational mitigation of signal distortions by significant spacing of the aircraft aligned on the approach and can only provide approaches at one predefined glide slope angle to one fixed aiming point on the runway. When using GNSS for precision approach guidance, some sort of augmentation of the signals is required to meet the performance requirements. For precision approaches with different visibility minima in the last phase of flight, Space Based Augmentation Systems (SBAS) like the US American Wide Area Augmentation System (WAAS) or the European Geostationary Navigation Over-

lay Service (EGNOS) are certified for use down to decision heights of 200 ft or 250 ft, respectively. Currently also certified for CAT-I operations (called GBAS Approach Service Type (GAST) C) and commercially available is the Ground Based Augmentation System (GBAS). A ground station with reference receivers at the airport provides locally relevant corrections and integrity parameters, together with a definition of the approach path to arriving aircraft. Since its first approval and commercial use in 2012 it has been developed to also support CAT-II/III operations and is the system of choice to replace the ILS in the future. Standards for the CAT-II/III capable service type (GAST D in GBAS terminology) were developed and agreed upon by the International Civil Aviation Organization (ICAO) at the end of 2016 and will be in effect from 2018 on [3]. While the system is currently only used for ILS-lookalike approaches extensive standardization effort is ongoing to be able to fully exploit the benefits of GBAS. Some of the potential benefits include increased and variable glide slope angles for noise abatement, multiple glide slope angles for wake vortex mitigation and thus less spacing of aircraft on the approach, multiple runway aiming points to minimize runway occupancy and taxi times and optimize separation to ultimately increase capacity of a runway, definition of curved approaches with vertical guidance and potentially in the future also support of automated taxi operations and precision departure guidance. All these benefits become possible because of the flexible way of defining reference paths for aircraft by waypoints, straight and curved segments and vertical profiles, while the ILS is physically limited to providing only one straight approach path for all aircraft.

1.2 CURRENT STATE OF THE ART

As state of the art of GBAS the service types C and D are considered [3], [4]. The service types were designed to support CAT-I approaches (GAST C) and CAT-III operations including automatic landings without visibility requirements (GAST D) [5], [6]. The differential GNSS corrections provided to arriving aircraft by the ground station enable significantly improved guidance [7], [8]. The calculated deviations include much less signal distortions than ILS, provide greater accuracy and, contrary to conventional navigation aids, also onboard integrity in the form of error bounds associated with the current position estimate. When considering automatic landings, the performance of the navigation system is a key parameter, however, also the performance of the autopilot is crucial. The high-level safety requirements are defined on aircraft level and thus include both subsystems and their interaction [9], [10]. Thus, the total error budget has to be allocated between navigation system and autopilot. On the autopilot side the performance is described by a nominal touchdown point and the standard deviation of a Gaussian distribution accounting for the uncertainty caused e.g. by wind, aircraft weight and balance and other influences [11], [12]. The nominal touchdown point and autopilot performance of course differ between aircraft types and the current wind and loading conditions for each specific approach. In the process of deriving navigation requirements, a “standard” autopilot performance is used

that should ideally cover all aircraft using GBAS [13]. It is obvious that in the derivation process the autopilot performance has to be conservatively assumed. Thus, the navigation requirements are more stringent than necessary for most aircraft and approach conditions but, on the other hand, may not necessarily cover all situations.

In GAST C the ground station is responsible to bound the error at the output of the airborne receiver. In addition to conservative assumptions about the autopilot performance, conservative navigation system error bounding has to be performed, in order to meet the stringent integrity requirements. For GAST D the philosophy was changed in a way that the monitoring for ionospheric disturbances is shared between the ground and the airborne systems. Thus, the conservatism could be somewhat reduced but more sensitive monitoring algorithms were included in GBAS in order to protect users from potentially large positioning errors due to ionospheric gradients. The sensitive monitoring for ionospheric gradients within the ground station is challenging due to strong limitations on the spacing between reference antennas and thus the footprint of the GBAS installation on an airport where usually the space is very limited. Furthermore, it requires an extremely stable phase center of the reference antennas and can also be impacted by tropospheric disturbances. While GAST D is now also standardized, it is expected that the availability of the system will not be high enough to meet operational requirements in all regions of the world. Ionospheric issues lead to a degraded performance where ionospheric activity is high and significant (mainly in equatorial and polar regions). Thus, the current version of GAST D may still see some changes and improvements in the future.

In order to overcome many of the challenges of current single frequency and single constellation GBAS, the system is being further developed to include also signals from other GNSS constellations and a second frequency. The latest generation of GPS satellites (the Block II F satellites), as well as all functional Galileo satellites, already offer additional signals in the L5 frequency band that can be used for aviation purposes. Dual frequency methods allow for detection of ionospheric gradients or forming of an ionosphere free combination of the navigation signals. Using more than one constellation makes the system less vulnerable against loss of signals due to ionospheric scintillations and associated loss of lock of the satellite signals that occur very frequently in equatorial regions. However, the development of these methods has only started recently and to date no processing method with a corresponding integrity concept has been developed. Despite the obvious benefits new challenges, technical (e.g. increased measurement noise in the ionosphere free combination), regulatory (e.g. development of new antenna and receiver standards) and political (approval of the use of different GNSS constellations are national responsibility and thus may be different in each country) issues still have to be resolved before the next generation of multi constellation and dual frequency GBAS can become operational.

1.3 OBJECTIVES OF THIS WORK

This work should be seen in the context of supporting the development and promoting the implementation of GBAS as primary guidance system for precision approaches and landings.

The general objective is to advance the system on a technical level but always with the constraint to keep it certifiable with minimal additional effort and to maintain compatibility with existing hardware with as little modifications as possible. This shall be achieved by a tighter integration of the navigation and autoland system, taking into account available knowledge about sensors and systems in real-time instead of relying on conservative assumptions. For this purpose, a critical review of the underlying assumptions made during the requirement definition process is carried out. This process shall identify potential improvements in the allocation of the allowable error budget considering the available knowledge about the navigation system and the autopilot, where applicable. The identified improvements are then applied to existing GBAS architectures to evaluate potential benefits in existing systems with only slight modifications.

Finally, the general concept is also discussed in the light of the development of future GBAS generations that are developed to include dual frequency and multi constellation techniques. As there is currently no concept fully developed how future GBAS architectures should work and be implemented, there is great potential to define new ways of error budget allocation. These can take into account the interaction between the GBAS navigation sensor and the autopilot in order to achieve a landing system that is robust against disturbances and capable of providing availability of service at a level that is currently provided by the ILS.

This work is not considering any operational approval aspects of new procedures or potential changes and optimizations that could be done in the autopilot in order to exploit the much-improved guidance performance. These topics are left for future work to experts in the respective areas.

1.4 OUTLINE AND OVERVIEW OF THE CONTRIBUTIONS

In order to achieve the aforementioned objectives, the thesis is organized into four main chapters after this introduction, followed by a summary with conclusions and an outlook on potential future work in the area.

The following Chapter 2 gives an overview of approach classifications and current approach guidance systems and their functionalities. After a short discussion of the ILS it provides a description of the GBAS service, the ground and airborne subsystems and the integrity assurance. In order to compare the nominal performance of the two systems flight test data were collected and evaluated. The evalua-

tion of the in-flight performance of ILS and GBAS is presented showing clearly the significantly improved nominal guidance performance of the GNSS-based system.

The contribution contained in this section is the first in-flight comparison of actual ILS and GBAS performance during approaches carried out with an Airbus A320 as example for a representative commercial aircraft presented in [7].

Chapter 3 details the process of deriving requirements for the navigation system and highlights the trade-off between navigation system error (NSE) and flight technical error (FTE), i.e. the autopilot performance. Based on airworthiness requirements, and more specifically, the definition of a safe landing, the total system performance requirements are presented. Next, the resulting requirements for the autopilot performance, and finally the derived requirements for the navigation system are discussed.

The contribution in this section is a critical review of the requirement derivation process for GBAS-based automatic landings and the identification of possible relaxations of the monitoring requirements from the state of the art methodology. Potential relaxations are suggested by taking into account actual conditions and known parameters instead of worst-case parameters. These suggestions are then used in Chapter 5 as basis of a new GBAS ground monitor that is developed and described there.

Chapter 4 focuses on the autopilot performance. After a short general description of the autopilot functionalities an exemplary study of the influence of different effects on the touchdown performance is presented. The model of the Airbus A320 autoland system was used to simulate landings under different wind conditions, as well as the impact of aircraft weight and balance on the nominal touchdown point and the dispersion of touchdown points.

The contribution of this chapter is the analysis of the touchdown performance and the suggestion to apply the Gaussian overbounding method or the use of a Johnson distribution to model the results. This is deemed necessary in order to not underestimate the risk of landing outside the touchdown box described in Chapter 3, due to the non-Gaussian and non-symmetric distribution of the touchdown points. It is further suggested and illustrated at the example of aircraft landing weight and center of gravity location to use available knowledge when assessing the touchdown performance in order to obtain a less varying distribution for the touchdown points and be able to use this margin. Finally, the trade-off between NSE and FTE performance is performed and discussed based on the results.

Chapter 5 is dedicated to the NSE of GBAS and is the largest part of this thesis. It starts with a discussion of nominal and non-nominal errors and then analyzes in more detail the impact of the ionosphere and its disturbances on GBAS. Ionospheric issues have the potential to cause large positioning errors and are a major concern for the differential architecture of GBAS. Most of the monitoring and error bounding in the current GBAS service types C and D is dedicated to the mitigation of this potential threat.

The chapter then presents two further contributions of this thesis: The first one is the development of a monitoring architecture for a GAST D ground station to safely detect and mitigate the threat posed to GBAS by ionospheric gradients. It is based on an additional reference receiver that is placed as far as possible from the original GBAS but for safety reasons still within the airport. The concept shows the potential of applying the relaxations identified in chapter 2 and was presented in [14].

The second contribution in this chapter is the development of a monitor for dual frequency GBAS that operate in single frequency positioning mode (a highly likely candidate for future GBAS architectures). It uses dual frequency measurements to detect difference in the ionospheric delay between the ground station and the aircraft on one or more satellites. In contrast to all current service types, it is suggested to perform this monitoring on board the aircraft so that the knowledge about current navigation system performance and autopilot performance can be fully leveraged. In that way, the conservatism in the error bounding process can be reduced to a minimum and system availability greatly increased. The monitor was presented in [15].

Chapter 6 contains the conclusions of this thesis. They summarize again the contributions of each chapter and discuss their significance in the GBAS context. Finally, suggestions for further research in this area are given.

2 APPROACH CLASSIFICATIONS AND GUIDANCE SYSTEMS

This chapter gives a summary of approach classifications depending on different weather conditions and services offered, as well as an overview of current state-of-the-art approach guidance systems. The Instrument Landing System (ILS) is the current standard technology for precision approach guidance. First Ground Based Augmentation Systems (GBAS) have been deployed and now also offer approach guidance under conditions up to CAT-I. Systems capable of providing CAT-II/III guidance are standardized and will become operational in the near future. ILS is relying on two ground transmitters defining a straight approach track for each runway end while GBAS generates corrections to GNSS signals which are broadcast via a VHF data link. It is thus possible to define not only straight approach tracks, as currently with ILS, but also curved and segmented steep approaches. After a short description of the ILS a review of the GBAS subsystems is presented together with their functions, GBAS based positioning as well as the integrity concept. Next, the way of calculating guidance information (i.e. deviations from the desired track) for the approach is shown. The chapter then concludes with a comparison of the nominal performance of GBAS and ILS as observed in flight trials. It can be observed that GBAS performance is significantly better than that of the ILS in terms of noise and absolute errors in the guidance signal.

<u>Contribution:</u> *In-flight comparison of ILS and GBAS approach performance (Results in Chapter 2.3)*

<u>*Publications:*</u>

- M. Felux, T. Dautermann and H. Becker, "GBAS landing system - percision approach guidance after ILS," *Aircraft Engineering and Aerospace Technology,* vol. 85, no. 5, pp. 382-388, 2013. [7]
- M. Felux, T. Dautermann and H. Becker, "GBAS Approach Guidance Performance - A Comparison to ILS," in *Proc. ION ITM*, Newport Beach, CA, USA, 2013. [16]

Under low-visibility conditions an approach guidance system together with an appropriate approach procedure is necessary for aircraft to safely approach and land at an airport. The procedure provides a flight path with sufficient obstacle clearance on the approach and on the missed approach track as specified in the ICAO Doc8186 [17]. Depending on ground and airborne equipment, runway category, crew and operator certification, different levels of service can be provided. These reach from visual via non-precision approaches to approaches with vertical guidance and finally precision approaches. Table 2-1 summarizes the classifications for the different approach operations, approach runways and system performance procedures. It summarizes the changes that were agreed upon in 2012 by the International Civil Aviation Organization (ICAO) to the ICAO Annex 6 “Operation of Aircraft” [18], Annex 10 “Aeronautical Telecommunications” [4] and Annex 14 “Aerodromes” [19]. Approach operations are classified as Type A and Type B for Decision Heights above 250 ft or below that value, respectively. Type A approaches can be based on 2D guidance (i.e. lateral guidance only) or 3D guidance (additional vertical guidance available), while Type B operations require 3D guidance. Type B operations are then subdivided into three categories (CAT) I / II / III, depending on the minimum decision height or altitude (MDH/A) and minimum visibility conditions. Runways are classified according to which type of operation they support and system performance is classified into non-precision approach, approach with vertical guidance and precision approach. Systems foreseen to support Type B operations are ILS, MLS, SBAS and GBAS.

While at the moment ILS is by far the most used guidance system for final approaches, GNSS based navigation is being implemented and an ever increasing number of SBAS and GBAS approaches are being defined and published. For SBAS the US Wide Area Augmentation System (WAAS) supports CAT-I precision approaches, while the European Geostationary Overlay Service (EGNOS) supports APV operations with a DH/A of 250 ft. For approaches in visibility conditions lower that the ones mentioned and for autoland operations, local augmentation in the form of a GBAS is necessary to meet the time to alarm requirements and protect the user from rare ionospheric disturbances which have the potential to cause GNSS positioning errors large enough to prevent safe operations of aircraft during landing. In the following chapters ILS and GBAS are explained in more detail and a comparison of both systems is presented.

This work mainly focuses on Type B operations, and especially on CAT-II/III autoland operations based on GBAS as approach guidance system. In GBAS terminology different GBAS approach service types (GAST) are defined, which again correspond to different levels of service. The service type supporting Type A and B operations to the CAT I minima according to Table 2-1 is GAST C, while the service type supporting Type A and B operations including CAT II/III is termed GAST D. The latter one is the GBAS approach service type focused on within this work.

<table>
<tr><td>Domain</td><td>Document</td><td colspan="5">Aspect</td></tr>
<tr><td rowspan="3">Approach Operations</td><td rowspan="3">Annex 6</td><td rowspan="2">Classification</td><td colspan="2">Type A</td><td colspan="3">Type B</td></tr>
<tr><td colspan="2">>250ft</td><td>CAT-I (>200ft)</td><td>CAT-II (>100ft)</td><td>CAT-III (<100ft)</td></tr>
<tr><td>Method</td><td>2D</td><td colspan="4">3D</td></tr>
<tr><td>Minima</td><td>MDA/H</td><td colspan="4">DH/A</td></tr>
<tr><td rowspan="4">Approach Runways</td><td rowspan="4">Annex 14</td><td>MDA/H
VMC</td><td colspan="2">Non-instrument runway</td><td colspan="3"></td></tr>
<tr><td>MDA/H >250ft
Visibility > 1000m</td><td colspan="2">Non-precision approach runway</td><td colspan="3"></td></tr>
<tr><td>DA/H >200ft
Visibility > 800m or RVR > 550 m</td><td colspan="3">Precision approach Runway, Category I</td><td colspan="2"></td></tr>
<tr><td>DA/H > 100ft
RVR ≥ 300m</td><td colspan="4">Precision approach Runway, Category II</td><td></td></tr>
<tr><td rowspan="3">System Performance Procedures</td><td rowspan="3">Annex 10</td><td>DA/H ≥ 0ft
RVR ≥ 0m</td><td colspan="5">Precision approach Runway, Category III</td></tr>
<tr><td>NPA</td><td colspan="2">NDB, Lctr., VOR, LOC, GNSS</td><td colspan="3"></td></tr>
<tr><td>APV</td><td rowspan="2"></td><td>GNSS, Baro, SBAS</td><td colspan="3"></td></tr>
<tr><td>PA</td><td colspan="4">ILS, MLS, SBAS, GBAS</td></tr>
</table>

Table 2-1 Summary of approach classification according to [20].

2.1 THE INSTRUMENT LANDING SYSTEM

The Instrument Landing System (ILS) is currently the only widely used precision approach guidance system. It has been in use since the 1940s and can provide precision approach guidance for manual or automatic approaches and landings. Two separate antenna arrays form the core of an ILS ground station: the localizer is placed behind the end of the runway to which approach service is provided. It is used for horizontal guidance during the approach and rollout on the runway; the glide slope transmitter is placed typically about 60 m next to the runway abeam the touchdown point for vertical guidance. Both systems form two narrow beams with different modulations slightly to the left and right and above and below the desired approach track (90Hz for the left and upper one, 150Hz for the right and lower one) onto a carrier signal (110MHz for the localizer and 330MHz for the glide slope). When the

aircraft is aligned with the extended runway centerline and the glide path, both signals are received equally strong and the difference in depth of modulation (DDM) of the two respective signals is zero. Whenever the aircraft deviates from the approach track the DDM becomes non-zero indicating a deviation to the pilot (and outputting it to the autopilot if connected).

By design and technical realization of the system there is no way of providing other than straight-in approach tracks. Furthermore, it is quite common that preceding aircraft create signal distortions to other trailing aircraft due to multipath and signal shadowing effects of the signals from the ground. Further out on the approach this does not cause problems. However, when operating near the ground such distortions could potentially endanger the safety of aircraft. In an incident in 2011 a B777 made a runway excursion upon performing an automatic landing at Munich Airport. It was most likely caused by such signal distortions from a departing aircraft from the same runway when the landing aircraft was shortly before touchdown [21]. In visibility conditions below the CAT-I minima spacing between aircraft is thus increased to ensure undistorted signal quality for operations near the ground. These operational measures, however, reduce airport capacity and lead to a significant amount of delay and flight cancellations at large airports which operate near their capacity limits.

In its long history in service several incidents and also fatal accidents were attributed to ILS or more precisely the characteristics of the beams emitted from the localizer and glide slope antennas. In addition to the desired narrow guidance beams defining the actual desired approach track there are side lobes which can be captured by the autopilot and have led to several incidents or accidents [22], [23], [24].

Despite these issues which are mitigated (if no other human or technical factors prevail) by operational and procedural measures the system has proven to be extremely reliable and is operated by almost all major and a very large number of regional airports to support precision approach guidance. It is only in the next decades when satellite navigation with its different kinds of augmentation systems will be able to fulfill the task to provide precision guidance under all weather conditions with the same availability that the existence and further use of ILS might be put in question. For precision approaches to CAT-I (or with slightly higher minima) there are ground and space based augmentation systems (GBAS, SBAS) with suitable procedures at an ever increasing number of airfields available. Especially for regional airports, CAT-I capability is often sufficient to meet their needs. An SBAS procedure does not require any additional ground infrastructure and is thus an economically very attractive solution for such airports. However, at large airports a solution for CAT-II/III weather conditions is often necessary. The development of standards for a CAT-II/III capable GBAS has been finished and first stations will become operational in the near future. However, due to challenges with ionospheric disturbances it is expected that initially the availability will not reach the same level that is provided by the ILS.

2.2 THE GROUND BASED AUGMENTATION SYSTEM

The Ground Based Augmentation System (GBAS) is a landing system designed for aircraft, which augments satellite navigation signals by broadcasting differential corrections, integrity parameters and approach reference coordinates to provide precision approach and rollout guidance.

Due to the weakness of signals from the navigation satellites that are correlated from below the noise floor and the resulting vulnerability to distortions in the atmosphere (especially in the ionosphere), interference, multipath and several other error sources the accuracy and especially integrity of standalone GNSS is not sufficient for safety of life applications, such as precision approach guidance. The approach to augmenting GNSS signals is based on a differential architecture in order to achieve performance suitable for aviation. A schematic overview of GBAS is given in Figure 1. Typically four reference receivers are placed at precisely surveyed locations and protected sites at an airport. This allows monitoring of the navigation signals from the satellites and calculation of locally relevant corrections which cancel all errors common to the ground station and airborne user. In the onboard receiver of arriving aircraft the corrections from the ground system are applied to the measured pseudoranges of the GNSS receiver and a position solution is calculated based on the corrected measurements. In order to ensure integrity, so-called protection levels which are conservative bounds on the position error are calculated. They are compared to so-called alert limits which are threshold values for the protection levels. As long as the navigation error bound stays below the alert limit the operation is considered to be safe. If the protection level exceeds the alert limit the GBAS service is set to unavailable since the safety cannot be guaranteed anymore. In addition to comparing protection levels to alert limits further low-level monitoring for specific failure modes may be necessary depending on the active service type and is included in the respective service type standards. Finally, the ground station also transmits coordinates describing the desired approach track. Based on the augmented position solution deviations from the desired approach track are calculated and displayed to the pilot as ILS lookalike deviations and are used as input for the autopilot. Currently, only the definition of ILS-lookalike “straight-in” approaches is used but there are provisions to also include further specifications of so-called terminal area paths (TAPs) that allow the definition of straight and curved segments to define advanced approach procedures. A current GBAS can support up to 49 different approach tracks. In the following sections the process of estimating a position, the different GBAS subsystems and their tasks as well as assurance of integrity are described more in detail.

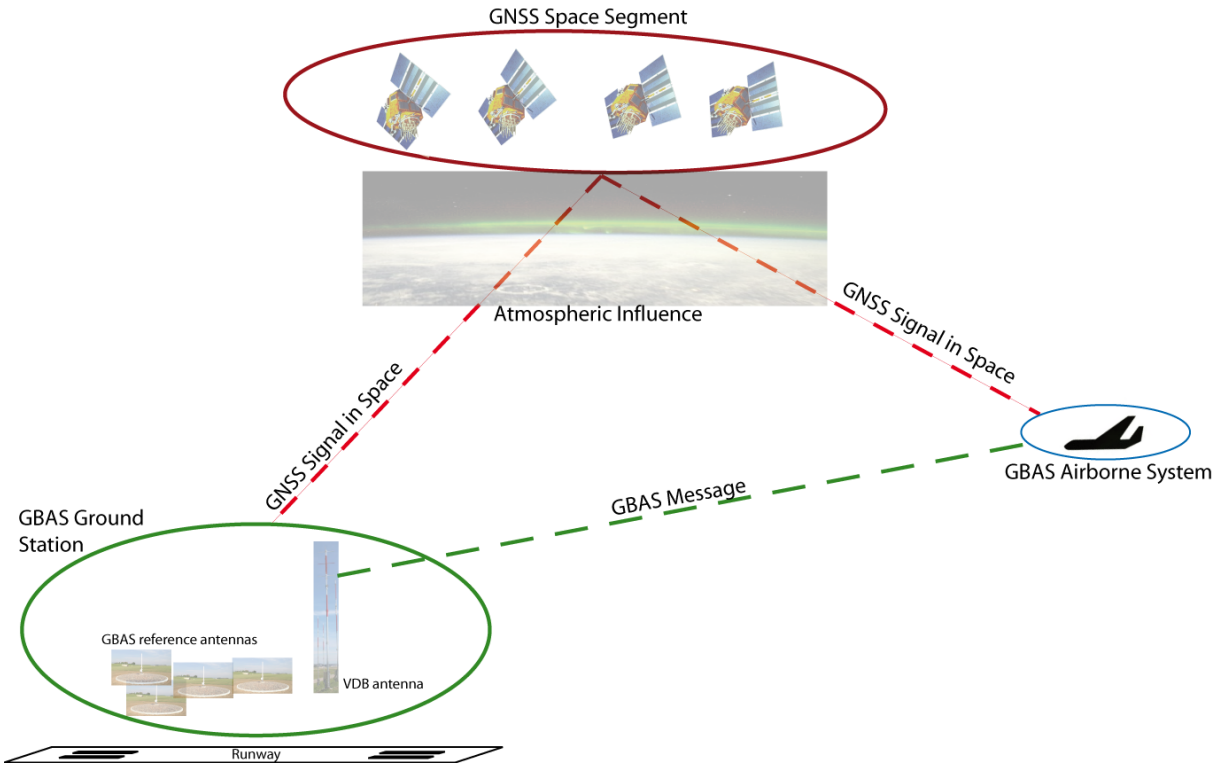

Figure 1 Schematic overview of GBAS elements

2.2.1 GNSS position estimation and potential influences

The GNSS position estimate is based the principle of multilateration. GNSS satellites broadcast their orbit parameters which enables a user to calculate the satellite positions at any given time. By measuring the distance between the satellites and the receiver a user position can be estimated. The range to a satellite, however, cannot be measured easily and directly. What can be measured is the signal travel time from the satellite to the receiver. Multiplied with the speed of light this travel time gives an estimate of the distance. Since the clock in the GNSS receiver and the GNSS constellation is not synchronized, this does not corresponds to the true range but contains a large error mainly due to the clock offset of the receiver clock but also due to other influences. The pseudorange ρ_n between satellite n and the user is modelled as

$$\rho_n = \left|\vec{x}_{usr} - \vec{x}_{SV}\right| + c \cdot \Delta t_{rx} + c \cdot \Delta t_{SV} + T_n + I_n + b_{TGD} + \eta_n \tag{1}$$

where $\vec{x}$ are the three dimensional position vectors of the user and the satellite, respectively, in an earth-centered, earth-fixed (ECEF) coordinate frame. c is the speed of light in vacuum, Δt_{rx} is the clock offset of the user receiver, Δt_{SV} the satellite clock offset to system time, T_n and I_n the delay induced by the troposphere and ionosphere on the path between user and satellite n, b_{TGD} the time group delay and η_n the measurement noise and multipath influence. Since only the geometric distance between user and satellite is desired, the other influencing terms have to be addressed in a way which is

appropriate for the application. The receiver clock offset is the same for each pseudorange measurement. It can thus be estimated as a fourth unknown (in addition to the 3 dimensional position). The satellite clock offset is well modelled and can be removed by applying a correction based on parameters transmitted in the navigation message of each satellite to a level that is sufficient for GBAS positioning. The tropospheric delay either has to be modelled or corrected differentially. The ionospheric delay can be modelled or differentially corrected as well. However, due to significant variations modelling is usually not sufficient for the GBAS application. The ionospheric delay is furthermore a frequency dependent term that can be estimated if pseudorange measurements on two different frequencies to the same satellite are available. Dual frequency GBAS are currently in the early stages of development. The time group delay is a satellite specific parameter which is pre-calibrated in the qualification process before the launch of each satellite and also transmitted as part of the navigation message. The measurement noise and multipath are addressed by placing the antenna in a low-multipath environment, using high quality receivers and components and using code-carrier smoothing that will be described later in Section 2.2.2.2. The residual noise and multipath components are modelled statistically but they cannot be removed completely from the measurements or be corrected differentially.

2.2.2 GBAS Ground System

The GBAS Ground System consists of typically four reference receiver at an airport to which approach service is provided. The required performance of a station is determined by the GBAS Approach Service Types (GAST) the station provides. The GAST is a matched set of requirements for the ground and airborne systems enabling different approach minima. Approaches under CAT-I (or better) conditions using only single frequency L1 C/A code measurements from the GPS constellation are supported by GAST C while CAT-II/III operations using the same signals are supported by GAST D. Future service types will likely also the possibility to use signals from another frequency and other GNSS constellations, such as the European Galileo, the Russian Glonass or the Chinesse Beidou and provide increased robustness and availability. This section describes briefly the necessary siting measures for these references as well as the process of generating the correction a GBAS transmits to arriving aircraft. Furthermore, the derivation of the transmitted integrity parameters for different service types is discussed. The differences between the service types are pointed out in the description where applicable.

2.2.2.1 Reference Stations

To protect the measurements at the references from potential error sources appropriate siting of the antennas is crucial. The FAA issued a GBAS siting order (FAA Order 6884.1) [25] for ensuring sufficient protection of the GNSS signals against external influences. The content of this section is summarizing the most important of these requirements. One of the main potential influences to the quality of the provided corrections is multipath from ground reflections [26]. Ground multipath can cause low

frequency effects on the pseudorange measurements which can hardly be mitigated through carrier smoothing. For GBAS, specially developed Multipath Limiting Antennas (MLA) are thus used which have an antenna pattern with an extremely sharp cutoff at an elevation of 5° which is the minimum elevation for which a satellite may be used in GBAS. The antenna is furthermore surrounded with graded gravel to scatter potential reflections. Figure 2 shows a GBAS reference antenna of an operational GBAS with the appropriate siting measures at Zürich Airport. In addition to ground reflections, multipath may also be caused by other structures such as buildings or equipment shelters or by vehicles on service roads passing by the antennas. Reflections from steady reflectors are addressed by selective masking out certain azimuth/elevation combinations, while the effect of transient objects is handled by operationally restricting access to the so-called Local Objects Consideration Area (LOCA). On the signal processing side a monitor for statistically relevant changes in the code minus carrier measurements as estimator for multipath is monitored in form of a cumulative sum monitor [27].

Figure 2 GBAS reference antenna at Zürich Airport (LSZH) [28]

To ensure that despite all previous measures no correlated multipath effects affect more than one reference location the minimum separation of the reference antennas is set to 100m (Section 5.2 b.(5) of [25]). By crosschecking the potential corrections from the different reference receivers, individually affected references can be determined and excluded or de-weighted appropriately.

The problem of radio frequency interference (RFI) has become an unexpected challenge in an operational environment as well. At Newark Airport in New Jersey, which was planned to be the first station to enter service, the four reference receivers were placed close to the I-95, a highway with 15 lanes and thus lots of traffic. Soon after beginning data evaluation it was found that GPS jammers (so-called

personal privacy devices, PPD) are used in vehicles passing by the airport which regularly affected the ground stations and interrupted GBAS service [29], [30]. Several operational measures like lowering the installation height of the reference antennas, introducing an additional mesh in the airport perimeter fence, building a protection wall between the highway and the airport as well as a software change in the ground facility were necessary to mitigate this problem. The location of the reference antenna for a second GBAS in the US at Houston Airport was thus selected far away from any public roads in between two parallel runways [31].

Finally, the geometry and separation of the GBAS reference antennas has an impact on the monitoring performance for satellite orbit errors and especially on the monitoring for ionospheric gradients as will be further described in Section 5.4 . The monitoring algorithm for ionospheric gradients in the ground system requires very specific spacings between the reference antennas so that the footprint of the GBAS at an airport is quite determined [32], [33].

Together with other restrictions concerning obstacle clearance areas around runways and taxiways according to [19], siting of a GBAS ground station is a difficult task which is crucial for later performance and consequently the availability of the service at a given airport.

2.2.2.2 GBAS Corrections

One of the main tasks of GBAS ground station is generating corrections for the navigation signals. Future systems will have to be extended to generate corrections and integrity parameters for each frequency and constellation. The way of generating the corrections is assumed to remain unchanged. Note that here the frequency dependency is thus not explicitly stated for better readability. Generating corrections is feasible because the reference antennas are located at precisely known and surveyed positions. In a first step the raw pseudorange measurements ρ_n from satellite n are smoothed with corresponding carrier phase measurements ϕ_n using a Hatch filter [34]. The code measurement permits determination of the pseudorange (actual range plus ranging error due to receiver clock offset and propagation disturbances) but it contains (mainly elevation dependent) noise and multipath errors in the order of meters. The carrier phase onto which the navigation code is modulated can be tracked very precisely with noise and multipath only in the order of millimeters. The phase measurement, however, is ambiguous, i.e. ranging is not possible (at least not for the techniques used in the GBAS context). Combining both measurements in a smoothing filter can eliminate a great part of the noise on the measurement. The smoothed pseudorange $\hat{\rho}_n$ at epoch n is described as (according to section 3.7.1.2.8.3.3 of [35] and section 3.2.1.2.8.5.1 of [36]]

$$\hat{\rho}_n = \alpha\rho_n + (1-\alpha)\left(\hat{\rho}_{n-1} + \frac{\lambda}{2\pi}(\phi_n - \phi_{n-1})\right) \tag{2}$$

where λ is the wavelength of the carrier phase (0.1905 m for GPS L1 and Galileo E1, 0.255 m for GPS L5 and Galileo E5a) and $\alpha = 0.5s \div \tau$ is the filter weighting constant depending on the filter time

constant τ . The time constant is depending on the active service type of the station. For GAST C it is 100 s while in GAST D two sets of corrections are provided in parallel, one based on 100 s and the other on 30 s smoothing. This is part of the mitigation strategy for ionospheric anomalies and enables the airborne user to detect disturbances by comparing position solutions based on two different filters. This method is described in more detail in Section 2.2.3. Future service types are still under development, however, due to backwards compatibility issues and the need to reuse existing signals also in new service types the smoothing time constants used will probably be restricted to the same time constants [37].

In a next step a preliminary pseudorange correction $PRC_{prel,\tau}(i, j)$ is calculated for each smoothing time constant τ and each satellite i in view and above the minimum elevation angle (5°) at each receiver j . This is done according to Section 3.7.1.2.8.3.1 of [35] or Section 3.2.1.2.8.5.4 of [36] and described as

$$PRC_{prel,\tau}(i, j) = r_{i,j} - \hat{\rho}_{i,j} - c\Delta t_{sv,i} \tag{3}$$

with $r_{i,j}$ the known geometrical range between the antenna position of reference receiver j and the position of satellite i , $\hat{\rho}_{i,j}$ the corresponding smoothed measured pseudorange and $c \cdot \Delta t_{SV,i}$ the relativistic satellite clock correction term. Note that those preliminary corrections still contain the receiver clock error from each reference receiver. To remove this contribution the average of all corrections from each receiver is removed per constellation and per frequency. This process is called “smoothed clock adjust” and the resulting corrections $PRC_{sca,\tau}(i, j)$ are described as

$$PRC_{sca,\tau}(i, j) = PRC_{prel,\tau}(i, j) - \sum_{i=1}^{N} k_i \cdot PRC_{prel,\tau}(i, j) \tag{4}$$

where N is the number of satellites and k_i are weighting factors. While in ED-114A [35] (according to Section 3.7.1.2.8.3.5) a meaningful elevation dependent weighting is permitted, requiring only that $\sum k_i = 1$, [36] (in Section 3.2.1.2.8.5.6) specifies them to be all equal. The process is illustrated in Figure 3. A different weighting of the individual measurements will result in a different location of the weighted average, and thus also in different PRCs. As a common offset in pseudorange measurements or in PRCs that are applied to pseudorange measurements does not affect the position solution but only the receiver clock estimate, there is no effect on the user side when the ground station applies different weighting methods (see Appendix II).

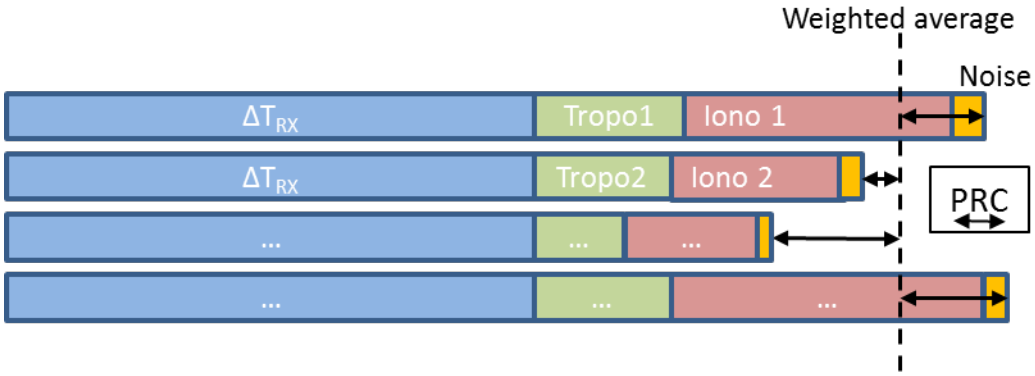

Figure 3 Generation of pseudorange corrections

Finally, a single correction $PRC_{tx,\tau}(i)$ for each satellite and each smoothing time constant to be broadcast is obtained by averaging the smoothed clock adjusted corrections from all receivers j for each satellite i

$$PRC_{tx,\tau}(i) = \frac{1}{M(i)} \sum_{j} PRC_{sca,\tau}(i, j) \tag{5}$$

with $M(i)$ the number of receivers tracking satellite i.

Together with the pseudorange corrections, the ground station also provides range rate corrections (*RRC*) which are obtained by dividing the difference between current and previous *PRC* by the update rate (0.5 s). This is done to enable the airborne system to extrapolate from the last received message to the next because the airborne update rate is specified to be at least 5 Hz [38] and thus faster than the update rate of the GBAS message from the ground.

PRC and *RRC* for each satellite obtained with a 100s smoothing time constant, together with a timestamp and checksum parameters are contained and transmitted in the Type 1 GBAS message [39]. The *PRCs* and *RRCs* based on 30s smoothing used in GAST D are transmitted in the Type 11 message which was added after the original message definition where only one smoothing time constant was foreseen. All future corrections for additional frequencies and constellations have to be accommodated in new message types still to be defined.

2.2.2.3 Integrity Parameters

In order to enable arriving aircraft to bound their residual position errors for the GBAS corrected measurements, the ground station transmits several integrity parameters relating to different error sources. The following subsections describe these parameters, their role and their application.

2.2.2.3.1 P-values

The P-values are the ephemeris decorrelation parameters transmitted in the Type 1 message. They are applied to bound the effect of a potential ephemeris error that has a different effect on a user at a certain distance from the ground station. They “shall characterize the impact of residual ephemeris errors

due to spatial decorrelation" [36] for all corrections broadcast in the Type 1 message. The P-value is defined as the minimum detectable error (MDE) of the ephemeris monitor implemented in the GBAS ground station divided by the range between the GBAS reference point and the satellite. The MDE depends on the type of ephemeris monitor implemented and for many implementations also on the baseline length and orientation between the receivers. Another algorithm is based on checking the difference between the last validated ephemeris (up to 24h old) and the current ephemeris of a satellite and monitor the change [40]. For current implementations of GBAS this monitoring is considered sufficient, however the P-values obtained in this way may be too large to expand the current service volume for future operations like continuous descent operations where also sufficient reliability has to be ensured at larger distances from the airport.

2.2.2.3.2 B-values

The B-values are an "estimate of the error contribution from" [36] each reference receiver to the corrections provided to the aircraft. They are computed for each satellite i and reference receiver j as

$$B(i,j) = PRC_{tx,100}(i) - \frac{1}{M(i)-1}\sum_{\substack{k\in S_i \\ k\neq j}} PRC_{sca,100}(i,k) \tag{6}$$

where $M(i)$ denotes the number of reference receivers which were used to generate the correction for satellite i and S_i is the set of reference receivers tracking satellite i. Before a correction for a specific satellite is calculated the corresponding B-values are compared to a monitoring threshold to identify potentially faulty measurements from one reference receiver and exclude the corresponding data from the calculation of corrections.

2.2.2.3.3 Sigma PR Ground

$\sigma_{pr,gnd}$ is the standard deviation of a zero-mean normal distribution associated with the residual uncertainty in the GBAS corrections. It "shall account for all equipment and environmental effects, including the received signal power, the local interference environment, and any transient error in smoothing filter output, relative to steady-state, caused by ionospheric divergence" [36]. The estimate of $\sigma_{pr,gnd}$ for a ground station can be obtained by either observing code minus carrier measurements or by a B-value assessment. The later method is usually the preferred one since in the code minus carrier observations the ionospheric error has to be estimated to separate it from the noise and multipath effect. For the ionospheric estimate dual frequency measurements are necessary which are typically not available in GAST C and GAST D ground stations. The estimate takes into account at least one day of recorded measurement data from B-values associated with validated corrections. For each reference receiver only one sample every 200 seconds is used to ensure that the data is uncorrelated. The remaining B-values are then sorted according to the elevation of the corresponding satellite into bins. For each such bin the mean and standard deviation σ_B are calculated. The mean is expected to be close to zero and the root mean square (RMS) for each reference receiver j is then calculated as

$$RMS_{pr\_gnd,j} = \sigma_{B,j}\sqrt{(M-1)\frac{N+1}{N}} \tag{7}$$

where M is the number of reference receivers and N is the average number of satellites which were tracked at the epoch the B-value was evaluated. This process yields one curve for each reference receiver. The broadcast $\sigma_{pr,gnd}$ for each elevation bin is taken as the maximum value of the individual estimates and is transmitted in the Type 1 message. Due to different signals on the different frequencies and constellations it will be necessary do define this parameter for each signal and possibly also for each constellation individually.

2.2.2.3.4 Tropospheric parameters

For enabling the aircraft to calculate a differential tropospheric correction and bound the residual tropospheric error there are three parameters provided by the ground station as part of the Type 2 message. The first one is the refractivity index N_R of the atmosphere at the GBAS location. It consists of a dry and a wet component and can be calculated based on locally measured weather data (temperature, air pressure and humidity) [41]. As the variations of N_R are small it can be assessed and used as a yearly average [42]. To account for the uncertainty introduced by considering such a long time span a refractivity uncertainty σ_n is calculated by assessing a daily value and compare it to the yearly average. This uncertainty is then expressed as a standard deviation of a normal distribution and provided to the aircraft for inclusion in the error bounding process in the on-board system [41]. A third parameter which is provided by the ground station is the tropospheric scale height h_0. It is also calculated based on the earth surface height at the GBAS location and based on the dry and wet components of the refractivity index N_R [41].

2.2.2.3.5 Sigma Vertical Iono Gradient

The parameter providing information about the residual uncertainty associated with nominal ionospheric impact in vertical direction is described by the value σ_{vig} which is transmitted in the Type 2 message. It is a parameter which is contained in the ionospheric threat model of the region where the GBAS is located. Every national regulator has to ensure that a valid and representative threat model for the ionospheric impact is developed. This is usually done by evaluating data collected over one solar cycle from a network of reference receivers in a representative region. Ionospheric threat models have been determined e.g. for the contiguous United States (CONUS) [43], Germany [44], South Korea [45]. Based on the elevation of a satellite the vertical uncertainty is then mapped into a slant uncertainty corresponding to an overbound of the expected error on the pseudorange measurement.

2.2.2.4 Approach reference coordinates

In addition to corrections and integrity parameters, the GBAS ground station also provides necessary reference coordinates to enable the aircraft to compute ILS like deviations from a reference trajectory by defining the final approach segment (FAS). Provisions also foresee the transmission of Terminal

Area Paths (TAP) defining approach tracks based on straight and curved radius to fix segments for future advanced approach procedures. The provision of all these reference coordinates via the GBAS message has the advantage that no database of reference coordinates has to be present and be continuously updated on board the aircraft.

The FAS data block is part of the Type 4 GBAS message and the calculation of deviations based on the provided reference points is described in Appendix C of [38]. The main reference point on the ground is the Landing Threshold Point (LTP). It is located in the middle of the runway threshold and is the origin of a local-level tangent coordinate system defined by unit vectors pointing in runway direction $\vec{u}_{rw}$, in vertical direction $\vec{u}_{vert}$, and a vector $\vec{u}_{lat}$ which is perpendicular to the previous two. The calculation of lateral deviations is based on the definition of a vertical plane containing the GBAS Landing System (GLS) Azimuth Reference Point (GARP), the LTP and the Threshold Crossing Point TCP, which is located vertically above the LTP. The approach geometry for the lateral deviations is illustrated in Figure 4.

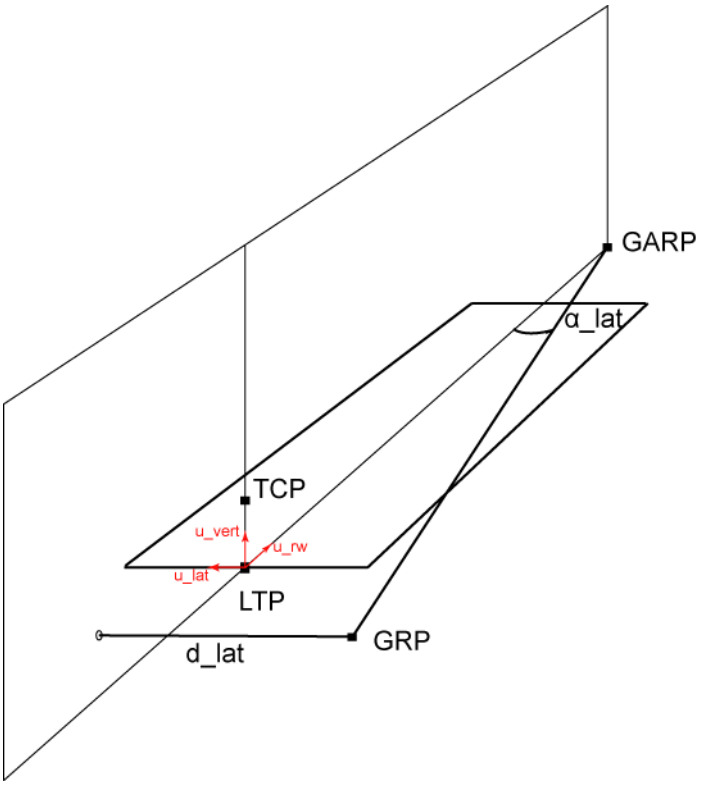

Figure 4 GBAS reference points for lateral deviation calculations, both rectilinear (d_lat) and angular (α_{lat})

In a first step the rectilinear deviation d_{lat} from the localizer plane is calculated in meters and in a second step transformed into an angular ILS look-alike deviation α_{lat}.

$$d_{lat} = \vec{u}_{lat}(\vec{r}_{GRP} - \vec{r}_{GARP}) \tag{8}$$

$$\alpha_{lat} = \tan^{-1}\left[\frac{d_{lat}}{\left|\vec{u}_{rw}(\vec{r}_{GRP} - \vec{r}_{GARP})\right|}\right] \tag{9}$$

The $\vec{r}$ -vectors denote the vectors from the center of the earth to the respective coordinates in an ECEF coordinate system.

The vertical deviations are directly calculated in an angular sense (α_{vert}) and can then be transformed into rectilinear deviations d_{vert} in meters if needed. The inputs into the autopilot, however, are again ILS-like angular deviations.

$$\alpha_{vert} = -\mathrm{GPA} + \tan^{-1}\left[\frac{\vec{u}_{vert}(\vec{r}_{GRP} - \vec{r}_{GERP})}{\sqrt{(\vec{u}_{lat}(\vec{r}_{GRP} - \vec{r}_{GERP}))^2 + (\vec{u}_{rw}(\vec{r}_{GRP} - \vec{r}_{GERP}))^2}}\right] \tag{10}$$

In this formula GPA denotes the glide path angle which is also transmitted in the type 4 GBAS message. The vertical deviations are calculated in this way as deviations from a cone with its tip at the GBAS Elevation Reference Point (GERP) as shown in Figure 5.

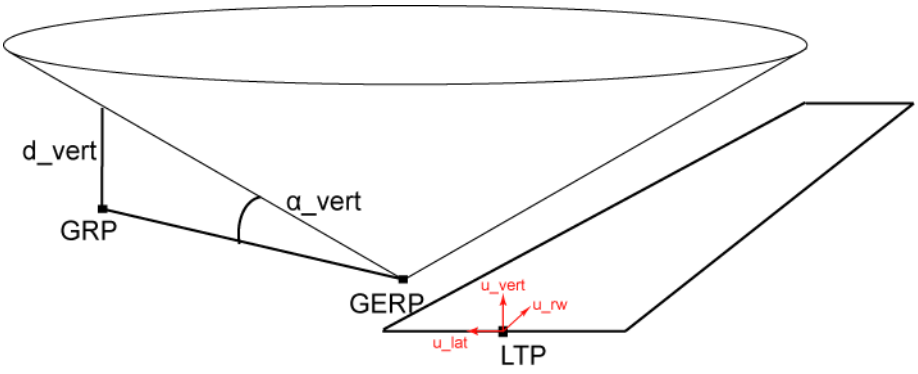

Figure 5 GBAS reference points for vertical deviation calculations, angular (α_{vert}) and rectilinear (d_vert)

As can be seen from the illustration, the defined approach track becomes either a conic section for the case when the GERP is located next to the runway or a straight line if it is located on the runway centerline.

2.2.3 GBAS Airborne System

In this section the data processing in the airborne GBAS system is described. At the aircraft the integrity of the navigation solution is assessed and compared to the relevant constraints. If an alert is triggered an appropriate warning for the pilot and/or an appropriate action from the autopilot such as downgrade to a service type with lower integrity requirements that can still be ensured or the initiation of a go-around has to be performed.

2.2.3.1 Airborne Processing

In this section the general processing in the airborne system is described. GBAS avionics typically consist of a multi-mode receiver (MMR) capable of receiving the GBAS messages from the ground system that are transmitted via a VHF data broadcast (VDB), as well as the GNSS ranging signals from the satellites. While the general process of determining a position is the same in every service type, there are several differences which data from the ground station is used depending on the active service type. The differences in processing are compared at the end of this section. The next section describes the different monitors that are required for the integrity assurance.

The aircraft starts processing the raw pseudorange and carrier phase measurements in the same smoothing filter [34] with the same smoothing time constant as used in generation of the corrections in the ground system described in Equation (2). Using the same filter with the same time constant ensures that no significant differential errors due to filter mismatch between the process of generating the corrections and the airborne processing can arise. The corrections are then applied to the smoothed pseudoranges $\hat{\rho}_n$. This process is described in Section 2.3.8.2 of [38]. The smoothed and corrected pseudoranges $\tilde{\rho}_n$ are obtained as

$$\tilde{\rho}_n = \hat{\rho}_n + TC + PRC + RRC(t - t_{zcount}) + \Delta t_{sv} \tag{11}$$

where $\hat{\rho}_n$ is the smoothed pseudorange, TC is the tropospheric differential correction, PRC and RRC are the pseudorange and range rate corrections from the Type 1 and in case of GAST D also the Type 11 message, t is the current time, t_{zcount} is the time of applicability of the corrections transmitted in the Type 1 GBAS message and Δt_{SV} is the relativistic satellite clock correction term including the relativistic correction. The differential tropospheric correction accounts for the different tropospheric impact at the ground station and the airborne user and is thus a function of the height difference between the aircraft and the GBAS reference point and satellite elevation angle [41]. It is specified in Section 2.3.8.3 of [38] as

$$TC = N_R h_0 \frac{10^{-6}}{\sqrt{0.002 + \sin^2(\theta)}} \left(1 - e^{\frac{-\Delta h}{h_0}} \right) \tag{12}$$

where N_R and h_0 are the refractivity index and the tropospheric scale height transmitted in the Type 2 GBAS message, θ is the elevation angle of the satellite calculated from the satellite ephemeris data and the last position estimate of the aircraft and Δh the height difference between the last calculated position solution and the GBAS reference point. The satellite clock correction term is calculated based on parameters transmitted in the navigation message of the satellites as specified in Section 20.3.3.3.3.1 of the GPS Interface Specifications [46].

2.2.3.2 Position determination

The pseudorange measurements ρ_i still contain the receiver clock offset $c \cdot t_{rx}$ and a residual error ε_i in addition to the geometric range. It can be denoted as the norm of the difference of the 3-dimensional position vectors $\vec{x}^i$ of the satellite i and the user position $\vec{x}_u$ in an earth centered earth fixed (ECEF) coordinate system and the receiver clock offset and additional errors as

$$\rho_i = \left| \vec{x}^i - \vec{x}_u \right| + c \cdot t_{rx} + \varepsilon_i \tag{13}$$

The well-known standard way of GNSS-based position estimating (described e.g. in Chapter 6 of [47]) is based on determining the position and receiver clock bias iteratively by starting with an initial position $\vec{x}_0$ (typically the position of the previous epoch or the center of the earth as initialization if no prior knowledge is available). Based on the initial position $\vec{x}_0$ and an initial clock offset estimate t_0 (initial value typically used is 0) the pseudorange described in Equation (13) can be expressed by a Taylor expansion using the geometrical distance $\rho_{est}(\vec{x}_0)$ between that position and the satellite (omitting higher order terms (h.o.t.)) as

$$\rho\begin{pmatrix}\vec{x}\\ t_{rx}\end{pmatrix} = \rho_{est}\begin{pmatrix}\vec{x}_0\\ t_0\end{pmatrix} + \nabla\rho\begin{pmatrix}\vec{x}_0\\ t_0\end{pmatrix} \cdot \begin{pmatrix}\vec{x}-\vec{x}_0\\ t-t_0\end{pmatrix} + \text{h.o.t.} \tag{14}$$

In the navigation problem $\nabla\rho\begin{pmatrix}\vec{x}_0\\ t_0\end{pmatrix}$ corresponds to the nx4 dimensional geometry matrix $\mathbf{G}$, containing as rows the negative line of sight unit vectors between the position estimate and the satellites and a 1 in the fourth column for the clock offset.

This can be rewritten using matrix notation and $\Delta\boldsymbol{\rho} = \rho\begin{pmatrix}\vec{x}\\ t_{rx}\end{pmatrix} - \rho_{est}\begin{pmatrix}\vec{x}_0\\ t_0\end{pmatrix}$ to include all measurements as

$$\Delta\boldsymbol{\rho} = \mathbf{G}\underbrace{\begin{bmatrix}\Delta\vec{x}\\ c\Delta t_{rx}\end{bmatrix}}_{\Delta\mathbf{x}} \tag{15}$$

This equation is typically solved for $\Delta\mathbf{x}$ using the least-squares method. When there is prior knowledge about the expected ranging errors available (as it is the case in GBAS) an additional weighting can be used. The weighting matrix $\mathbf{W}$ can then be defined to be an *n*x*n* dimensional diagonal matrix containing the inverse of the expected uncertainty associated with each pseudorange measurement as entries. These uncertainties will be described in detail in the next section. The weighted least squares solution is then obtained by

$$\Delta\mathbf{x} = \mathbf{S} \cdot \Delta\boldsymbol{\rho} \tag{16}$$

with

$$\mathbf{S} = \left[\mathbf{G}^T \mathbf{W} \mathbf{G}\right]^{-1} \mathbf{G}^T \mathbf{W} \tag{17}$$

The increment $\Delta\mathbf{x}$ is then added to the previous position and user clock estimate to obtain a new improved position and clock estimate. The process is repeated until the increment is small enough to remain below a predefined threshold. This method usually converges after very few iterations. The residual position error for smoothed and GBAS corrected pseudorange measurements is typically in the range of decimeters only [48], [49]. The projection factors relating the GNSS measurements from satellite i to the position domain in approach coordinates (centered at the aircraft position with the x-axis along the approach path, the y-axis in the lateral direction of the approach track and a perpendicular z-axis) play an important role in the integrity assurance process and are given as

$$s_{vert,i} = s_{3,i} + s_{1,i} \cdot \tan(GPA) \tag{18}$$

where $s_{k,i}$ are the entries of the $\mathbf{S}$-matrix of row k and column i and GPA is the glide path angle of the approach (typically 3°, in the requirement derivation 2.5° are assumed to be conservative).

The just described method is only applicable to single constellation positioning. In case of using a second GNSS constellation the $\mathbf{G}$-matrix becomes an nx5 dimensional matrix, containing not only the geometry part and a column with “1” for the clock offset but two columns with either “1 0” or “0 1” per row to identify the constellation the satellites belongs to. This is necessary as different constellations use their individual time references such that the receiver clock offset to each constellation has to be determined individually. Note that the smoothed pseudorange $\hat{\rho}_n$ can be from either navigation frequency in the single frequency positioning case or a linear combination of pseudoranges from two frequencies, e.g. in order to remove the ionospheric delay. Further details on dual frequency and multi constellation positioning can be found e.g. in [50] and [51].

2.2.3.3 Integrity Assurance

By using differential GNSS methods, precision approach guidance can be accomplished with high accuracy. The performance benefits of GBAS compared to a standard ILS are shown in the next section. For safety of life applications, such as navigation for automatic landings, not only accuracy is important, but especially the integrity, i.e. the trust one can put into the calculated position solution. In GBAS integrity is assured by calculating Protection Levels (PLs) in the lateral and vertical domain (LPL, VPL). These values are conservative bounds of the actual positioning error that can be calculated based on standardized models for different error contributions. Three different protection levels are calculated: one for the fault-free case, one for a single fault case in the ground system and an ephemeris protection level. The maximum of all three is then used in assessing the integrity by comparing the PL to the respective Alert Limit (AL) for a given position on the approach. These ALs ensure that an operation can be conducted safely if the PLs remain smaller than the ALs. The values for the ALs are given in tables 2-14 and 2-15 in DO-253C [38] and are reproduced for convenience in the Appendix I together with a summary of the GBAS performance requirements for the different existing service

types specified in the ICAO Standards and Recommended Practices (SARPS) for GBAS [4]. They have a maximum value at distances larger than 7500 m from the runway threshold (in the vertical case the distance can vary depending on the glide path angle) and then decrease linearly until they reach a constant minimum value at 873 m from the runway. The calculation of the lateral and vertical PLs is completely analog ensuring protection in the vertical and lateral domain, respectively. For readability purposes only the vertical calculations as described in DO-253C are shown here. They do hold only for the single frequency GPS case as this is the currently only validated and operational service. Future GBAS service types including a second frequency and other constellations will have to provide a similar concept. It may be expected that in principle the methodology will remain the same: Modelling and overbounding the expected residual ranging errors per satellite and then projecting them into the position solution. The signals on the second frequencies and from different constellations have different performance in terms of noise and multipath [51], [52] or ionospheric effects [53]. However, work on future GBAS services using two frequencies and multiple constellations is still in the early stages at the time of writing and will be ongoing for several more years to ensure sufficient protection for all potential failure modes.

The PLs for the service types C and D are defined in [38] and are reproduced and described in the following. For the fault free case (denoted by a subscript H0) they are based on the satellite geometry seen by the user and as given by the weighted pseudoinverse of the satellite geometry matrix $\mathbf{S}$, with the $s_{vert,i}$ as previously defined in Equation (18) and the residual uncertainties σ_i associated with each corrected pseudorange measurement and are expressed as

$$VPL_{H0} = K_{ffmd}\sqrt{\sum_{i=1}^{N} s_{vert,i}^2 \cdot \sigma_i^2} + D_v \tag{19}$$

The K_{ffmd} multiplier is the fault-free missed detection multiplier given by the tolerable integrity risk as inflation factor for a Gaussian distributed random variable. The parameter D_v is the vertical position difference between the two position solutions based on 30s and 100s smoothed pseudoranges (see Equation (2)) in GAST D and zero in GAST C. This parameter is important in accounting for the differences between the different smoothing time constants for the two service types C and D. While the GAST C integrity concept and parameters were defined to bound the errors for 100 seconds smoothing, the D_v term accounts for the differences resulting from the shorter smoothing time constant (30 seconds) used in GAST D and the somewhat larger residual errors and uncertainties in the smoothed pseudorange measurements. The variances of the standard deviations associated with the residual uncertainties are calculated as

$$\sigma_i^2 = \sigma_{pr,gnd,i}^2 + \sigma_{pr,air,i}^2 + \sigma_{tropo,i}^2 + \sigma_{iono,i}^2 \tag{20}$$

The individual variances are calculated based on the integrity parameters transmitted from the ground station as described in the previous section. The contribution from the ground station $\sigma_{pr,gnd,i}$ depends

on the active service type. The appropriate value is taken directly from the GBAS message. The $\sigma_{pr,air,i}$ describe the uncertainty introduced by the airframe multipath and airborne receiver noise, and depend on the airborne equipment classification. The tropospheric uncertainty is described as

$$\sigma_{tropo} = \sigma_n h_0 \frac{10^{-6}}{\sqrt{0.002 + \sin^2(\theta)}} \left(1 - e^{-\Delta h / h_0}\right) \tag{21}$$

with the refractivity uncertainty σ_n, the tropospheric scale height h_0, the elevation angle of the satellite θ and the height difference between the aircraft and the GBAS reference point Δh. The first three parameters are transmitted by the ground station, while the last one is calculated based on the current position of the aircraft. The ionospheric uncertainty is described as

$$\sigma_{iono} = F_{pp} \cdot \sigma_{vig} \cdot (x_{air} + 2\tau v_{air}) \tag{22}$$

with the vertical-to-slant obliquity factor F_{pp}, the standard deviation of the residual ionospheric uncertainty due to spatial decorrelation σ_{vig} the slant distance between the aircraft and the GBAS reference point x_{air}, the smoothing time constant τ and the horizontal speed of the aircraft v_{air}.

In addition to the PLs for the fault free case, PLs accounting for a single faulted reference receiver in the ground subsystem are calculated. They are calculated for each ground reference receiver j as

$$VPL_{H1,j} = \left|B_{j,vert}\right| + K_{md}\sigma_{vert,H1} \tag{23}$$

with the missed detection multiplier K_{md} determined by the associated integrity risk and the following parameters:

$$B_{j,vert} = \sum_{i=1}^{N} s_{vert,i} \cdot B(i,j) \tag{24}$$

are the B-values (see Section 2.2.2.3.2) from the Type 1 GBAS message projected into the position domain and

$$\sigma^2_{vert,H1} = \sum_{i=1}^{N} s^2_{vert,i} \cdot \sigma^2_{i,H1} \tag{25}$$

with $\sigma^2_{i,H1} = \left(\frac{M(i)}{M(i)-1}\right)\sigma^2_{pr,gnd}(i) + \sigma^2_{pr,air}(i) + \sigma^2_{iono}(i) + \sigma^2_{tropo}(i)$ and $M(i)$ the number of reference receivers used for the generation of the corrections. The VPL_{H0} is defined as the maximum over the $VPL_{H0,j}$.

The third type of protection levels is bounding GBAS positioning errors due to ephemeris errors. They are given for the vertical case as

$$VPL_{eph} = \max(VPL_{eph}(i)) + D_v \tag{26}$$

The D_v are the same as before and the individual PLs $VPL_{eph}(i)$ for each satellite i are defined as

$$VPL_{eph}(i) = \left| s_{vert,i} \right| \cdot x_{air} \cdot P_k + K_{md,eph} \sqrt{\sum_{i=1}^{N} s_{vert,i}^2 \sigma_i^2} \tag{27}$$

with the service type dependent ephemeris decorrelation parameter P_k transmitted in Type 1 GBAS message. The missed detection multiplier $K_{md,eph}$ is chosen according to the allocated integrity budged for the ephemeris fault and all other parameters are the same as previously defined.

All protection levels are compared against the alert limit at the current position and the service is set unavailable if they are exceeded. As it was already mentioned where appropriate, some of the parameters depend on the active service type used for the approach. The reason for that is a slightly different task allocation between the airborne and the ground system in the two service types which is further explained in the following.

2.2.3.3.1 GAST-C

In the case of GAST C it is the sole responsibility of the ground station to bound the error at the output of the airborne receiver. This is achieved by a geometry screening on the ground where potential subsets of usable satellites are evaluated to determine the worst geometry which may be used in an airborne receiver at any decision point i.e. the point on the approach where the decision height is reached. Then the largest vertical error introduced by an ionospheric front (the largest potential error source in GBAS, further described in Chapter 5.3) is determined and compared to an error limit for which the operation is still considered safe [5]. If geometries exist which could generate a larger error, the ground station has to artificially inflate one or more of the broadcast integrity parameters (typically σ_{vig} and/or σ_{gnd} are the parameters that are inflated) to increase the protection levels beyond the alert limit and thus to make these geometries unavailable to the user [54], [43]. This strategy assumes that the worst case ionospheric disturbance that was ever observed in the region where GBAS service is provided is always present. This is an extremely conservative assumption but is used to ensure integrity. However, a price has to be paid for that conservatism in form of a significant impact on the availability of the system in regions where large gradients have been observed. For mid-latitude regions like Europe or the US the impact on availability is small, however, in equatorial countries, such as Brazil, the largest observed gradients were so significant that assuming the presence of the worst case gradient reduces the availability to levels that are far below operational needs.

2.2.3.3.2 GAST-D

For GAST D the integrity concept is somewhat different. More stringent requirements have to be met for automatic landings with an integrity budget two orders of magnitude smaller than for CAT-I approaches. The rationale for that is that no credit can be taken for the flight crew detecting an abnormal situation by visual reference in CAT-II/III weather conditions. Reusing the GAST C architecture with even tighter required error bounds cannot support this service with reasonable availability. Hence, a different strategy has been adopted which shares the responsibility of detecting and mitigating the ionospheric threat between the ground and the airborne system. For this purpose the protection level

concept has been modified and further monitors have been included in both, the ground and airborne systems. These monitors were designed to ensure that GBAS navigation can protect a user from all known fault modes with the required probability. An in-depth discussion about the requirement follows in Section 3.1 and the known fault modes are described in Section 3.3.2. The most significant changes from GAST C to GAST D are:

The geometry screening process is now also performed at the airborne receiver in such a way, that the largest projection factor from the S-matrix and the sum of the largest two projection factors are limited [55]. This measure limits the largest impact a single ranging error on one pseudorange measurement can have on the position solution. The actual limit is a function of the autopilot performance and is determined in the airworthiness approval for each aircraft type individually. For GAST-D it is generally assumed that the projection factors are limited to $s_{vert,i} \leq 4$ or even smaller values if necessary. It is the task of the aircraft manufacturer to show that the aircraft can meet the autoland requirements that are later described in Section 3.1, with the geometry screening implemented.

The Code Carrier Divergence (CCD) monitor and the Dual Solution Ionospheric Gradient Monitoring Algorithm (DSIGMA) were added to the GAST D architecture. Both can detect a temporal ionospheric gradient which affects one or more satellites seen by the aircraft. The CCD monitor acts on each pseudorange and associated carrier phase measurement. A fast change in the ionospheric condition is detectable since the ionosphere is a dispersive medium and affects the code and the carrier in different ways. Flying through a region affected by an ionospheric gradient in such a way that there is a temporal change in the experienced ionospheric delay can be detected by this monitor [51]. The pseudorange DSIGMA algorithm compares two different smoothed and corrected pseudoranges: one determined by a smoothing time constant of 30 s and with 100 s smoothed and corrected pseudoranges. A fast change in the experienced ionospheric conditions that is not reflected by the corrections from the ground system would built up faster in the 30 s smoothed solution than in the 100 s smoothed solution and the two pseudoranges would drift apart which is detected by the pseudorange DSIGMA [56]. From the pseudoranges with the two different smoothing time constants two different position solutions are calculated. The vertical and lateral position difference of those solutions are named D_v and D_l, respectively, and are used in the protection level calculations. In the protection level calculations (previously described by Equations (19), (23) and (26) the σ_i are determined based on the assumption of 100 s smoothing. The position solution used in GAST D is, however, the one based on 30 s smoothing. The measured pseudoranges and received corrections therefore contain more residual errors introduced by noise and multipath. The D_v and D_l terms therefore are added in order to account for the slightly too optimistic assumption of the residual errors in σ_i.

The calculation of the Protection Levels differs from that in GAST C by applying different integrity parameters. Since the responsibility for detection of ionospheric disturbances is now partially shifted from the ground to the airborne system, the ground station does not inflate the broadcast values any-

more to protect the user. The onboard CCD and DSIGMA are now responsible for detection of ionospheric disturbances on the board side. Hence, smaller values for the integrity parameters can be used for calculation of the protection levels which leads to an increased availability. This method reduces the conservatism of assuming that an ionospheric front is present at any time by adding additional monitoring effort. In GAST D the 30 s smoothed position solution will be used to develop guidance on the approach in order to reduce filter initialization time and achieve faster (re-)inclusion of satellites. This also leads to a slightly increased availability and better performance of the system.

The airborne system can only detect temporal ionospheric gradients. An anomaly which appears stationary to the aircraft (i.e. the ionospheric pierce points as seen from the aircraft would travel in the same direction and the same speed as the front) would not be detectable with the aforementioned monitors. This requires the ground subsystem to monitor for absolute ionospheric gradients. This is a challenging task that will be described in detail in Section 5.4.1 of this work. Section 5.4.2 then presents an alternative new way how this problem can be addressed.

When used in concert all monitors provide the required integrity to make use of the improved guidance performance of GBAS. The integrity concepts as they have been developed for GAST C and D ensure integrity but cannot provide a sufficient level of availability of the GBAS service in all regions of the world. Future service types are currently being developed in order to cope with this problem.

2.2.3.3.3 Future service types

Future GBAS service types, including multi frequency and multi constellation techniques, will have their own specific sets of monitoring schemes to address the specific threats arising for a specific way of processing the signals. Modelling of the expectable performance in terms of noise and multipath behavior of different signals is currently ongoing [57]. In addition to the previously known and considered fault modes new ones can also arise and will have to be handled appropriately. In the case of using more than one frequency a way of accounting for satellite specific inter-frequency biases has to be determined for example [58]. At this time there is no decision made as to which potential future service types there could be. This is subject to significant trade-off studies between performance, complexity and benefits of different methods that are to be performed in the coming years.

A single frequency positioning, dual frequency monitoring and multi constellation based GBAS architecture is one special case and a likely candidate for a future service type. A monitoring for ionospheric gradients would be a necessary part of the integrity scheme. Such a monitor is therefore developed and presented as part of this work later in Section 5.5.

2.3 Comparison of GBAS and ILS Guidance

In this section GBAS guidance is compared to the currently used guidance based on ILS. Satellite navigation allows a lot more flexibility than navigation based on conventional navigation aids and is much more precise at the same time. After having described GBAS based positioning and integrity assurance, this section discusses advantages of GBAS from an operational perspective and shows a performance comparison to ILS in flight trials.

2.3.1 Potential

The broadcast FAS data in the Type 4 message contain the coordinates of the runway threshold and information about the glide path angle. Those parameters can be used to define approach trajectories to displaced thresholds on the same runway by simply defining two sets of reference coordinates. A displaced threshold bears the potential to increase runway capacity due to reduced sequential spacing of aircraft for wake turbulence. An increased glide path angle can be used for the whole approach to increase the height at which populated areas under the final approach track are overflown. Advanced final approach tracks, such as segmented steep approaches can be implemented where the final approach segment is intercepted from above instead of below. This can be achieved by broadcasting the same set of reference coordinates with two different glide path angles for different parts of the approach and also bears the potential to increase the height of aircraft over certain parts of the final approach. It is also foreseen that GBAS can broadcast Terminal Area Paths (TAPs) which consist of straight and curved (radius to fix) segments which allow a simple definition of curved approaches. All these measures can be used for a reduction of noise on the ground in the vicinity of an airport.

Other than ILS, GBAS is not sensitive to signal reflections of preceding aircraft on the approach or to aircraft close to the runway. Potential signal reflections and distortions from other aircraft require increased spacing of aircraft on the final approach and larger clearance areas in the vicinity of the runway during low visibility operations. This reduces the capacity of airports and often leads to large delays and flight cancellations. Due to navigation based on corrected satellite signals, those operational constraints are not necessary anymore and can be used to increase the capacity of an airport also in low visibility conditions.

2.3.2 Performance in flight trials

The error characteristics of GBAS are very different from those of ILS. Typically, GBAS errors are small and bias like over one approach and contain very little noise due to the code-carrier smoothing described in Equation (2). In this section, a comparison between GBAS and ILS performance on the final approach is shown. The results are derived from flights conducted in a flight trial with an Airbus

A320. Four approaches to runway 26 at Braunschweig are analyzed. They were conducted in December 2011 within a DLR internal project. The results shown here constitute one original contribution of this thesis. They were originally published in [16] and expanded in [7] and are reproduced here in the remainder of this section. The figure numbers, equation numbers and references were changed from the original to conform to the notation in this work.

"*To analyze the results, we computed a dual frequency carrier phase reference solution using Novatel GrafNav. GrafNav is a surveying software, which employs a positioning technique based on highly precise carrier phase measurements and kinematic ambiguity resolution. The accuracy of the carrier phase reference trajectory is typically in the range of few centimeters, however less robust than GBAS navigation. For this reason, some reference data points were excluded where quality checks failed and not enough trust could be put in the correctness of the reference point. We used the truth reference to compute the error of the two navigation systems by subtracting the deviations that were actually observed by the ILS and GBAS during the flights from the ones that should be indicated based on the true position. Angular information was used for guidance and the indication on the flight instruments. Hence, an angular error would be directly visible for the pilot. However, from a scientific point of view the absolute error in meters throughout an approach was of greater interest. It bears the potential for improved aircraft guidance and control as well as procedural advantages in parallel approach tracks due to the independence of guidance quality from the distance to the runway. To compute the position error in meters for the ILS, we transferred the angular glideslope and localizer deviations into a local coordinate system based on the distances to the two ILS transmitters.*

In Figure 6 *through Figure* 8 *the data calculated from the GBAS position solution are shown in red, while the ILS measurements are depicted in blue. The published glide path angle for runway 26 in Braunschweig is 3.5°. During data evaluation we found an offset in the angular vertical deviations of the ILS which could be removed when using a 3.45° GPA instead. We consulted the obtained results with Flight Calibration Services in Braunschweig who found the results plausible and within the range of expectation. This deviation of 0.05° is still in accordance with the FAA Order* [59] *about determination of the ILS glide path angle and ICAO Annex 10, Chapter 3.1.5.1.1. Figure* 6 *and Figure* 7 *have a grey maker to show results if calculation had been based on the published GPA of 3.5° instead of the 3.45°. On the localizer display in the cockpit a full-scale deflection of the indicator is equivalent to a deviation of ±2.5° or more from the centerline, the glide slope indication is significantly more sensitive and already shows a full-scale deflection at ±0.5°.*

A clustering behavior of the data points can be observed in Figure 6 *for both systems, but at a larger scale in the GBAS data. This is showing the strong temporal correlation of errors in GBAS. The angular deviation error for the ILS glideslope and localizer scatters around the means* μ_{LOC}*=0.005° and* μ_{GS}*=-0.004° with standard deviations of* σ_{LOC}*=0.02° and* σ_{GS}*=0.02°, respectively. These values are smaller by an order of magnitude for GBAS with standard deviations of* $\sigma_{GBAS,lat}$*=0.001° and* $\sigma_{GBAS,vert}$*=0.004° and mean values of* $\mu_{GBAS,lat}$*=0.001° and* $\mu_{GBAS,vert}$*=0.003°. While the GBAS errors are*

clustered very well around the origin and remain below 0.015° vertically and 0.01° laterally, ILS errors spread up to +0.04°/-0.1° vertically and ±0.08° laterally. Possible sources of these errors include aircraft on the ground as well as on the approach, buildings and airport installations as well as seasonal variations [60]. *To our experimental pilots the deviations looked normal throughout the approaches.*

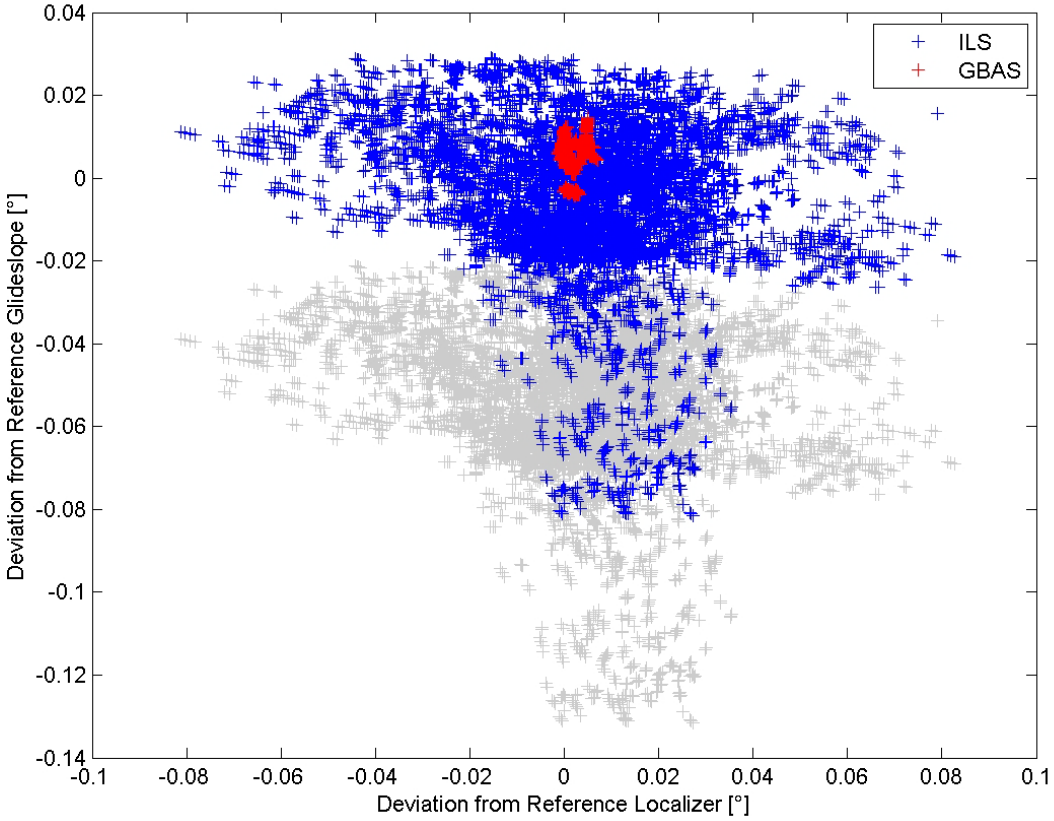

Figure 6 *Comparison of the angular deviation errors of the two guidance systems ILS and GLS with respect to a post processed carrier phase truth reference. The plot shows the data from four approaches. GBAS is much more accurate and shows less noise than ILS. The grey data points show the results if the published 3.5° GPA is used instead of the 3.45° as we determined.*

Figure 7 *and Figure* 8 *show the absolute errors of the glide slope and the localizer in meters. The origin of the coordinate system was located at the LTP; therefore negative x-values occurred before overflying the threshold. The analog VHF signals of the glide slope transmitter showed rather large deviations reaching up to almost 8 m but decrease towards values in the range of 1-2 m as the aircraft approaches the airport.*

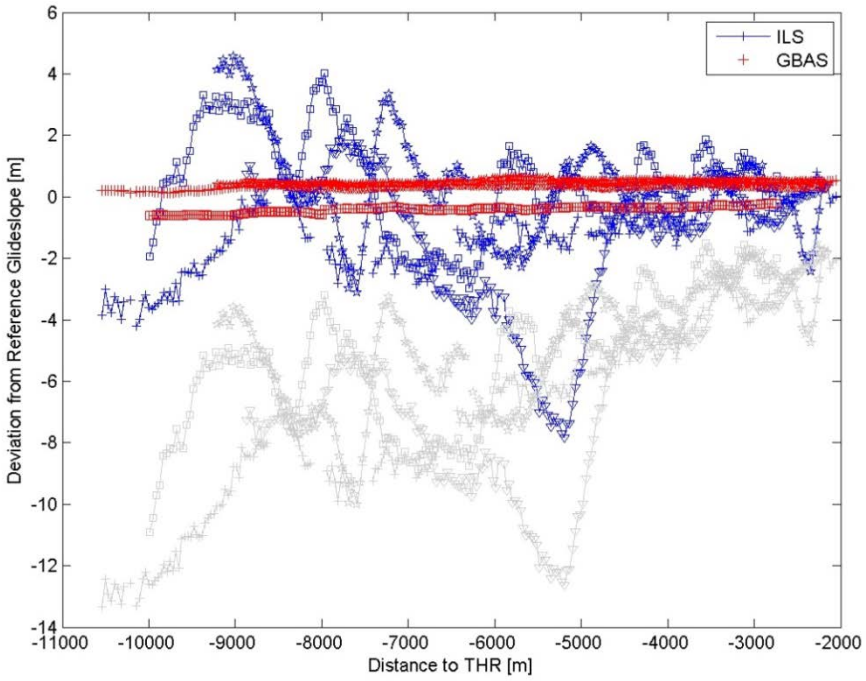

Figure 7 Distance dependence of the glide slope deviation errors. The plot shows the data from four approaches. Each marker type denotes a different approach. The grey data points show the results if the published 3.5° GPA is used instead of 3.45° as we determined. A different marker type for the data points was used for each of the approaches.

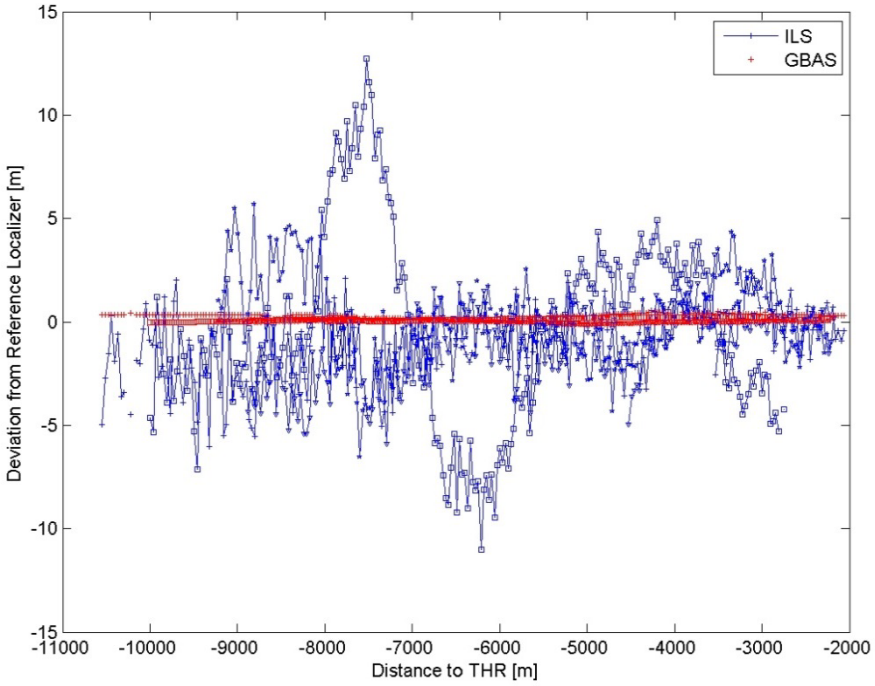

Figure 8 Distance dependence of the localizer deviation errors. The plot shows data from four approaches. Neither signal shows strong distance dependence but the ILS signal is much noisier and also shows a sinusoidal oscillation. Each marker type denotes adifferent approach.

Error characteristics of the GBAS are different from the ILS in that they appear bias-like over the time of an approach with a very low noise level. The absolute value of the errors stays below 0.75 m at all times. The offset of the boxed markers for the GBAS case in Figure 7 occurs due to a constellation

change with respect to the other three approaches shown here. During those three approaches the same satellites were available and used for guidance. The ILS glide slope mean error μ_{GS} *=-0.4 m and GBAS mean error of* $\mu_{GBAS,vert}$*=0.25 m observed during the four approaches are small and do not show a significant bias in the calculations for GBAS and the ILS measurements. The same holds for the ILS localizer error with a mean of* μ_{LOC}*=-0.75 m and* $\mu_{GBAS,lat}$*=0.12 m, respectively. The situation looks different, however, when investigating the standard deviations of the errors. While the observed GBAS standard deviations vertically* $\sigma_{GBAS,vert}$*=0.4 m and laterally* $\sigma_{GBAS,lat}$*=0.1 m are very small, the corresponding values for the ILS* σ_{GS}*=1.9 m and* σ_{LOC}*=2.9 m are several times larger.*
In Figure 8 *we can see that during the approach depicted by the boxed markers, an undulation appears in the signal at a distance from 8500 to 5500 meters from the threshold. This was possibly caused by construction vehicles working on an extension of the runway during the approach. At the same time, GBAS does not show any signs of signal deformation. All GBAS monitors were active during the flight and performed to expectation. No alerts were triggered and the system was fully available at all times.*“ [7].

The comparison of ILS and GBAS performance during the approaches shows a significantly better performance of the GLS in terms of noise, absolute errors and guidance signal stability. The GBAS standards for CAT II/III services as they are now agreed upon and are discussed in detail in the following chapter, provide an availability of GBAS service which will likely not meet the availability of current ILS installations. This results from partially overly conservative assumptions. The following chapters show the process of the derivation of the requirements and suggest certain changes in order to leverage the improved performance of GNSS based guidance which was discussed in this chapter.

3 REQUIREMENTS

In this chapter the relevant requirements for automatic landings are summarized from the different applicable standards. Most of them originate from the definition of a safe landing as described in the European certification specifications for all weather operations and the FAA advisory circular AC-120 28B. It has to be shown that the aircraft can land in a dedicated area on the runway with a given, very high probability under nominal conditions as well as in certain limit and fault cases.

This total error budget on aircraft level is then allocated between the flight technical error, relating to autopilot performance in automatic landings, and the navigation system error, relating to GBAS in the context of this discussion. On the navigation side, this budget is then further allocated between the ground and the airborne GBAS sub-systems resulting in specific low-level requirements for specific failure modes. The requirement derivation and allocation between the different systems is described in this chapter.

The last section is a critical review of the derivation process and suggests possible changes to the process where appropriate. This can yield relaxed monitoring requirements and has the potential to enable a better allocation of the total error budget between the relevant systems and components. The concepts described here are used for deriving ground and airborne GBAS monitoring architectures that are described in Chapter 5.

Contributions:

The derivation process for the relevant GBAS ground monitoring requirements is critically reviewed and suggestions are made for changes in order to relax the requirements without compromising safety. The relaxations are based on the proposal to use available knowledge where possible instead of making conservative assumptions.

Publications:

- M. Felux, J. Lee and F. Holzapfel, "GBAS ground monitoring requirements from an airworthiness perspective," *GPS Solutions*, vol. 19, no. 3, pp. 393-401, 7 2014. [14]

The International Civil Aviation Organization (ICAO) develops and publishes globally harmonized international Standards and Recommended Practices (SARPs) which usually form the basis of the legally binding national regulations. In terms of GBAS and this work, the most relevant part of the ICAO SARPs is Annex 10 to the Chicago Convention which relates to Aeronautical Telecommunications, and more specific Volume 1 which covers radio navigation aids [4]. The currently published version includes the standards for CAT-I GBAS (or GAST C), the standards for GAST D (CAT-II/III GBAS) are agreed upon and will take effect in 2018 [3].

The development of those GBAS standards was originally based on showing that GBAS performance is not worse than ILS performance and is thus suitable for approach and landing guidance. This was successful for the CAT-I case, however, extending this strategy for the CAT-II/III was not feasible [6]. In that case, system performance would be restricted too much, resulting in unacceptably low availability of the system. Instead, the adopted strategy to derive the requirements is based on ensuring a safe landing. The definition of a safe landing and the relevant parameters are defined at aircraft level and are further described in Section 3.1.

From that definition which is an airworthiness requirement, the total error budget is allocated to different subsystems as shown in Figure 9.

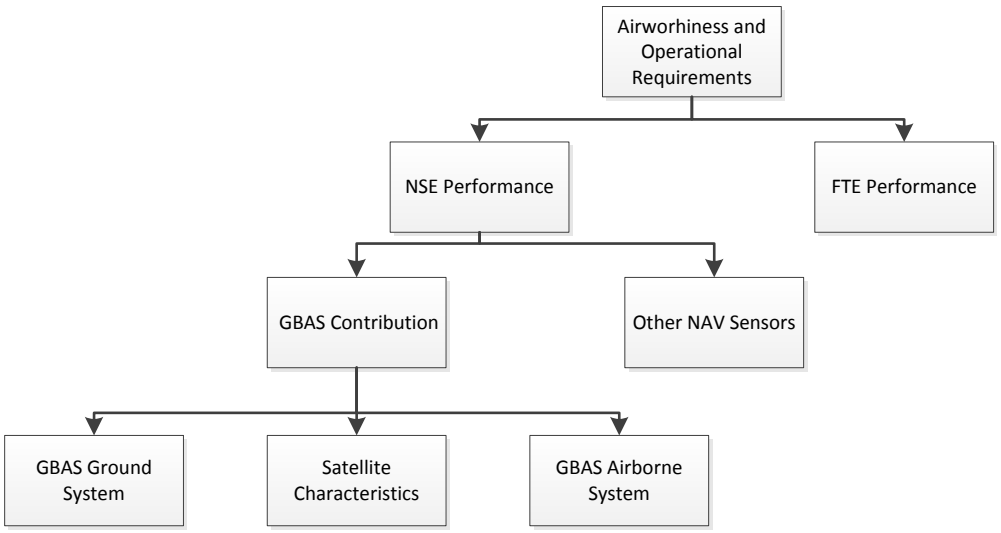

Figure 9 Requirement and principal error budget allocation reproduced from [13]

The performance requirements at aircraft level are allocated between the flight technical error (FTE) and the navigation system error (NSE).

The NSE contribution is then split into the contribution from GBAS and other aircraft navigation sensors, such as the radar altimeter which is initiating and guiding the flare manoeuver and the inertial sensors which are necessary for continuity in case of an unpredicted GBAS outage. Within GBAS, the budget is further allocated between the GBAS ground station at the airport, satellite characteristics and the airborne GBAS subsystem. The individual parts are all described in the next sections.

In the derivation of NSE requirements the FTE performance is considered to be fixed and equal for all aircraft. For many aircraft in many situations this leads to very conservative assumptions while the actual performance would be much better. One of the main goals of this work is thus to reduce conservatism in the derivation of requirements by using available information, such as type of aircraft or approximate mass and location of the center of gravity when landing.

3.1 AIRWORTHINESS AND OPERATIONAL REQUIREMENTS

The relevant requirement documents defining high-level performance requirements on aircraft level are the Certification Specifications for All Weather Operations (CS-AWO), Book 1 in CS-AWO 131 for Europe [9] and the Advisory Circular AC 120-28D, Appendix 3 for the United States [10]. Both documents describe the nominal case and the influencing parameters which need to be considered. CS-AWO contains requirement also for a so-called limit case scenario and AC 120-28D (Section 6.4.1) contains specifications for the case of a malfunction. All those cases are further described in this section.

The definition of a safe landing mainly requires the aircraft to touch down in a box at the runway with a very high probability. The longitudinal touchdown point (i.e. along the runway in flight direction) must not be less than 60 m (200 ft) behind the threshold and not beyond 823 m (2700 ft) behind the threshold. Note, that 200 ft actually equals 60.96 m, so that slightly different results occur if using a limit of 200 ft or of 60 m behind the threshold. Throughout this work, the 200 ft limit is used as it is the slightly more constraining conditions. In the limit and fault case the land long limit is increased to 914 m according to CS-AWO and 1000 m according to AC 120-28D (3000 ft) behind the threshold. The difference between 914 m and 1000 m is quite significant and may result in different monitoring limits. In the classical derivation, the land short case is usually the limiting condition. Thus, the difference in the specified land long limits may not have an effect. However, when using an improved modelling (as will be described later in Section 4.4 of this work), the differences may be significant. Throughout this work, again the more constraining value of 914 m is used. The lateral limit is given as 21 m (70 ft) from the runway center line (which means 1.5 m (5 ft) from the edge of the runway) for the outboard landing gear. This requirement is based on an assumption of a 45 m (150 ft) wide runway and “may be appropriately increased if operation is limited to wider runways” [10]. The area where the aircraft should land (the “touchdown box”) is illustrated in Figure 10.

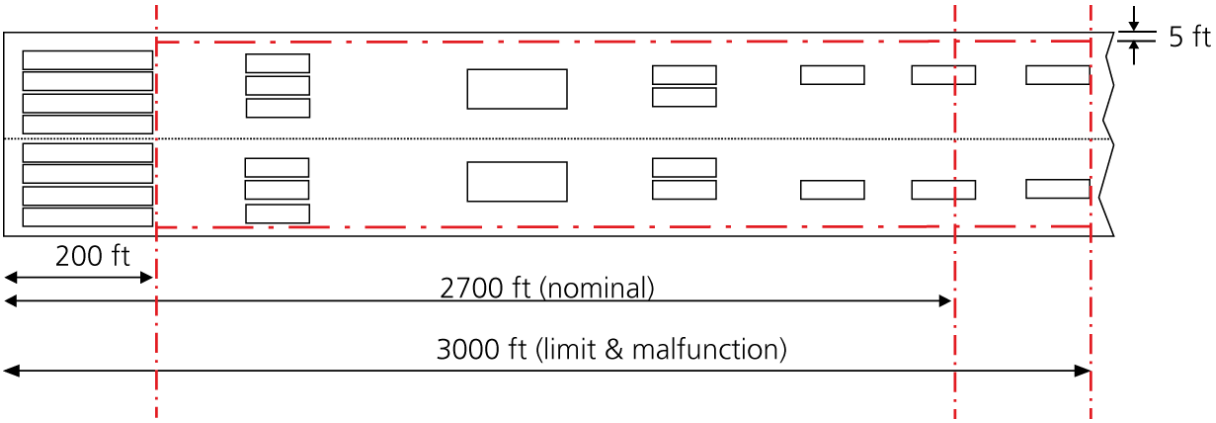

Figure 10 Illustration of the touchdown box

The definition of a safe landing also comprises limitations on the maximum sink rate which must not exceed the structural load limit of the airframe, the maximum bank angle which must be such that no part of the aircraft (e.g. engine or wings) touches the ground and the lateral velocity or slip angle which must not exceed the limitations of the aircraft.

Compliance with this requirement has to be shown for each aircraft in a combination of simulations and flight trials. Appendix 3 of AC 120-28D and CS-AWO 131 and 132 state the variables which have to be taken into account for these simulations.

Influencing Parameter
(a) Configurations of the airplane (e.g. flap/slat settings)
(b) Center of gravity
(c) Landing gross weight
(d) Conditions of headwind, tailwind, turbulence and windshear [..]
(e) Characteristics of applicable navigation systems and aid, variations in flight path definitions [..]
(f) Airport conditions (elevation, runway slope, runway condition)
(g) Approach airspeed and variations in approach airspeed
(h) System tolerances

Table 3-1 Contributing factors to landing performance reproduced from [9] and [10]

Variables (a)-(f) are common to both documents. Parameter (h) is specific to CS-AWO and parameter (g) specific to AC 120-28D.

Appendix 4 of AC 120-28D and Book 2 AMC AWO 131 of CS-AWO include the wind conditions to be considered in simulations. These will be further discussed in Section 4.4.1 of this work where the autoland simulations and the wind effect are described and discussed in detail.

3.1.1 Nominal Case

The nominal case is defined as the situation where all influencing parameters from Table 3-1 vary according to their expected distributions. Conditions which are changing significantly during one approach, and thus have a large influence on the variation of the touchdown point, are mainly wind and the characteristics of the navigation system. The total probability of an unsuccessful landing, i.e. that the aircraft lands outside of the touchdown box (200 ft – 2700 ft behind the runway threshold in longitudinal direction), or does not meet any other condition for a safe landing has to be smaller then 10^{-6}.

3.1.2 Limit Case

The limit case is defined as the situation where one of the parameters from Table 3-1 is "held at its most adverse value, while the other parameters vary according to their" [9] nominal distributions. Exceeding the touch down limits must be "improbable", i.e. smaller than 10^{-5} according to the definitions of AMC-25.1309 in [61]. It is not specified further what exactly is meant by "most adverse" value. The main focus within Chapter 5 of this work is put on the navigation system, i.e. item (e) from Table 3-1. The way the requirement is interpreted within this work is that a bias in the position domain exists as a result of an error condition. No monitoring limits are exceeded but one specific monitoring limit is reached. The limit condition requires that the probability of an unsuccessful landing, given an error exists, is smaller than 10^{-5}. In terms of the landing box requirement this means that the probability of landing less than 200 ft behind the runway threshold and the probability of landing further than 3000 ft behind the threshold both have to be smaller than 10^{-5}. Note that the land long limit is extended by 300 ft from the nominal case and the tolerable risk of landing outside the box is increased by a factor of 10.

3.1.3 Malfunction Case

In the malfunction case, described in Section 6.4.1 of AC 120-28D Appendix 3, a single malfunction in a fail operational automatic landing system may not lead to an unsuccessful landing. Unsuccessful in this case means not landing within the touchdown box which for the malfunction case starts at 200 ft behind the threshold and ends at 3000 ft behind the threshold, i.e. it is again prolonged by 300 ft compared to the nominal case. The limitations for the lateral dimensions of the box, as well as the requirements concerning structural load limits and bank angle at touchdown remain unchanged from the nominal case. A fundamental difference to the nominal case is the requirement that the aircraft must be able to land within the box with certainty and not anymore with a given very high probability (e.g. $1\text{-}10^{-6}$ as for the nominal case). Of course, when assuming that the along-track error at touchdown can be described by a Gaussian distribution this condition can never be fulfilled as there is always some residual risk to land outside the box. Therefore, the malfunction analysis "may be considered

under nominal environmental conditions" [10]. This statement is not clarified any further as to what can be considered "nominal". In [62] it was shown that fixing the parameters at the 95th percentile is sufficient. In the process of deriving the requirements within this work, the same assumption is used.

These performance requirements for the nominal, limit and malfunction case all relate to the total system error (TSE), i.e. to performance at aircraft level. Now the total error budget has to be allocated between the different contributing subsystems.

3.2 AIRCRAFT FTE REQUIREMENTS

One portion of the TSE budget has to be attributed to the performance of the autopilot. The corresponding error is called flight technical error (FTE) and, in this context of touchdown performance in airworthiness assessments, is given in form of a standard deviation of a Gaussian distribution which describes the along-track dispersion of the touchdown point relative to a nominal touchdown point (NTDP). It is commonly assumed that the FTE and navigation system error (NSE) are both Gaussian distributed and statistically independent. For the FTE, the Gaussian assumption could not be confirmed within this work as will be shown later in Section 4.4. It is, however, shown that a Gaussian overbound can be used to describe the FTE, such that the contribution of the autopilot to the total probability of landing outside the touchdown box is not underestimated. Due to the error characteristics of GNSS-based navigation, modelling the NSE (or its overbound) by a zero mean Gaussian distribution appears to be a valid assumption. Assuming now that a description of the NSE and FTE by two Gaussian distributed random variables is appropriate, the variance of the TSE is then given as

$$\sigma_{TSE}^2 = \sigma_{NSE}^2 + \sigma_{FTE}^2 \tag{28}$$

This equation shows that there is a trade-off between the NSE and FTE performance of the aircraft. The better the FTE performance, the more NSE could be tolerated and vice versa. From an airworthiness perspective the condition which has to be fulfilled is the touchdown requirement (TSE requirement) in the three different cases detailed in Section 3.1. The resulting required FTE performance in all cases is described in the following sections. In this section the most stringent FTE requirements are determined by using a largest permissible NSE. It results from the largest nominal vertical error which is given by the VAL according to Equation (19) as

$$\sigma_{vert} = \frac{VAL}{K_{ffmd}} \tag{29}$$

A larger σ_{vert} would result in a VPL larger than VAL and would thus make GBAS navigation unavailable. For the limit and malfunction case additional undetected errors are assumed in addition to the nominal vertical NSE. The total vertical error is then transformed into an along track error by a divi-

sion by the tangent of the glide path angle. This assumption is justified by the fact that in an automatic landing the flare is initiated at a certain height above ground which is measured by the radar altimeter. The radar altitude is independent of the GBAS calculated altitude above the runway and thus a vertical bias in the GBAS navigation solution would result in an along track error due to early or late initiation of the flare. Note that for satellite geometry reasons the vertical performance in GNSS based navigation is generally worse than lateral performance. At the same time the performance requirements for vertical errors are much more stringent than for lateral performance. Hence, discussions here are limited to the vertical case since lateral performance requirements are assumed to be met whenever the vertical conditions are fulfilled.

3.2.1 Nominal case FTE constraints

In the nominal case the probability of landing less than 200 ft behind the runway threshold and the probability of landing more than 2700 ft behind the threshold must be less than 10^{-6} for both cases individually. Formulating these conditions in a probabilistic way yields the following conditions for an unsuccessful landing (UL) and thus for the standard deviation of the along-track TSE dispersion for the land-short case:

$$k \cdot \sigma_{TSE} \leq NTDP - 200\,ft \tag{30}$$

and similarly for the land long case:

$$k \cdot \sigma_{TSE} < 2700\,ft - NTDP \tag{31}$$

The k -factor in both equations is the same. It results from the probability p_{UL} of not landing inside the touchdown box and is thus given as

$$k = Q^{-1}(p_{UL}) = Q^{-1}(10^{-6}) = 4.75 \tag{32}$$

with $Q(x) = \frac{1}{\sqrt{2\pi}} \int_{-\infty}^{x} e^{\frac{t^2}{2}} dt$. Using the condition from Equation (28) for σ_{TSE} , and solving Equations (30) and (31) for σ_{FTE} the condition for the land short case can be formulated as

$$\sigma_{FTE} \leq \sqrt{\left(\frac{NTDP - 200\,ft}{k}\right)^2 - \left(\frac{VAL \cdot 3.28\,{}^{ft}\!/_{m}}{K_{ffmd} \cdot \tan(GPA)}\right)^2} \tag{33}$$

and for the land long case as

$$\sigma_{FTE} \leq \sqrt{\left(\frac{2700\,ft - NTDP}{k}\right)^2 - \left(\frac{VAL \cdot 3.28\,{}^{ft}\!/_{m}}{K_{ffmd} \cdot \tan(GPA)}\right)^2} \tag{34}$$

From Equations (33) and (34) it is obvious, that the aircraft performance needs to meet certain minimum performance characteristics which depend on the size of the VAL. The larger VAL becomes the less stringent the requirement on the FTE of the aircraft becomes. For that reason the VAL for the Final Approach Segment is limited to a maximum of 10 m but can also be decreased for an individual

approach where necessary. Figure 11 shows the resulting constraint region assuming a VAL of 10 meters, a K_{ffmd} of 5.847 (corresponding to a four reference receiver GBAS with the associated integrity risk as per table 2-16 in [38] and a glide path angle of 2.5° which is the minimal and thus worst case GPA for precision approaches. The area below the green curve shows allowable combinations of NTDP and σ_{FTE} in the nominal case.

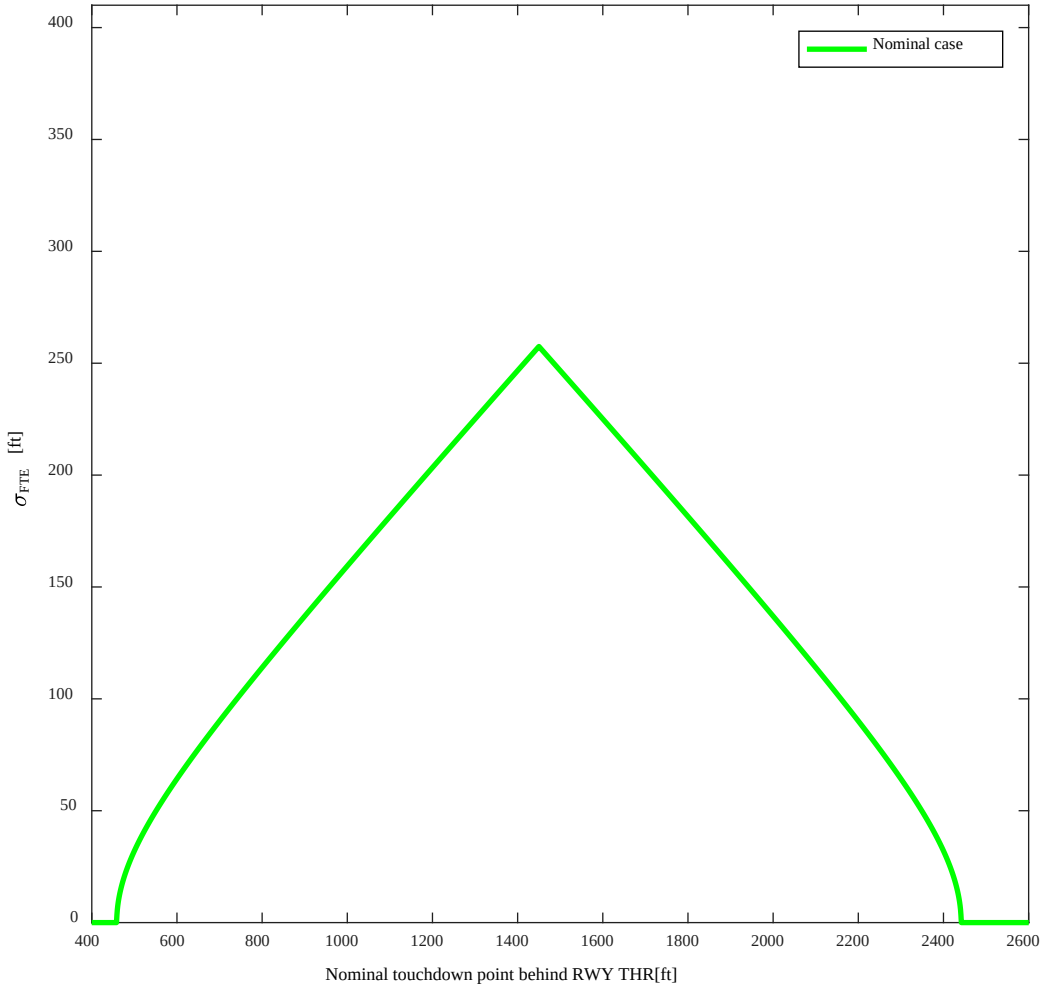

Figure 11 Constraint region for FTE under nominal NSE conditions.

3.2.2 Limit case FTE constraints

A similar condition exists for the limit case. In the limit case one parameter is kept at its most adverse value while all other influencing parameters vary according to their nominal distributions. The total probability of an unsuccessful landing is the product of the probability that a landing is unsuccessful, given a certain vertical error E_v due to the limit case condition which is not detected $P_{UL|E_v,md}(E_v)$, multiplied with the probability of that error being undetected $P_{md}(E_v)$. An unsuccessful landing would

again be considered to occur when the touchdown takes place outside of the touchdown box, i.e. less than 200 ft or more than 3000 ft behind the runway threshold for the limit case.

In a similar way as in Equations (33) and (34) for the nominal case the requirement on σ_{FTE} for the limit case can be expressed as

$$\sigma_{FTE} \leq \sqrt{\frac{NTDP - 200\,ft - \frac{E_v \cdot 3.28\,{}^{ft}\!/_{m}}{\tan(GPA)}}{k_1} - \left(\frac{VAL \cdot 3.28\,{}^{ft}\!/_{m}}{K_{ffmd} \cdot \tan(GPA)} \right)^2} \tag{35}$$

for the land short case and as

$$\sigma_{FTE} \leq \sqrt{\frac{3000\,ft - NTDP - \frac{E_v \cdot 3.28\,{}^{ft}\!/_{m}}{\tan(GPA)}}{k_1} - \left(\frac{VAL \cdot .3.28\,{}^{ft}\!/_{m}}{K_{ffmd} \cdot \tan(GPA)} \right)^2} \tag{36}$$

for the land long case. In this formulation an additional vertical error E_v is assumed as a result from a limit case condition. The k_1-factor results from the touchdown requirements which have to be fulfilled with a probability of 10^{-5} for the limit case such that

$$k_1 = Q^{-1}(p_{UL}) = Q^{-1}(10^{-5}) = 4.26\,. \tag{37}$$

The resulting constraint region for the FTE assuming a limit case NSE of 3.3 m (worst case error as described later in Section 3.3.2.2) is shown by the light blue line in Figure 12.

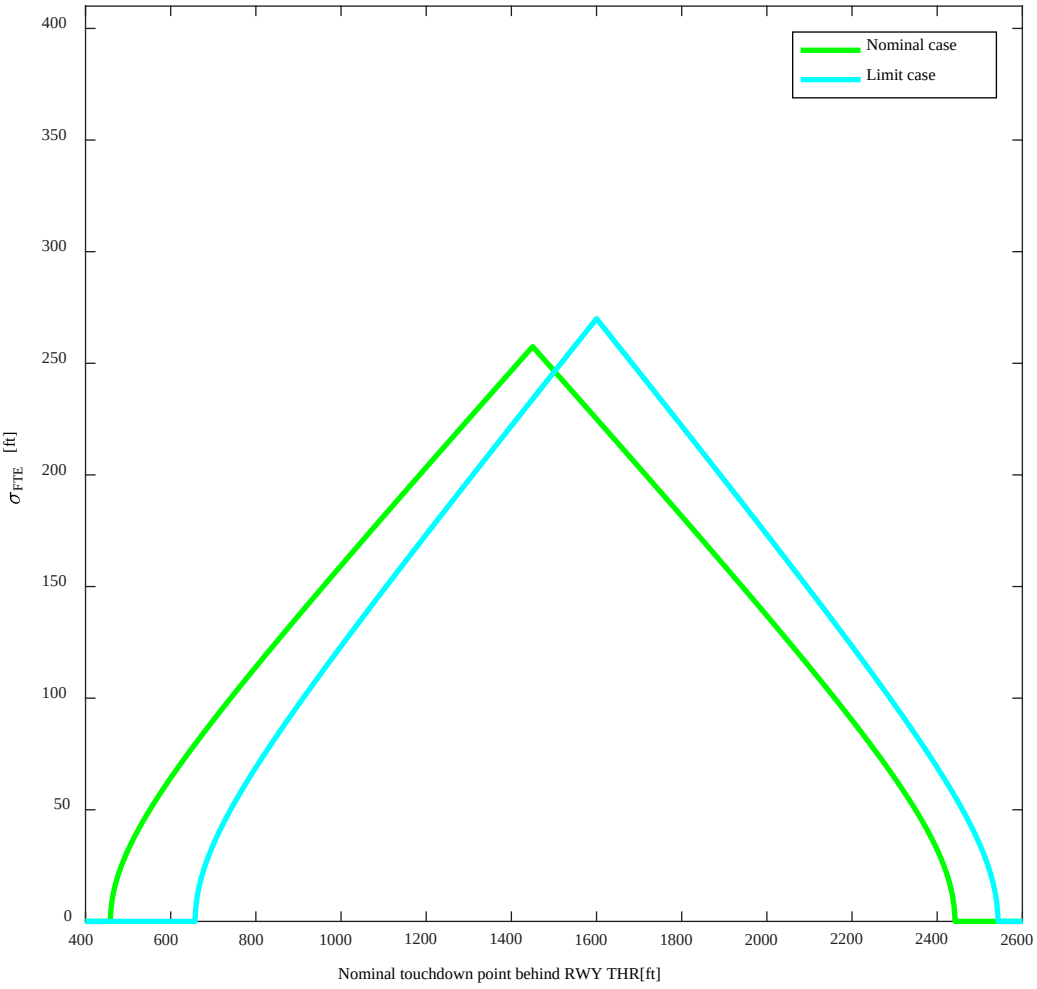

Figure 12 Constraint region for FTE under nominal and limit case NSE conditions

Note that the limit case constraint has a somewhat steeper slope and is centered slightly further behind the runway threshold. This is due to the larger land long limit (3000 ft instead of 2700 ft) compared to the nominal case.

3.2.3 Malfunction case FTE constraints

In the malfunction case, fixed values for FTE and NSE are assumed since it has to be shown that the aircraft lands inside the touchdown box with complete certainty. Taking the variables as stochastically varying, this condition could not be fulfilled. They are taken at the 95th percentile to represent a conservative nominal situation [62] and thus the k-factor for fixing the value becomes

$$k_2 = Q^{-1}\left(\left(1-0.95\right)\!\!\diagup\!\!2\right) = 1.96 \tag{38}$$

again with $Q(x) = \frac{1}{\sqrt{2\pi}} \int_{-\infty}^{x} e^{\frac{t^2}{2}} dt$. When fixing NSE and FTE at their 95th percentiles the land short condition for the FTE becomes

$$\sigma_{FTE} \leq \frac{NTDP - 200\,ft - \frac{(k_2 \cdot \sigma_{NSE} + E_v) \cdot 3.28\,{ft}/{m}}{\tan(GPA)}}{k_2} \tag{39}$$

with $\sigma_{NSE} = VAL / K_{ffmd}$, and similarly for the land long case

$$\sigma_{FTE} \leq \frac{3000\,ft - NTDP - \frac{(k_2 \cdot \sigma_{NSE} + E_v) \cdot 3.28\,{ft}/{m}}{\tan(GPA)}}{k_2} \tag{40}$$

Note that both equations depend again on the size of the VAL, as well as on the size of a vertical error E_v which results from the malfunction condition. The size of E_v depends on the performance of the ground monitors, the expected threats to the system and their magnitudes. In the GAST D SARPS a largest value for the vertical error E_v in the position domain is defined implicitly by limiting the error in the pseudorange domain and requiring airborne geometry screening. A more detailed discussion on how to fix E_v at a certain value and how large this value may be is the content of Chapter 4. A fixed boundary for E_v and VAL in Equation (40) then results in a limitation for the permissible σ_{FTE}. Following the requirements with VAL=10 m and a largest possible E_v of 6.44 m (the derivation and discussion of this value follows in Section 3.3.2.3) the malfunction case constraint is indicated by the red curve in Figure 13. It has again a steeper slope than the nominal and limit case curve and is centered at the same point as the limit case curve (land long limit is the same for limit and malfunction case). For airworthiness approval it has to be shown that a navigation system can support autoland operations for all three cases. The total constraint region is thus the lowest limit of all cases for every combination of NTDP and σ_{FTE} and is indicated by the dashed black curve in Figure 13. The land short condition for of σ_{FTE} is dominated by the malfunction case for a one sigma touchdown performance of up to 184 ft (56.1 m). For larger σ_{FTE} -values up to 246 ft (75.0 m) the limit case condition is the most constraining one. The land long condition is dominated by the constraint on the nominal behavior. For σ_{FTE} -values between 125 ft (38.1 m) and 246 ft (75.0 m) it is the limiting case, while for smaller values the malfunction limit again drives the required performance.

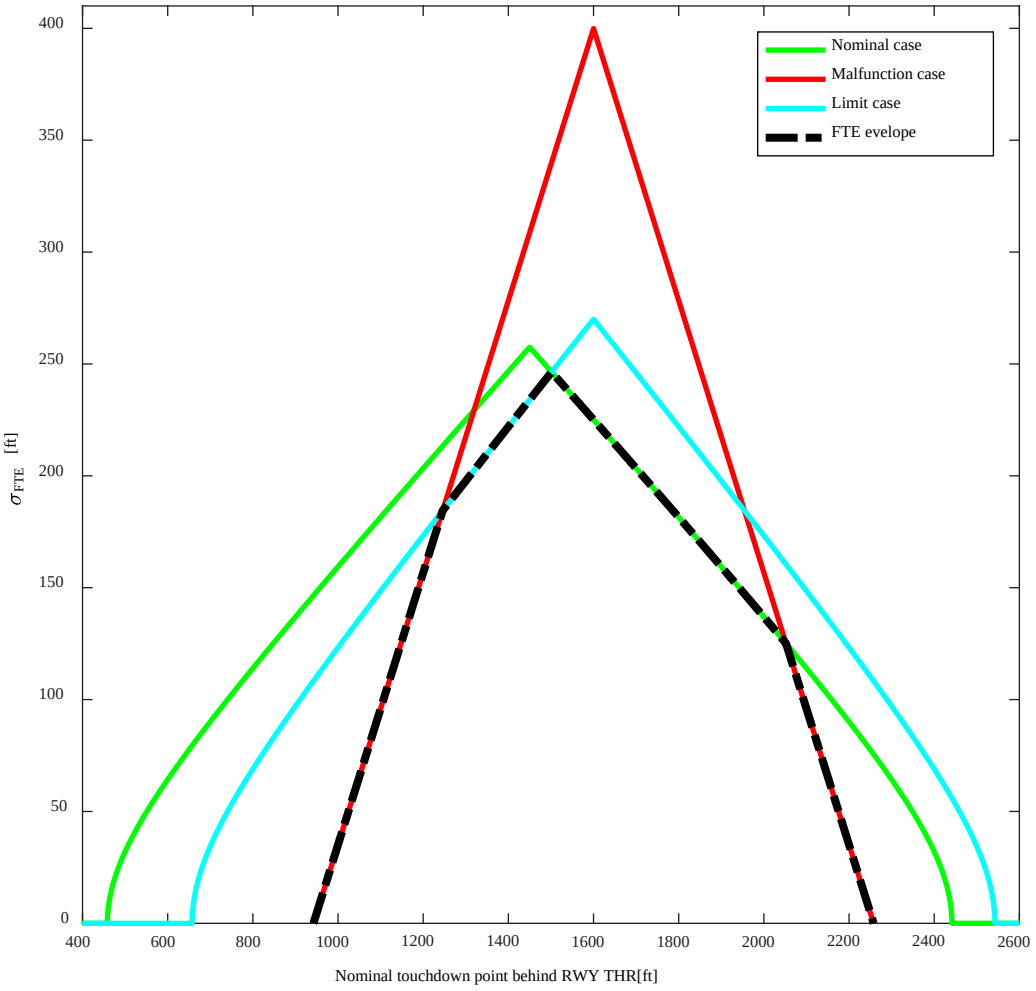

Figure 13 Constraint region for the standard deviation of FTE for nominal, limit and malfunction case NSE. The total resulting constraint region is indicated by the dashed back line.

Depending on the actual aircraft installations, aircraft dimensions and weight, autopilot laws and glide path angle and of course type of aircraft the nominal touchdown point can vary substantially. An example for the variation of NTDPs and FTE values (blue asterisks) is shown in Figure 14 which is reproduced from a Boeing report on a research program concerning several aspects of GBAS [63].

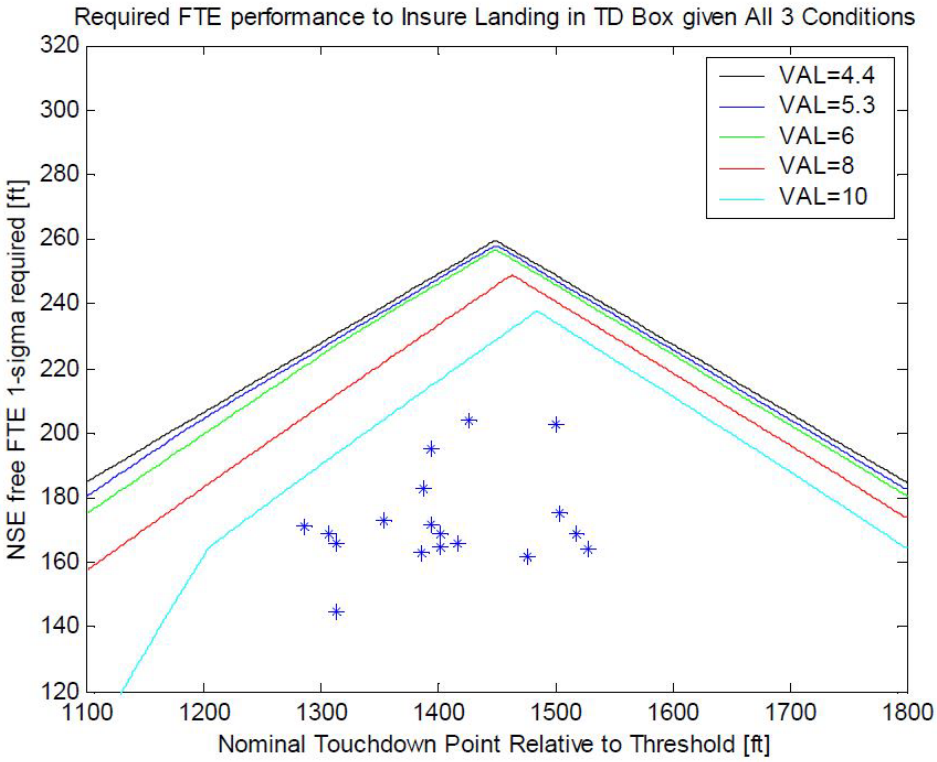

Figure 14 Touchdown performance of Boeing airplanes compared to different alert limits and constraint regions for nominal, limit and malfunction case extracted from [63].

Note that the actual size of the constraint region is somewhat different in Figure 13 and Figure 14. This results from the fact that different values have been agreed on by the international community than those used in this report on influencing factors, such as the allocated integrity risk to the Alert Limits or on the derivation of the largest errors in the limit and malfunction case. It furthermore shows the resulting constraints of NTDP/FTE performance depending on different values for the VAL. The tightest constraint on the FTE performance results from the least stringent requirement on the alert limit. For the 10 m VAL case (turquoise constraint region) the previously described joint constraint coming from the different requirements for the nominal, limit and malfunction case is clearly visible from the different slopes of the boundaries.

It can also be seen from Figure 14 that the most constraining NTDP (closest to the beginning of the touchdown area) of the aircraft considered here is about 1290 ft behind the runway threshold. This value is used in the derivation of the NSE requirements described in the next section. However, there is also a large variation of the NTDPs among the different types of aircraft. Taking only the most conservative value thus places an unnecessarily tight burden on all other aircraft.

3.3 AIRCRAFT NSE REQUIREMENTS

After the FTE, the other significant contribution to the TSE results from the imperfections of the navigation system. The navigation system error (NSE) requirements apply to the actual output of the navigation system, irrespective of the sensors which are used to develop a position solution. During different phases of flight, typically different navigation sensors are used. The baseline in the SESAR and NextGen programs in Europe and the US is centered around the assumption that navigation is based more and more on satellite signals. GBAS is designed as a landing system providing guidance on the approach and during landing and rollout. There are, however, certain cases where conventional navigation sensors are still being used. The principle of operation of ILS and its performance were already shown in Sections 2.1 and 2.3. Other relevant sensors are discussed briefly in Section 3.3.1, before the derivation of requirements for GBAS NSE is shown in more detail in Section 3.3.2.

3.3.1 Other Aircraft NAV Sensors

Apart from GBAS there are the radar altimeter and the aircraft's inertial navigation system which are used in autoland operations, even when guidance is based primarily on GBAS. Their tasks in the autoland architecture are described here for completeness, however, they will not be considered in more detail in the further evaluations of this work.

3.3.1.1 Radar Altimeter

The radar altimeter is installed at the bottom of the fuselage and measures the height of the aircraft above ground by emitting a signal and measuring the transit time of the returning signal which is reflected by the ground. This information is typically only output at altitudes below 2500 ft above ground. The main task of the radar altimeter is initiating the flare during landing. At a predefined height above ground (typically between 30 and 100 ft indicated altitude) vertical guidance is switched from GBAS or ILS to the radar altimeter. The ILS glide slope information becomes unreliable at such low heights above ground due to the location of the glide slope antenna next to the runway. Thus, the control of the flare is done autonomously on board based on the radar altimeter measurements. When changing the primary means of approach guidance from ILS to GBAS one of the main concerns for potential users are associated costs. In order to keep them as low as possible, the least amount of change to the autopilot modes and operations is desired. For that reason the radar altimeter is assumed to fulfill the same tasks as currently with ILS even though GBAS guidance does not become less reliable near the ground.

The minimum operational performance standards (MOPS) for the radar altimeter are specified in [64]. Below an indicated height above ground of 100 ft (30.48 m) the accuracy of the output must be within +-3 ft (0.91 m) and between 100 ft (30.48 m) and 500 ft (152.4 m) indicated height within +-3% of the

indicated value. Those values refer to the accuracy of the sensor, i.e. 95% of these measurements must be within this requirement. In an autoland context other contributing factors can also potentially impact the measured height above ground. The first return of a signal depends on the beam width of the radar altimeter and the evenness of the terrain overflown [65]. Furthermore, an attitude dependent lever-arm bias for the different locations of the ILS/GNSS antenna and the radar altimeter installation can introduce further uncertainties in the measurements.

3.3.1.2 Inertial Navigation System

The Inertial Navigation System (INS) is based on measuring accelerations of the aircraft in three perpendicular directions and turn rates about the corresponding axes. Based on an initial state of the aircraft (position, attitude, velocity, turn rates) the sensor information is integrated and position updates are computed. This system has very good properties for short-term navigation but due to the integration process sensor noise and all other errors are integrated and thus increase with time. Typically, the information from the INS is fused into an integrated position solution with information from other sensors, such as GNSS, VOR, DME and ILS. For GLS the INS information is used for continuity reasons and the requirements of a fail-operational landing system. At a certain stage of the approach the aircraft can and will continue an automatic landing even if the signals from the approach guidance system is lost. Boeing certifies their aircraft for a 200 ft alert height, while Airbus uses a 100 ft alert height [66]. The fusion and integration methods with INS are, however, also beyond the scope of this work and only mentioned here for reference.

3.3.2 GBAS NSE Requirements

The budget allocation tree shown previously in Figure 9 indicates that, apart from the conventional navigation sensors, an allocation is made for navigation system errors introduced by the GBAS. In the process of the requirement derivation for the GLS, no sensor fusion is considered. This assumption is conservative on one side, since the integration with other sensors has the potential to detect errors in GBAS. On the other hand all other sensors are also prone to errors with different fault modes depending on their sensors and signal processing schemes. From an airworthiness perspective, they are treated as separate faults and thus are not considered together with GLS. The error budget attributed to GBAS covers any influence from the space segment of the GNSS, the GBAS ground subsystem at the airport and the airborne installation at the aircraft. As for the FTE considerations in Section 3.2 similar performance requirements in the nominal, limit and malfunction case are derived for the GBAS NSE and thus all monitoring algorithms within the system. These are discussed in the following sections. As the necessary performance results are again derived from the definition of a successful landing as described in Section 3.1, a trade-off between NSE and FTE performance is required. In order to derive specific low-level NSE limitations the derivation process is largely based on a fixed FTE performance

assumption. This approach is useful for the derivation of requirements for the GBAS ground station since sufficient protection has to be provided for all aircraft.

3.3.2.1 Nominal case NSE requirements

The nominal case for GBAS is rather simple and straight forward. If all influencing parameters vary according to their expected distributions the protection level concept conservatively models all error sources and can bound the resulting position error with a sufficiently high probability. The protection levels are based on modelling the residual uncertainty resulting from the ground system, the airborne installation and ionospheric and tropospheric effects. The root-sum square of these contributors for each satellite represents the total uncertainty associated with an individual pseudorange measurement. These uncertainties are then projected into the position domain and inflated to bound errors with a sufficiently low residual integrity risk. This process was previously described in Section 2.2.3.3. The touchdown performance for the nominal condition has to satisfy the conditions

$$NTDP - k \cdot \sigma_{TSE} \geq 200\,ft \tag{41}$$

and

$$NTDP + k \cdot \sigma_{TSE} \leq 2700\,ft \tag{42}$$

again with $NTDP$ being the nominal touchdown point, k the multiplier associated with the allocated integrity risk and $\sigma_{TSE} = \sqrt{\sigma_{NSE}^2 + \sigma_{FTE}^2}$ the standard deviation of the touchdown dispersion which consists of an FTE (mean at NTDP, and standard deviation σ_{FTE}) and an NSE (zero mean, standard deviation σ_{NSE}) contribution. For the nominal case the probability of landing outside of the box must be smaller than 10^{-6} which results in

$$k = Q^{-1}(10^{-6}) = 4.75 \tag{43}$$

with the inverse Q-function as previously described in the FTE discussion. The largest nominal vertical NSE standard deviation $\sigma_{NSE,v}$ is given by the VPL which is limited to a maximum of 10 m. Thus it is limited to $\sigma_{NSE,v} \leq 10m / K_{ffmd} = 1.72m$. The along-track dispersion σ_{FTE} of the touchdown point due to a certain vertical NSE performance is then given by a projection according to the glide path angle GPA as

$$\sigma_{NSE} = \frac{\sigma_{NSE,v}}{\tan(GPA)} \tag{44}$$

Assuming a worst FTE performance of $\sigma_{FTE} = 180\,ft$ and a minimum glide path angle $GPA = 2.5°$, the most conservative value for the NSE is $\sigma_{NSE} = 129.3\,ft$ and thus the worst TSE is given by $\sigma_{TSE} = 221.6\,ft$. Assuming a touchdown point of 1290 ft behind the runway threshold with the worst σ_{NSE} and $k = 4.75$ the conditions (41) and (42) are still fulfilled. The protection level concept which bounds the nominal case error is thus sufficient to ensure that the touchdown requirements are met in that case.

3.3.2.2 Limit case NSE requirements

The limit case considerations assume that one influencing parameter is kept at its most adverse value while the others vary in a nominal way. This requirement interpreted in a GBAS context defines a general monitoring necessity with a threshold set low enough to enable a safe landing when one cause (e.g. an ionospheric condition) creates a certain error. It is essential that each of the monitors in GBAS has to satisfy this condition. Following the notation of [13], the fact that the aircraft may not land outside of the landing box with a probability higher than 10^{-5} in a limit case condition can be described as

$$P_{UL|\,fault}(E_v) = P_{md}(E_v) \cdot P_{UL|\,fault\_undetected}(E_v) \le 10^{-5} \tag{45}$$

where $P_{UL|\,fault}$ is the probability of an unsuccessful landing (i.e. touching down outside the box) given a limit case error, P_{md} is the probability of missed detection of a generic monitor, $P_{UL|\,fault\_undetected}$ is the probability of an unsuccessful landing given a limit case fault occurs and is not detected and E_v is a vertical position error, resulting from the limit case error. The probability of landing outside the box (for the land short case) given and undetected fault that results in a vertical error E_v is represented by the blue curve inFigure 15 and can be described (for the land short case) by

$$P_{UL|\,fault\_undetected}(E_v) = P\left(NTDP - k \cdot \sigma_{TSE\_ff} - \frac{E_v}{\tan(GPA)} \le 200\,ft \right) \tag{46}$$

The two factors of Equation (45) have complementary characteristics. This situation is illustrated in Figure 15. While the probability that a monitor does not detect a certain error E_V (first factor) decreases with increasing values of E_V (red curve), the probability of landing outside the touchdown box (second factor) increases with increasing E_V (blue curve). Vertical errors smaller than 3.3 m are not critical since the probability of landing outside of the box remains below 10^{-5}. However, with increasing size of the vertical error a monitor has to detect with increasing probability (or decreasing probability of missed detection as shown in the figure). The product of the values of the blue and the red curve has to be smaller or equal to 10^{-5} in order to fulfill the limit case requirement.

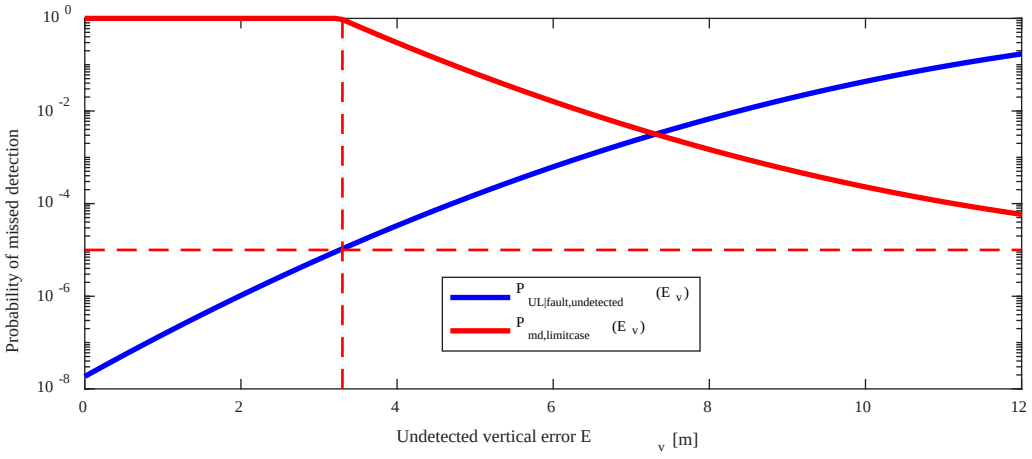

Figure 15 Limit case requirement for the probability of missed detection for a generic GBAS monitor.

The condition for a limit case error as shown in Figure 15 is a limit on the position error. For the GBAS it is, however, useful to define conditions in the pseudorange domain. As it was described in chapter 2.2.3.1, the relation between the pseudorange domain and the position domain is given by the weighted pseudoinverse of the geometry matrix, $\mathbf{S}$. Any error on a single satellite cannot lead to a larger position error than the corresponding factor for the specific satellite in the $\mathbf{S}$-matrix. Limiting the size of the largest projection factors $s_{vert,max}$ and $s_{lat,max}$ into the vertical and the lateral position domain thus limits the largest limit case errors. Assuming a limit for the projection factor $s_{vert,max}$ and a largest vertical position error $E_{v,max}$ for which the aircraft still lands in the box thus defines a limit on the largest pseudorange error $E_{r,max}$ of a single satellite which is given as

$$E_{r,max} = \frac{E_{v,max}}{s_{vert,max}} \tag{47}$$

The largest vertical position error results from the touchdown requirement and an assumption about the FTE performance. The same equations as for the FTE requirements in Section 3.2.2 apply ($NTDP = 1290\,ft$, $GPA = 2.5°$) and can now be solved for $E_{v,max}$. Together with Equation (47) it can then be solved for $E_{r,max}$ to obtain the desired limit on an individual pseudorange error. The red curve shown in Figure 15 was plotted based on the assumptions of $\sigma_{FTE} = 150\,ft$ and $s_{vert.max} = 4$. The way the requirements are written also accommodates larger values for σ_{FTE} when the projection factor $s_{vert.max}$ is limited accordingly. A combination $s_{vert.max} = 2$ and $\sigma_{FTE} = 180\,ft$ would for example still fulfill the monitoring condition. In such a case it is the responsibility of the airframe manufacturer to set the geometry screening parameters (i.e. the limit on $s_{vert.max}$) low enough to ensure that the limit case requirement holds.

For an easier parameterization of the monitoring condition resulting from the limit case considerations, a slightly more constraining piecewise linear approximation of the resulting missed detection requirements was defined (given in Table B-76 A of [4]). It is shown in black in Figure 16 together with the required monitoring performance (shown in red) as resulting from the touchdown requirements.

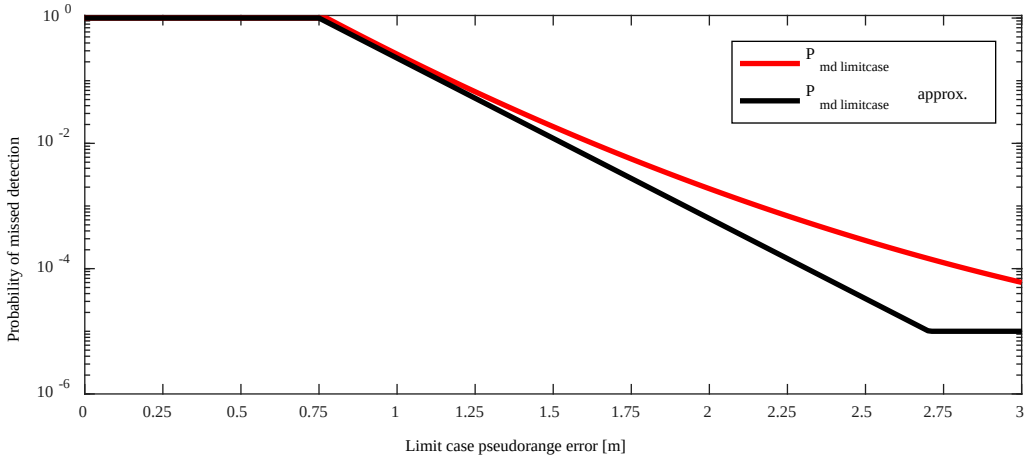

Figure 16 Limit case requirement (red) and approximation as standardized (black).

3.3.2.3 Fault case requirements

Finally, also for the NSE a malfunction condition exists. In that case it has to be shown again that the aircraft can land in the box with complete certainty in case of a single undetected malfunction which occurs with a probability greater than 10^{-9}. The probability of the occurrence of an undetected fault condition is the product of the probabilities that some conditions exists which produces the fault condition and that this condition is not detected by the GBAS. In the requirement derivation process the FTE and NSE performance are again assumed to be fixed at their 95th percentiles because if they were considered as varying parameters with a Gaussian distribution, this condition could never be fulfilled. Additionally a vertical error is assumed as result from the fault condition. This can be formulated for the land short case as

$$200\,ft \le NTDP - k_2 \cdot \sqrt{\left(\frac{\sigma_{NSE,vert}}{\tan(GPA)}\right)^2 + \sigma_{FTE}^2} - \frac{E_v}{\tan(GPA)} \tag{48}$$

and similarly for the land long case as

$$NTDP + k_2 \cdot \sqrt{\left(\frac{\sigma_{NSE,vert}}{\tan(GPA)}\right)^2 + \sigma_{FTE}^2} + \frac{E_v}{\tan(GPA)} \le 3000\,ft \tag{49}$$

again with $NTDP$ the nominal touchdown point, $k_2 = Q^{-1}\left((1-0.95)/2\right) = 1.96$ corresponding to the k-factor for the 95th percentile of the Gaussian distribution $\sigma_{NSE,vert}$ the standard deviation of the nominal vertical NSE distribution, σ_{FTE} the along-track touchdown dispersion due to the flight technical error, GPA the glide path angle of the approach and E_v a vertical error which results from the fault case condition.

Equations (48) and (49) can now be solved for E_v when fixing all other parameters. From Equation (47) it is then possible to derive a fault case monitoring requirement. When taking the assumptions as

before ($NTDP = 1290\,ft$, $GPA = 2.5°$, $\sigma_{NSE,vert} = VAL / K_{ffmd} = 1.72m$, $s_{vert,max} = 4$) but with an increased $\sigma_{FTE} = 180\,ft$ (as compared to $\sigma_{FTE} = 150\,ft$ which was used in the limit case) the pseudorange monitoring condition becomes

$$E_{r,i,max} = \frac{E_v}{s_{vert,max}} = \frac{6.4\text{m}}{4} = 1.6\text{m} \tag{50}$$

No justification is given why different FTE performances are assumed in the different cases. Note that so far no credit is taken for any prior probability of the occurrence of a fault. In [13] a value of $P_{fault} = 7.5 \cdot 10^{-6}$ is given for a prior probability of fault. It results from a satellite fault rate for the GPS satellites of 10^{-4} per hour, an exposure time of 15 seconds (time from the CAT-I minimum to touchdown) and a maximum number of visible satellites of 18. The requirement to monitor for pseudorange errors larger than 1.6 m appears in the draft SARP in Section 3.6.7.3.3.3 [3].The resulting fault case monitoring condition assuming a prior fault probability of $P_{fault} = 7.5 \cdot 10^{-6}$ is shown in red in Figure 17.

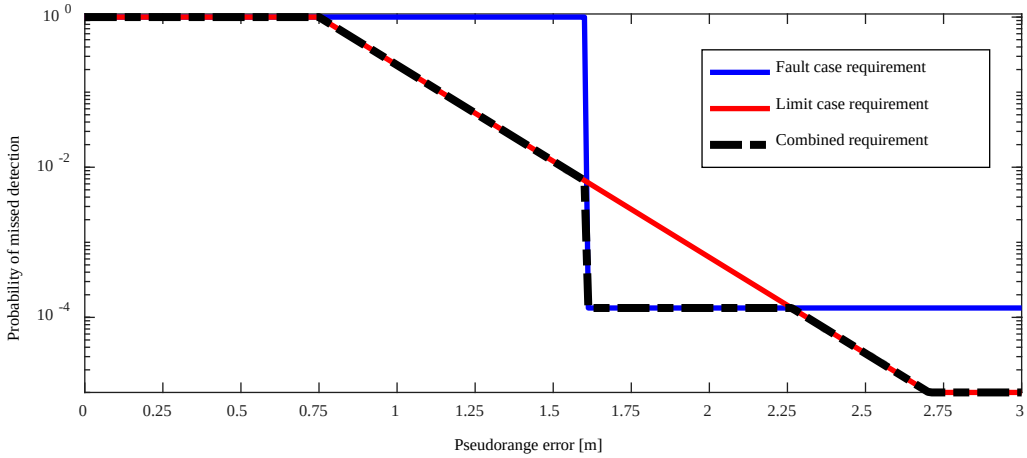

Figure 17 Monitoring requirement in the pseudorange domain for the fault case (red) together with the approximated limit case requirement from the previous section (blue) and the combined requirement indicated by the dashed black line.

The black dashed curve shows the overall monitoring requirement combining the limit and fault case requirements. For smaller errors the limit case is the more constraining case, but as the pseudorange errors exceed 1.6 m the fault case becomes the more constraining monitoring condition until the limit case requirement again dominates for errors larger than 2.25 m.

3.4 DISCUSSION OF REQUIREMENTS AND POSSIBLE RELAXATIONS

The previous sections gave a summary of the derivation of the currently proposed requirements and the rationale on how they were derived. A number of assumptions were taken in order to be conservative and cover all possible cases. However, at certain points those assumptions are unnecessarily conservative which results in requirements which are sometimes hard to fulfill and thus reduce the availability of the GBAS service.

In this section some adjustments are proposed in the assumptions made to derive several values. These suggestions are a further contribution made in this thesis, contributing to the goal of using available knowledge in order to reduce unnecessary conservatism and improve the usability of GBAS. All proposed changes do never compromise any safety targets but result from a view on actual conditions and capabilities of the systems rather than worst case assumptions.

3.4.1 Glide Path Angle

One key assumption is that a vertical NSE on the approach translates into an along-track error at touchdown. The assumption is justified by the switch from vertical GLS guidance to guidance by the radar altimeter at a defined radar altitude. For the derivation of the requirements a 2.5° GPA was assumed. While this value is the minimum for precision approaches [17], there is no need to assume that minimum value for all approaches. The by far most commonly used GPA is the value of 3°. Of the few airports using a lower GPA, many are combined civil/military airfields which require the lower GPA for military aircraft. However, if the airspace above the approach track permits, there is no operational reason to stay with the shallow glide path. At many airports effort is put to increase the glideslope angle even above 3° to increase the height of overflight over populated areas (e.g. Frankfurt uses 3.2° for approaches in CAT-I conditions to their new runway 25R/07L).

In any case and in contrast to ILS, the GPA is transmitted in the Type 4 GBAS message and is thus a known parameter which can be used when determining limits on the maximum tolerable NSE and/or FTE for a specific approach. In all derivations shown in the previous sections the GPA plays a central role in relating a vertical error into an along-track error on the runway. This is true for all three cases previously described.

It is therefore suggested that the required monitor performance of a GBAS is derived based on the GPA which is used for the specific approach an aircraft is flying, instead of 2.5° as most conservative value. Most airports use a steeper GPA anyways and those that use a more shallow approach there is a possibility to trade required monitor performance (and thus in the end availability of the approach service) against the approach angle. An example of how monitoring can be relaxed based on the GPA is shown later in Section 5.4.2 of this thesis.

3.4.2 Relation between pseudorange and position domain

A second case where the requirements are derived based on the most conservative assumption is the relation between a ranging error and the resulting position error. As shown in Section 2.2.3.1, the measured pseudoranges are projected into the position domain by the $\mathbf{S}$-matrix which is the weighted pseudoinverse of the geometry matrix. The projection from all pseudoranges into the vertical domain is given by the previously discussed parameter s_{vert}. In order to limit the influence of a single satellite onto the overall position solution it is assumed that a maximum value is given by $s_{vert,max} = 4$. It is a sensible approach of limiting the influence since the ground has no means of knowing which subset of satellites and thus which s-values the airborne system is using.

However, with a given set of satellites for which corrections are provided, there is a certain knowledge about which combinations of satellites can be used on board of an aircraft. Since only ranging information can be used from satellites for which corrections are provided there is a limited number of subsets which can be used. In all of those subsets the value of $s_{vert} = 4$ is very rarely obtained. Typically for the worst geometries it stays in the range of 3-3.5, because otherwise the alert limit would be exceeded. From all possible subset geometries the ground can thus limit the s_{vert} to a value typically lower than 4 by evaluating all possible subset geometries. Hence, an erroneous pseudorange measurement (and also the combination of 2 or more erroneous pseudorange measurements) has a worst case impact which is usually smaller than assumed in the requirement derivation and, just as important, it is known to the ground to a certain extend by the limited number of subset geometries which can be formed.

It is therefore suggested to use the actual worst case $s_{vert,max}$ instead of assuming a fixed $s_{vert,max} = 4$ for the derivation of certain monitoring thresholds. An example of how monitoring can benefit from this approach is again shown in Section 5.4.2.

3.4.3 FTE contribution and nominal touchdown point

In Section 3.3 the derivation of requirements for the NSE contribution to the TSE was discussed. Despite the fact, that there is some freedom for the airframe manufacturers on limiting their geometry screening limits according to the FTE performance of the aircraft, it is generally assumed that the FTE is a single fixed number given as σ_{FTE}. It is derived in the process of aircraft certification and is then kept fixed. However, in reality this parameter is changing with prevailing wind conditions and aircraft weight, center of gravity location and aircraft configuration. With knowledge at least of the weight and

center of gravity location (and knowledge about the uncertainties associated with this knowledge) it may be possible to use more realistic values for σ_{FTE} as well as for the $NTDP$.

In the current GBAS architecture, the ground station is at least partially responsible for ensuring the integrity. As the ground station has to support all arriving aircraft a certain amount of conservatism and standardized assumptions are necessary. Future GBAS service types may, however, shift the responsibility for threat mitigation more to the airborne system such that e.g. an improved FTE- performance can be leveraged in the navigation system and thus improve the availability of the GBAS service. This idea is further pursued and exploited in the development of an ionospheric monitoring algorithm for future dual-frequency GBAS and is discussed in detail in Section 5.5 of this thesis.

4 FTE CONTRIBUTION - AUTOPILOT SYSTEMS FOR AUTOMATIC LANDINGS

This section starts with a short description of the autopilot systems used for automatic approaches and landings and then shows an exemplary analysis of the touchdown performance of a given autopilot implementation with a limited set of influencing parameters. The navigation requirements for the GBAS Approach Service Type D were derived based on the definition and criteria of a safe landing (as previously described in Chapter 3). These are given in terms of total system error (TSE) that is then allocated between the navigation system error (NSE) and the flight technical error (FTE). The FTE in the GBAS context is only described as the standard deviation of a normal distribution describing the dispersion of the touchdown point on the runway in along-track direction relative to a nominal touchdown point. Touchdown performance, however, depends on several influencing parameters. Assuming one single performance model for all aircraft and all flying conditions is a very crude and thus conservative way to describe the autopilot performance. It is, however, useful when deriving requirements for a GBAS ground station since the ground infrastructure has to support all different kinds of aircraft. In this section the results of autoland simulations are presented. The usual way of describing the FTE is fitting the touchdown data to a Gaussian distribution. The results can, however, not be expected to be Gaussian distributed and thus the risk of landing short or long may be underestimated.

Contribution: It is suggested to model the touchdown distribution either by a Gaussian overbound or by a Johnson distribution instead of using a Gaussian fit. This is done to ensure that the risk of missing the touchdown box is not underestimated (Section 4.4.1.2). After a discussion of the implications it is shown that it is also possible to derive NSE requirements based on this kind of modelling (Section 4.6), ensuring safety and bearing the potential to leverage any knowledge about the actual loading conditions of a certain aircraft (Section 4.5).

As it became apparent in the previous chapter about the derivation of GBAS navigation requirements, an allocation of the total system error budget (i.e. the requirement that the aircraft has to land inside the touchdown box) has to be performed between the budgets for the NSE and the FTE.

This part of the thesis focuses on the determination of the FTE performance of a given aircraft and its proper modelling. It is beyond the scope of this work to improve the autopilot with respect to the characteristics of a GBAS (e.g. by leveraging the much smoother guidance signal provided by GBAS as compared to ILS for optimizing the control laws in the autopilot during a GBAS approach) although optimizing the approach and flare laws in this respect may lead to improvements in terms of touchdown performance and enable operational benefits. In the future with an improved data link more useful data to optimize the flare (such as information about the terrain) may also be leveraged and alter the touchdown characteristics. The discussions here are, however, limited to analyzing an existing autopilot. This approach follows the philosophy of GBAS where initially, the interfaces of the GBAS avionics and the flight control system are identical to ILS requiring almost no change in the autopilot modes, display of deviations and pilot training. Potential future changes can, however, easily be adopted in the concept presented in this chapter and may be useful in the future.

4.1 Approach Phases and Autopilot Modes

In this section the relevant autopilot modes for automatic landings are briefly described. Historically, first autopilots were developed to relieve the pilot from simple tasks like maintaining a certain altitude, track or aircraft attitude which would require constant attention. Further developments enabled the aircraft to automatically acquire a certain altitude or heading. As aircraft became more sophisticated and aircraft designs started to develop to constantly improve performance of aircraft also the autopilots gained importance in stabilizing aircraft designs e.g. by implementing yaw dampers in order to reduce the Dutch roll tendency, one of the Eigen motions of the aircraft. Modern autopilot and flight management systems accomplish an enormous variety from autonomously flying complete missions to interpreting pilot control inputs and providing optimized aircraft handling qualities and flight envelope protections. One of the most challenging tasks for the autopilot is the automatic approach and landing. A series of different autopilot modes are used during the different stages of an approach:

First, the ILS or GBAS approach trajectory has to be intercepted typically at an angle of about 30° laterally (segment “A” of the approach track in Figure 18) and from a constant altitude from below the glide path (segment “B”). The autopilot is armed for the localizer and glideslope mode which automatically acquires the final approach course and sink rate required to follow the final approach path. Next, the approach trajectory is tracked laterally and vertically (“C”) down to an altitude of about 45 m above ground where the ILS glide slope signal becomes unreliable. The approach mode is accomplish-

ing the path tracking and minimized deviations from that path that occur due to external influences (mainly wind). In the case of an ILS approach, an intermediate segment (“D”) follows which guides the aircraft with a constant sink rate down to the flare height, which is typically around 15 m above ground. In that segment no ILS glide slope information is used, however GBAS guidance could be continuously used in the same way as during the approach since the signals do not become less reliable with the aircraft approaching the ground. The next segment is the landing flare (“E”) where the sink rate is reduced to an acceptable value until touchdown, the pitch and roll attitude angles of the aircraft are adjusted to ensure a safe landing and the aircraft is aligned with the runway. After touchdown the rollout guidance (“F”) has to keep the aircraft centered on the runway until the autopilot is disengaged or the aircraft comes to a stop or some sort of taxi guidance is provided. While the aircraft is flying, the airspeed has to be controlled precisely in addition to the tracking of the desired trajectory. As the control of the speed and the vertical profile are closely coupled, typically this task is accomplished by managing the total energy (i.e. potential and kinetic energy) of the aircraft.

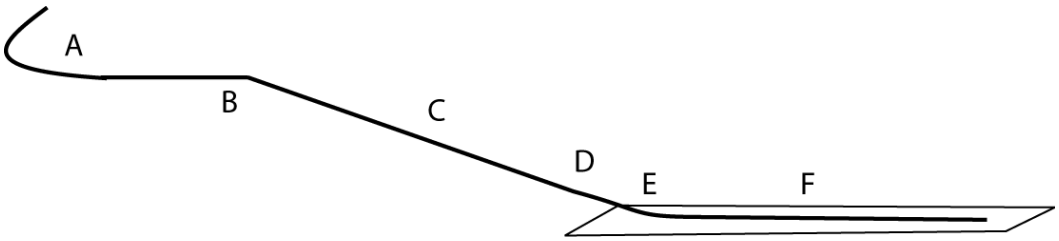

Figure 18 Phases of different autopilot modes. A: capture of lateral track, B: capture of glide path, C: tracking of approach trajectory, D: intermediate segment with constant sink rate without external guidance (ILS only), E: lading flare and decrab, F: rollout

In the context of this work the phases C to E are of special interest and the autopilot modes used to fly these portions of the approach are described in a little more detail. For the other phases there is little to no difference to existing standard approaches and automatic landings in the context of total system performance at touchdown.

4.2 CONTROLLER ARCHITECTURE

This section gives an overview over the classical autoland system used in the Airbus A320 and also in the simulation model used later in this chapter. The classical control architecture comprises several hierarchical levels as shown in Figure 19.

A typical realization (which includes the autopilot used in this work) contains a guidance mode on the outermost level. It is providing information about the position of the aircraft relative to the approach trajectory, both, laterally and vertically. For precision approaches this information is based on deviations from the ILS (see Section 2.1), MLS or GBAS (see Section 2.2.2.4). Note that these deviations

contain the NSE of the approach guidance system used, as the deviations are determined based on the difference of the estimated position relative to the approach track. The ILS/MLS/GLS avionics are usually avionics purchased by the airframe manufacturers and are providing only angular deviations to the autopilot system. However, in the case of GBAS not only angular but also rectilinear deviations (i.e. the absolute lateral and vertical displacement from the approach track in meters) are calculated within the GBAS board equipment. However, the output mimics the ILS deviations such that the look and feel for the pilot and the guidance signals coming from GBAS provide the same type of information as the ILS. The avionics typically do not interact in any other way with the aircraft or autopilot functions. From an integration point of view this is understandable when purchasing avionics from a supplier, however a tighter integration between autopilot and GBAS could lead to improvements in the future as will be discussed later in Section 4.5. Furthermore, depending on the weight and configuration of the aircraft and prevailing conditions a target approach speed V_{app} is calculated during the approach preparation and selected by the pilot.

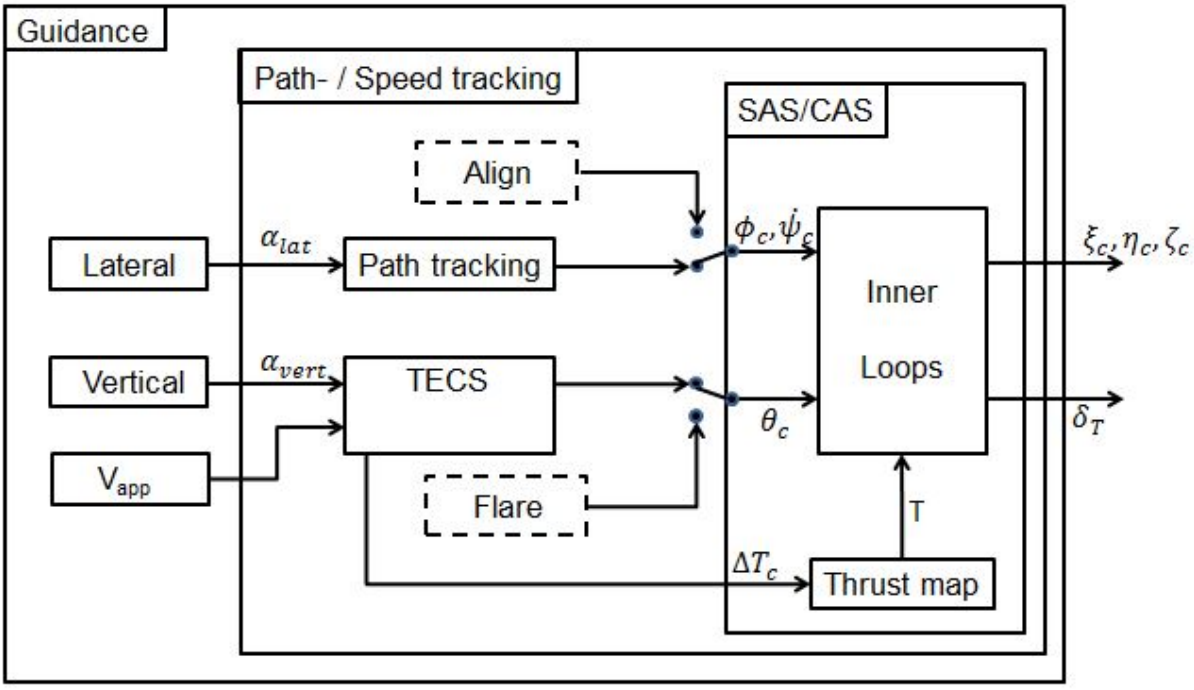

Figure 19 High-level classical autoland controller architecture

The lateral and vertical angular deviations α_{lat} and α_{vert} and target airspeed V_{app} serve as inputs to the path and speed tracking mode of the autopilot system. The path tracking is the lateral component and ensures that the aircraft stays on the lateral approach track. The upper dashed box in Figure 19 is the align function that is activated for the final phase of the approach just before touchdown. In that stage the autopilot aligns the aircraft with the runway direction in case the approach was flown with a certain side slip angle in order to correct for cross wind components. Furthermore it also ensures the aircraft touches down without a significant bank angle in order to fulfill the criteria for a safe landing as

described in Section 3.1. The vertical mode is somewhat more complex since a change in the vertical speed in order to correct for deviations has a direct effect on the airspeed of the aircraft. These two components thus have to be controlled simultaneously. This is accomplished by controlling the total energy of the aircraft (i.e. the kinetic and potential energy) jointly in a Total Energy Control System (TECS). As for the lateral mode, there is also vertical mode for the final phase of flight just before touchdown, namely the flare mode. It is activated at a predefined radar altitude (i.e. height above ground) and reduces the sink rate and adjusts the attitude of the aircraft such that a safe landing is ensured. The exact implementation of the flare law plays a major role in the achievable touchdown performance and thus is a central element for the trade-off between NSE and FTE. The outputs of the speed and path tracking modes are commanded aircraft attitude angles (ϕ_c, θ_c, ψ_c) and a commanded thrust or change of thrust ΔT_C. These values serve as inputs for the innermost autopilot modes, the stability and control augmentation systems (SAS/CAS).

In the SAS and CAS the commanded aircraft attitude angles and thrust are interpreted and the actual commands for the thrust setting δ_T and the actuation of the control surfaces of the aircraft are calculated (aileron deflection ξ_c, elevator deflection η_E and rudder deflection ζ_c) and forwarded to the actuator systems.

The performance of an autopilot depends on the exact implementation and selected parameters of all the controllers and modes and differs significantly between different aircraft types and even within different generations of the same aircraft model. It is obvious, that not all aircraft and autopilots will have the same level of performance. Furthermore, the performance depends on a number of different influences that will be discussed in the next section. In order to assess the FTE of a certain type of aircraft a statistical way of describing the performance is therefore appropriate. A number of Monte-Carlo (MC) simulations are performed to assess the autopilot performance in a wide range of possible environments and configurations. The output of these simulations in the context of GBAS guidance is a statistical description of the touchdown performance in the along-track direction of the runway. This process is described in more detail in the following section.

4.3 DETERMINATION OF AIRCRAFT'S FTE

As described in the previous sections and chapters it is essential to characterize the touchdown performance (generally described by a Gaussian distribution centered at a nominal touchdown point (NTDP) and with a corresponding along-track FTE standard deviation) of a certain aircraft type and autopilot. This information is necessary when evaluating the total performance of the aircraft (combined NSE and FTE contribution) against the lading requirements given in [9]. In the current way of

deriving GBAS NSE requirements the nominal touchdown point is assumed to be fixed and the same for all aircraft. The same is assumed for the distribution of the FTE at touchdown. As there is a large variety of parameters that influence the FTE performance during the approach and at touchdown, Monte-Carlo simulations are performed in order to determine the aircraft performance. The following list summarizes the parameters that are taken into account for the simulations. Their range and distributions is described at the example of the autoland simulations performed for the Boeing 757 and 767 during their certification program according to [11]:

Wind: Wind and turbulence conditions are simulated according to a standardized wind model (e.g. Dryden wind models **[67]**). As reference wind speeds and directions that serve as parameters of the wind simulation recorded winds at different airports are used.

Weight of the aircraft: The gross weight of the aircraft is simulated by picking a random sample from a uniform distribution between the maximum landing weight and the empty weight of the aircraft.

Moments of inertia and loading configuration: The moments depend on the weight and loading condition of the aircraft and are chosen to have either a minimum, nominal or maximum value at the randomly selected weight and loading condition.

Center of gravity: The center of gravity location is chosen from a uniform distribution between the forward and aft aerodynamic limit.

Airspeed: The initial airspeed is chosen from a uniform distribution with a lower limit of $1.3 \cdot V_s$ and an upper limit of $1.3 \cdot V_s + 10$ kts where V_s is the stall speed of the aircraft.

ILS parameters: A variety of ILS parameters, such as the glide path angle, the ILS reference datum, localizer and glideslope alignment errors, beam noise etc. are simulated for the MC-simulations.

Note that the ILS parameters are modelling the NSE of the aircraft, while the FTE is given by the autopilot performance in the given conditions. When performed as described in [11], the autoland simulations can thus be directly evaluated against the touchdown requirements relating to the TSE. When deriving NSE requirements based on these simulations the resulting values are somewhat conservative as the TSE is simulated and not just the FTE contribution.

Intercept angle: The intercept angle is the angle between initial aircraft heading and the runway direction. It is chosen as random variable with a mean of 0° and a standard deviation of 30° and is limited to a maximum of 90°.

Radar altitude error: The error of the radar altimeter is chosen from a Normal distribution that is not further specified in **[11]**. In the minimum operational performance requirements for radar altimeters (DO-155) the radar altimeter error is specified to remain below +-3 ft for 95% of the measurements below a height of 100 ft above ground (this is the area where the radar altimeter is used to trigger and guide the landing flare).

Capture distance: The capture distance is chosen from a uniform distribution with a minimum of 5 NM and a maximum of 10 NM from the runway threshold.

Altitude of the airport and slope of the runway: These two parameters are selected by picking a random sample from the database of actual airports with CAT II and CAT III runways. The slope (with the exemption of one single airport) varies between +0.8% and -0.8%.

Other parameters, such as runway length and runway friction, are not directly impacting the dispersion of the touchdown points on the runway for automatic landings but are used for determining the rollout and braking behavior.

By varying these parameters a distribution of the touchdown performance for a certain autopilot and aircraft can be derived. In order to establish confidence in the results to the required level as specified by [9], a large number of simulation runs has to be performed. The required number depends on the desired confidence into the derived results. In the following section the influence of the most significant parameters is investigated in more detail.

4.4 EXEMPLARY FTE ANALYSIS

In this section the influence of wind, turbulence and the aircraft's weight and balance on the touchdown performance are investigated and discussed. This section should exemplify part of the FTE analysis that needs to be performed and discusses how to model the results. It is, however, beyond the scope of this work to perform a full characterization of an autoland system and all influencing effects such as runway shape, terrain and radar altimeter. As basis for the results an experimental autopilot for the Airbus A320 developed at the German Aerospace Center implemented as a Simulink simulation model was used. While it does not completely fulfill the autoland criteria (as shown later), it is useful to evaluate and discuss the effect of the variation of different parameters in the simulation and discuss the methodology of FTE modelling. For the autoland simulations a set of standard parameters are used. They are summarized in Table 4-1. Any variations from these standard vales are indicated by putting the corresponding values in *italics*. The standard mass of the aircraft is chosen at the maximum landing weight (MLW) that is 64.5 t. The location of the center of gravity (CG) is given in percent of the mean aerodynamic chord, i.e. the percentage of the reference length (i.e. the distance between the most forward and most aft position of the CG) behind a given reference point. For the A320 this reference point is located 16.31 m behind the tip of the nose and the reference length is 4.19 m. The initial speed (V_{TAS}) indicates the true airspeed of the aircraft at the beginning of the simulation. The initial altitude indicates the height above the runway threshold at the beginning of the simulation. Wind di-

rection and wind speed are the reference winds used as inputs for the simulation blocks of the Dryden wind models in Simulink simulating the steady wind, wind shear and turbulence components.

Aircraft mass	Aircraft CG	V_{TAS}	Initial altitude	Wind direction	Wind speed	Turbulence intensity
64.5 t	22.2%	70 m/s	609.6 m (2000 ft)	265°	0 m/s	10^{-1}

Table 4-1 Standard parameter set for autoland simulations

All simulations are all taking place in Braunschweig in Northern Germany with a position of the runway threshold at 52.32°N and 10.56°E and at an elevation of 131.7 m above the WGS84 ellipsoid. The glide path angle (GPA) is chosen to be a standard angle of 3°. The aircraft is fully configured for landing with the landing gear lowered and flaps set to position full. Figure 20 shows the high level architecture and the main components of the simulation model. It furthermore shows a general flow diagram of the data that is exchanged between the blocks of the autoland simulation model.

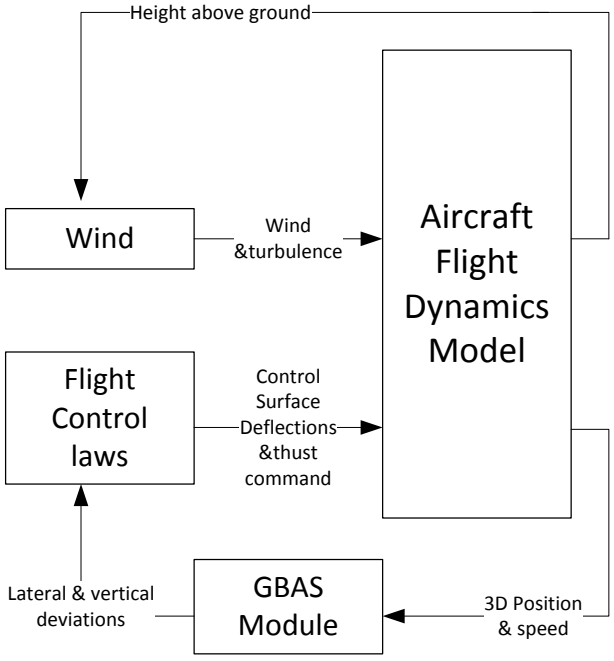

Figure 20 Data flow diagram and main components of simulation model

The core is the aircraft flight dynamics model shown on the right. Its output is the state vector of the aircraft out of which the three dimensional position is used further. In the upper loop the height above ground is used to generate the wind according to the Dryden model and feeding it back into the flight dynamics module. In the lower loop the GBAS module calculates vertical and lateral deviations from a reference trajectory and outputs these to the flight control law module. A standard ILS-lookalike tra-

jectory was used for the simulations. The functionality of the GBAS module is described in detail in Section 2.2.2.4. The deviations are interpreted in the flight control law module and the appropriate control surface deflections and thrust commands are fed back into the flight dynamics model. This represents the outer guidance loop of the controller architecture that was described in the previous section and illustrated in Figure 19.

4.4.1 Wind influence

Wind is a highly complex atmospheric phenomenon which is influenced by large scale phenomena, such as trade winds or low and high pressure areas, by local orographic conditions such as dominant wind directions due to mountains in the vicinity of an airport, but also by the surface features with different absorbing capabilities for the heat radiation of the sun. It is thus almost impossible to completely describe prevailing wind conditions. However, in order to simulate representative wind conditions several standardized wind models were defined and are commonly used for simulation purposes. Concerning the autoland simulation case that is of interest in the context of this work, two alternative wind models are described in Book 2 of the CS-AWO [9]. Another model is described in the military handbook “Flying Qualities of Piloted Airplanes” [67]. For this study the definitions from the military specification was chosen as is also used as reference for the simulation blocks in the Aerospace Blockset in Simulink used for this study.

While slightly different in their representations, all those models contain three parts for the description of the wind: a mean wind component, a windshear component and a turbulence component.

The mean wind represents the steady state wind conditions which are measured at the airport, typically at a height of 6 m above the ground. This value is also reported to the pilots during landing as a vector containing the speed of the wind and direction rounded to the nearest 10°.

The windshear is modeled to represent the boundary layer effect, i.e. a decrease in the wind as the height above ground decreases. A change in the direction of the wind is not included in the simulation as the effect would mostly affect the cross-track touchdown errors but not so much the along-track errors at touchdown that are of special interest in this study. Note that the models only include nominal windshear effects. Severe windshear effects, as be observed in the vicinity or within convective storms (e.g. thunderstorms), are not considered. Most large commercial transport aircraft are equipped with a predictive windshear warning system. In addition, many of the large airports prone to frequent windshear are equipped with ground based windshear alerting systems. Through those measures, most encounters of aircraft with those non-nominal windshear effects can be avoided and thus need not be considered in autoland simulations.

The turbulence component describes a random variation of wind speed and direction. In the Dryden Wind Turbulence Model the turbulence is simulated by defining the spectral representations of white

noise passed through an appropriate forming filter. The longitudinal, lateral and vertical spectra are given as functions of the turbulence intensities, turbulence scale lengths and the airspeed of the aircraft flying through a frozen turbulence field with a given spatial frequency.

4.4.1.1 Wind direction and wind speed

In a first step the influence of the steady wind direction and wind speed shall be discussed without considering influence of turbulence. The standard parameters for the simulation were chosen and the wind direction varied between 5° and 355° in steps of 10°. This process was repeated for a steady wind speed of 1 m/s, 5 m/s and 10 m/s. All simulation parameters are again summarized in Table 4-2.

Aircraft mass	Aircraft CG	V_{TAS}	Initial altitude	Wind direction	Wind speed	Turbulence intensity
64.5 t	22.2%	70 m/s	609.6 m (2000 ft)	*5°-355°*	*1 m/s* *5 m/s* *10 m/s*	*off*

Table 4-2 Parameter set to evaluate impact of steady state wind direction and wind speed

The following Figure 21 shows the touchdown points on the runway for different wind scenarios. The edges of the runway are shown in black, the touchdown box described in Section 3.1 is shown in red, the touchdown points are shown as black crosses for a steady wind at a reference height of 6 m above ground of 10 m/s, as magenta boxes for 5 m/s and cyan asterisks for 1 m/s. All scenarios use the Continuous Dryden Wind Turbulence Model and the Wind Shear Model to simulate the boundary layer effect. Additionally, the red diamond shows the touchdown point for the ideal case without any wind.

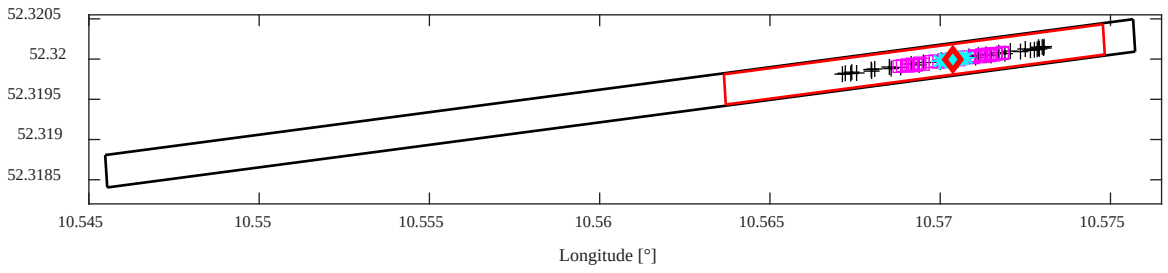

Figure 21 Touchdown points on runway for wind from 5° to 355° in steps of 10°. Black crosses show a steady wind of 10/s, magenta boxes 5m/s and cyan asterisks 1m/s. The red diamond shows the no wind scenario.

It can be seen that in this case all touchdown points are located well within the touchdown box and thus all landings can be classified as successful. However, it is also apparent that there is a large spread of the touchdown points that increases with increasing steady wind speed. A more detailed view on the touchdown points is shown in Figure 22 and Figure 23.

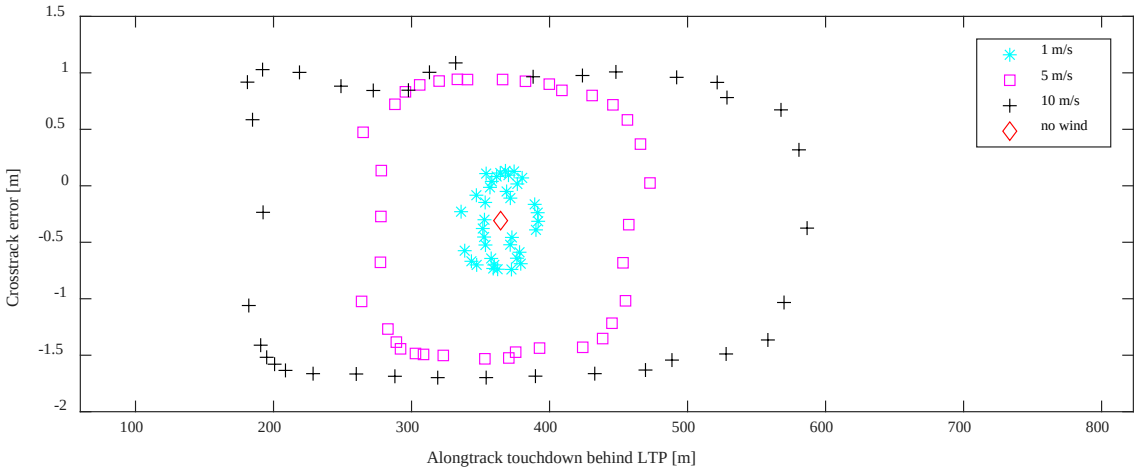

Figure 22 Dispersion of the touchdown points on the runway with steady wind of 10 m/s, 5 m/s and 1 m/s from directions between 5° and 355° in steps of 10°. The limits of the x-axis correspond to the limits of the touchdown box.

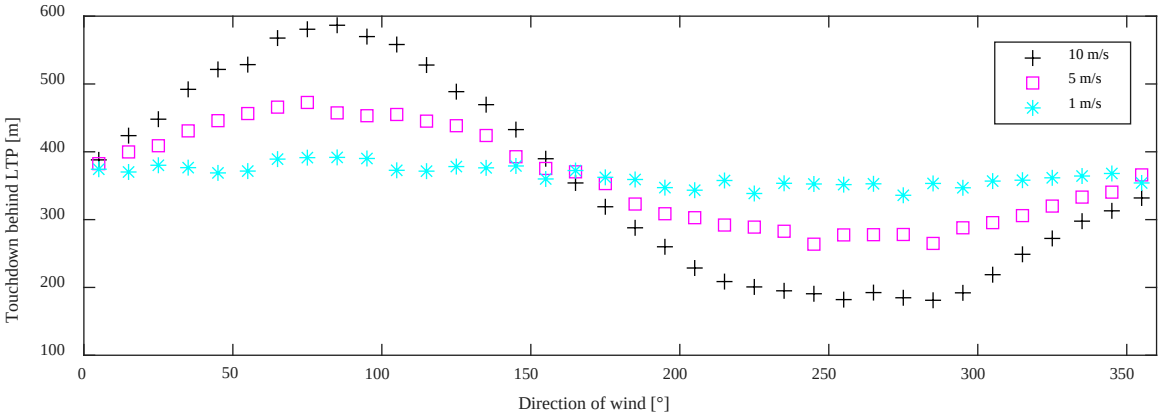

Figure 23 Touchdown point as function of the direction of the steady wind of 10 m/s, 5 m/s and 1 m/s for a runway heading of 265°

For the scenario with a steady wind of 10 m/s the touchdown points vary between 181 m for a pure headwind and 586 m behind the LTP for a pure tailwind. It should be mentioned, however, that the case of a 10 m/s tailwind component is usually out of the autopilot specifications. In those cases the opposite runway direction would be used in order to land into the wind wherever possible. The distribution of the touchdown points is not symmetric in the longitudinal direction around the nominal touchdown point but skewed towards the land-long side. The distance between the earliest and latest touchdown also decreases with the steady wind speed from a distance of about 210 m for a 5 m/s to about 56 m for the 1 m/s wind case. Even though this value considers also tailwind landings, a tailwind component of up to 1 m/s is very realistic and should be considered in a nominal scenario.

The cross-track errors remain between about 1 m on one side and 1.8 m on the other side of the runway center line. The asymmetry results from the fact that all approaches simulated here were inter-

cepting the extended runway centerline from the same side. Due to the design of the autopilot small deviations are not corrected in order to avoid oscillations caused by frequent changes of the sign of the residual lateral deviation. Thus a small steady state error remains in the simulated landings leading to the observable asymmetry of the touchdown points with respect to the runway centerline.

In summary, the steady wind component has a large influence on where the autopilot will put the aircraft onto the runway. From only these steady wind results, the approach to make an allocation between the NSE and FTE on an aircraft based on a nominal touchdown point, already shows significant deficits as the nominal touchdown point is greatly affected by the winds. Apart from the steady wind component, also turbulence of different intensities has a significant effect onto the touchdown behavior. The effect is investigated more in detail in the next section.

4.4.1.2 Turbulence intensity

After just investigating the influence of the steady wind on the touchdown performance, the results in this section show the influence of turbulence in addition to the steady wind. To illustrate the effect, the same parameter set is chosen as before, now adding turbulence to the wind (see Table 4-3). The first set of simulations assumes wind speeds of 1 m/s, 2.5 m/s and 5 m/s with the turbulence intensity set to "low", i.e. a probability of exceedance of the high altitude intensity of 10^{-2} in the Dryden Wind Turbulence Model block in Simulink. For each of the three steady wind speeds 500 simulation runs were performed.

Aircraft mass	Aircraft CG	V_{TAS}	Initial altitude	Wind direction	Wind speed	Turbulence intensity
64.5 t	22.2%	70 m/s	609.6 m (2000 ft)	265°	*1 m/s* *2.5 m/s* *5 m/s*	*light (10^{-2})* *light (10^{-2})* *light (10^{-2})*

Table 4-3 Parameter set used in autoland simulations to evaluate impact of turbulence.

The autopilot model used for the simulations was designed for a limited range of winds. Depending on the turbulence intensity, wind speeds above about 10 kts (=5.14 m/s) would cause landings outside of the touchdown zone. When also considering different turbulence intensities a number of unsuccessful landings can be observed for a steady wind component of 5 m/s. Thus, wind speeds larger than 5 m/s were not considered in this simulation. Figure 24 shows the results for 500 simulated landings with light turbulence.

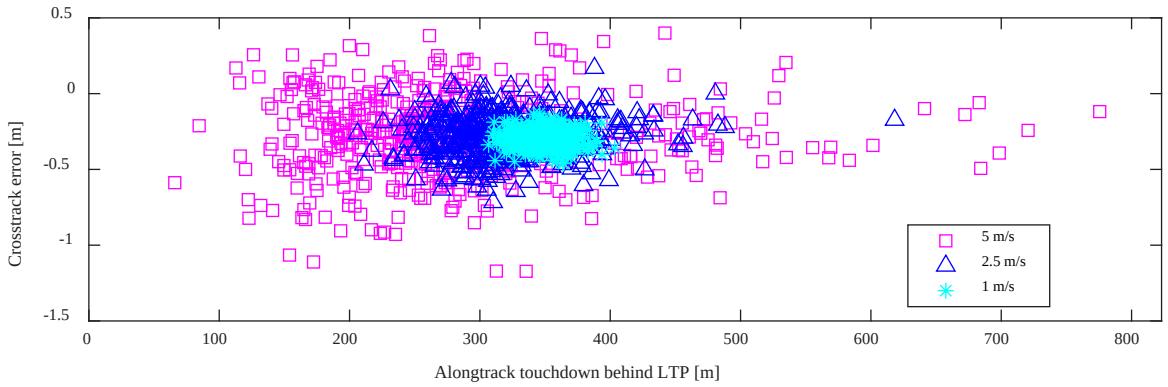

Figure 24 Touchdown points for 500 landings with light turbulence and steady wind of 5 m/s, 2.5 m/s and 1 m/s

The results for the same set of simulations using moderate and severe turbulence settings in the simulation model yielded similar results in terms of mean and dispersion of the points. While for the 1 m/s and 2.5 m/s cases there is almost no change coming from the different turbulence settings, a slight and steady increase in the dispersion is visible for the 5 m/s case for turbulence intensities of 10^{-2} (light), 10^{-3} (moderate) to 10^{-5} (severe). This increase in the dispersion of the points with increasing steady wind speed is expected, since the magnitudes of the wind changes in the turbulence is defined relative to the steady reference wind. For 1 m/s and 2.5 m/s all touchdowns were successful. For the 5 m/s case 7 out of 500 landings occurred beyond the touchdown zone and 2 even beyond the end of the runway. For the purpose of this study, only the touchdown points within the touchdown zone are considered for the more detailed evaluations. The other points are neglected, acknowledging the fact, that the autopilot design used in this study would not fully meet the autoland requirements discussed in Chapter 3.1. An operational justification for omitting the points outside of the touchdown box is the use of a warning system preventing long landings. If detected, such a runway overrun protection system would prompt a go-around.

The mean of all touchdown points is generally located close to the case where only a steady wind without turbulence was simulated (depicted in Figure 21). The means for 5 m/s, 2.5 m/s and 1 m/s wind with light turbulence are located at 283.49 m (277.78 m without turbulence), 319.89 m (323.30 m without turbulence) and 347.25 m (352.82 m without turbulence) behind the LTP.

Apart from the mean value, especially the dispersion of the touchdown points is of interest. While the mean value would relate to the nominal touchdown point, the dispersion drives the σ_{FTE}. Special care has to be taken when evaluating the dispersion and describing it as standard deviation of a Gaussian distribution (as is being done when working with σ_{FTE}). Figure 25 shows a histogram of the distribution of the touchdown points behind the LTP for the same three steady wind scenarios as before and severe turbulence.

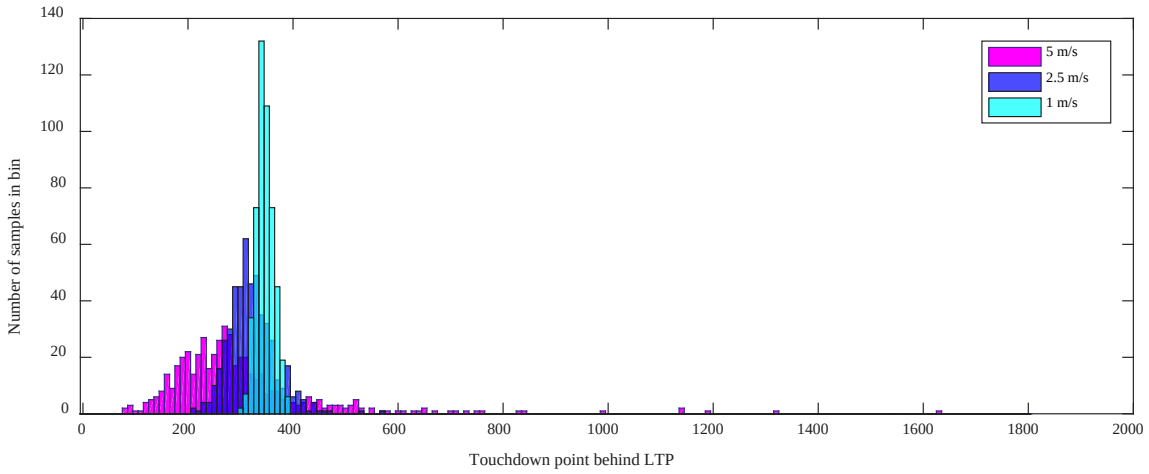

Figure 25 Histogram of the touchdown points behind the LTP for different steady wind scenarios and severe turbulence with 500 simulation runs for each case. The bins were selected at a width of 10 m.

It is obvious from the histogram and confirmed by the Kolmogorov-Smirnov [68] and the Anderson-Darling test for normality [69] at a 5% significance level that the distribution of data points is not Gaussian distributed. The resulting distribution is asymmetric and skewed. Especially for larger wind speeds, the land long side has significantly more points at large distances behind the core of the distribution than landings that occurred close to the beginning of the runway. Figure 26 shows a quantile-quantile plot of the distribution of the touchdown points for a steady wind of 5 m/s and severe turbulence with the Gaussian fit curve (fitted to the data between 25^{th} and 75^{th} percentile). One data point where the aircraft touched down far behind the end of the runway is excluded from the data set and the graph as this “floating” of the aircraft is to be considered a weak point of the model rather than a case that would likely occur. As previously mentioned, also the data points of the landings that occurred outside the touchdown box are disregarded for the statistical analysis but shown here for illustration purposes. In this plot, samples from a Gaussian distribution would appear as a straight line. While the core of the data is very close to linear, it can be seen that the tails, especially on the land long side, appear non-linear in this way of plotting. This is a result from the non-Gaussian distribution of the data in the tails.

In order to describe the distribution and not underestimate the risk of landing outside of the touchdown box two different methods are discussed. The first one is a process called overbounding. In this process a Gaussian distribution is used to describe the touchdown dispersion in such a way that the mass in the tails of the overbounding distribution is larger than the mass of the sample. The blue solid line in Figure 26 shows a Gaussian overbound as determined in the following. The second method is modelling the touchdown points by a Johnson distribution that allows a better description of the obtained results.

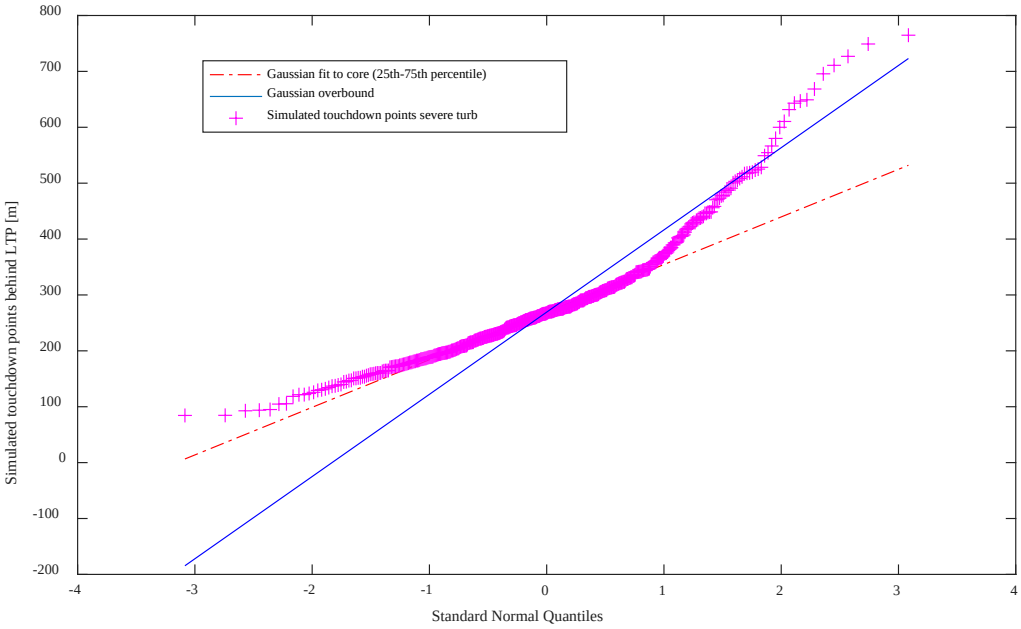

Figure 26 Quantile-quantile plot for simulated touchdown points (5 m/s steady wind component with severe turbulence, magenta crosses) with Gaussian fit for data between the 25th and 75th percentile (red dash-dotted line). The blue solid line shows the Gaussian overbound as determined in the following.

Gaussian Overbounding

In order to describe the data by a Gaussian distribution an experimental overbound of the data is derived based on an evaluation of the cumulative distribution function (CDF). The overbounds are defined such that

$$\begin{aligned} \Phi_{overbound}(x) &\geq \Phi(x) \;\; \forall x \leq NTDP - 1.5 \cdot \sigma_{overbound} \\ \Phi_{overbound}(x) &\leq \Phi(x) \;\; \forall x \geq NTDP + 1.5 \cdot \sigma_{overbound} \end{aligned} \tag{51}$$

where $\Phi = \int_{-\infty}^{x} f(x)dx$ is the CDF of a random variable x with a Gaussian probability density function (PDF). In this way it is ensured that the mass in the tails of the Gaussian overbound is larger than that of the sample obtained by Monte-Carlo simulations. Note that the overbounding condition in Equation (51) is only chosen to hold in the tails of the distribution outside $\pm 1.5\sigma_{overbound}$, but not necessarily at the core. The measure of $\pm 1.5\sigma_{overbound}$ appears to be a reasonable choice for the data at hand, however, it is not a fixed quantity. It should rather give some flexibility to not having to choose overly large overbounding sigmas in order to accommodate data at the core of the distribution while the interest of ensuring a safe landing is rather in the tails of the distribution. Also note that for choosing an overbounding distribution the NTDP has to be chosen or determined. As can be seen in Figure 25, the NTDP depends on the head wind component, and, as will be shown later in Section 4.4.2, also on the aircraft mass and location of the center of gravity. In the context of this study the NTDP for the Gaussian

overbound was set to the touchdown point for the simulation scenario with the parameters given in Table 4-2, with no wind, shown by the red diamond in Figure 21 and Figure 22 at a distance of 364.5 m behind the runway threshold. It should be noted that the choice of the NTDP, however, affects also the overbounding sigma so that for different choices of NTDP also different overbounds will be obtained.

With the conditions from Equation (51) the resulting experimental overbounding standard deviation of the FTE in the 5 m/s and severe turbulence case was found to be 147.1 m (see also Figure 26). The CDF and 1-CDF plots for the obtained autoland results and the experimental overbound are depicted in Figure 27. The blue dashed line shows the CDF of the sample, the blue solid line shows 1-CDF of the sample. The red lines show the experimental overbound and are centered at the NTDP. The black line indicates the $\pm 1.5\sigma_{overbound}$ interval for which the overbounding condition (51) does not necessarily have to be fulfilled.

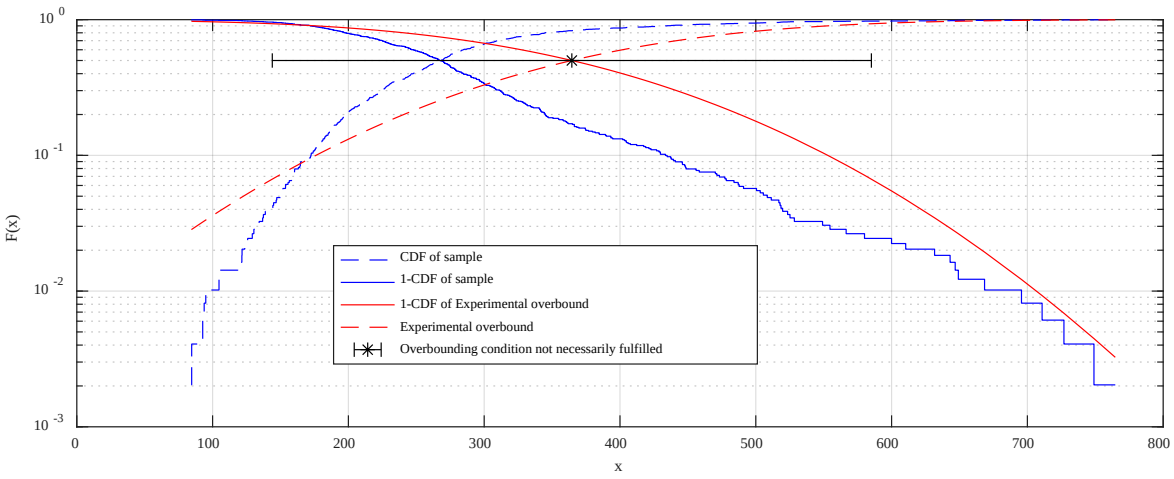

Figure 27 Semi logarithmic CDF and 1-CDF plots for the sample data (blue for 5 m/s wind and severe turbulence) and corresponding overbound (red) with NTDP at x=364.5 m determined by a landing without wind.

It can be seen that due to the asymmetry of the results, the overbound is driven by data on one side of the distribution, the land-long case in this example. For the other simulated cases the overbounds and Gaussian fits were derived in the same way as described for the two cases and are summarized in Table 4-4. Together with the sigmas, the median of the data set is listed in order to show an indication of the distance between the NTDP in the case without wind and the location of the core of the experimental distribution. Furthermore, the p-value of the Anderson-Darling test for normality is given. The p-value is used in hypothesis testing and compared to a significance level of choice (typically 5% or 1%) in order to decide if the sample data is from the assumed distribution. A p-value smaller than the significance level leads to a rejection of the H0-hypothesis that the sample data is drawn from a given (Gaussian) distribution. The results show for all overbounds p-values in the order of 10^{-6} indicating a significant deviation from the assumed normal distribution. That is, however, not surprising as the data

indicates a non-Gaussian distribution and the overbound is defined with the target to use a Gaussian distribution with more mass in the tails than the obtained sample. It is explicitly not aiming at providing a good fit to the data. Finally, the table also includes the calculated probabilities of landing outside the touchdown box (land short and land long case) assuming the NTDP at 364.53 m behind the threshold and the touchdown dispersion described by the overbounding σ_{FTE}. It can be seen that the critical case is always the land short case since the Gaussian distribution is symmetric and the NTDP is located closer to the beginning of the touchdown zone.

Wind	Gaussian fit σ_{FTE} (m)	Gaussian overbound σ_{FTE} (m)	Median (m)	p-value of AD test for overb.	Prob.of landing short (overbound)	Prob. of landing long (overbound)
1 m/s, lgt turb.	16.0	27.4	347.1	1.200e-6	8.018e-29	(machine) 0
1 m/s mod turb.	15.5	26.5	345.3	1.200e-6	1.119e-30	(machine) 0
1 m/s sev turb	16.2	27.6	345.1	1.200e-6	1.959e-11	(machine) 0
2.5 m/s lgt turb.	45.7	88.3	315.2	1.200e-6	2.935e-4	1.040e-7
2.5 m/s mod turb.	44.5	85.5	316.5	1.200e-6	1.925e-4	4.112e-8
2.5 m/s sev turb	44.5	70.9	315.7	1.200e-6	9.294e-6	5.021e-11
5 m/s lgt turb.	106.8	144.4	265.1	1.222e-6	1.777e-2	7.493e-4
5 m/s mod turb.	108.4	152.2	263.1	1.217e-6	2.306e-2	1.297e-3
5 m/s sev turb.	110.8	147.1	267.4	1.222e-6	1.953e-2	9.145e-4

Table 4-4 σ_{FTE} evaluated for Gaussian fit and Gaussian overbounding for different wind and turbulence intensity together with the corresponding median of the simulated scenario, the resulting land short and land long probabilities and the p-value of the Anderson-Darling test as goodness of fit measure.

Johnson Distribution

A different approach than Gaussian overbounding is modelling the touchdown performance by a distribution that fits better to the observed data. The Johnson distribution is a four-parametric distribution that is "often applied to FTE and TSE data" [70] because it allows a better description of the skewness and kurtosis of the obtained results than a Gaussian distribution. The distribution is obtained by a transformation of the normal distribution as

$$z = \gamma + \delta g(y) \tag{52}$$

where $y = \frac{x - \xi}{\lambda}$, x is the random variable to be described, z is standard normal distributed random variable, $g(y)$ is an appropriate transformation function, and γ, δ, ξ and λ are the four parameters of the Johnson distribution. In [71] Johnson describes three different types of distributions that are derived from a transformation of the form of (52).

- *SL* for the log-normal type (or semi bounded) obtained by putting $g(y) = \ln(y)$ with the PDF

$$f_{SL}(y) = \frac{\delta}{\lambda\sqrt{2\pi}\,y} e^{-\frac{1}{2}(\gamma+\delta\ln(y))^2} \quad \text{with } y > 0 \text{ and thus } x > \xi \tag{53}$$

- *SB* for the bounded case that is also obtained by putting $g(y) = \ln\left(\frac{y}{1-y}\right)$ with PDF

$$f_{SB}(y) = \frac{\delta}{\sqrt{2\pi}\,y(1-y)} e^{-\frac{1}{2}\left(\gamma+\delta\ln\left(\frac{y}{1-y}\right)\right)^2} \quad \text{with } \frac{y}{1-y} > 0 \text{ and thus } \xi < x < \xi + \lambda \tag{54}$$

- *SU* for the unbounded case obtained by putting $g(y) = \sinh^{-1}(y)$ with the resulting PDF

$$f_{SU}(y) = \frac{\delta}{\sqrt{2\pi(y^2+1)}} e^{-\frac{1}{2}\left(\gamma+\delta\ln\left(y+\sqrt{(y^2+1)}\right)\right)^2} \quad \text{with y} \in \mathbb{R} \text{ and } x \in \mathbb{R} \tag{55}$$

The simulated autoland data is analyzed by the Johnson Curve Toolbox for Matlab with the f_johnson_fit.m function that fits a Johnson distribution to observed data [72]. Based on a selected (or automatically chosen) fitting method (either based on moments or on quantiles) the appropriate type is chosen. Note that the SL and SB cases are, however, not defined for all values of x. That means that by using the SL or SB model not all values for the touchdown point are possible. This may not necessarily be considered a suitable model, or if the probability for the undefined touchdown points is set to 0 outside the ranges where it is defined, this may lead to an underestimation of the true risk of landing short or long. As for the Gaussian overbound, the CDF an 1-CDF for the observed data for the 5 m/s steady wind and severe turbulence case are analyzed and plotted. The fitting method based on quantiles yields a closer match of the data than the moments based method for the analyzed dataset. The selected type is the unbounded distribution *SU* . Together with the CDF/1-CDF of the sample also the CDF and 1-CDF of the obtained Johnson distributions are shown in Figure 28. Compared to the results obtained by Gaussian overbounding in Figure 27, the Johnson distribution has a much better agreement with the data. It should, however, also be noted that the Johnson fit does not ensure that the cumulative probability of the fit is always larger than the sample data. In this example this is e.g. the case for the data between about 150 m and 210 m on the x-axis. In order to be conservative it is also possible to inflate the scale factor λ (for the SU case) such that the inflated Johnson fit safely bounds the tails of the sample data, if desired.

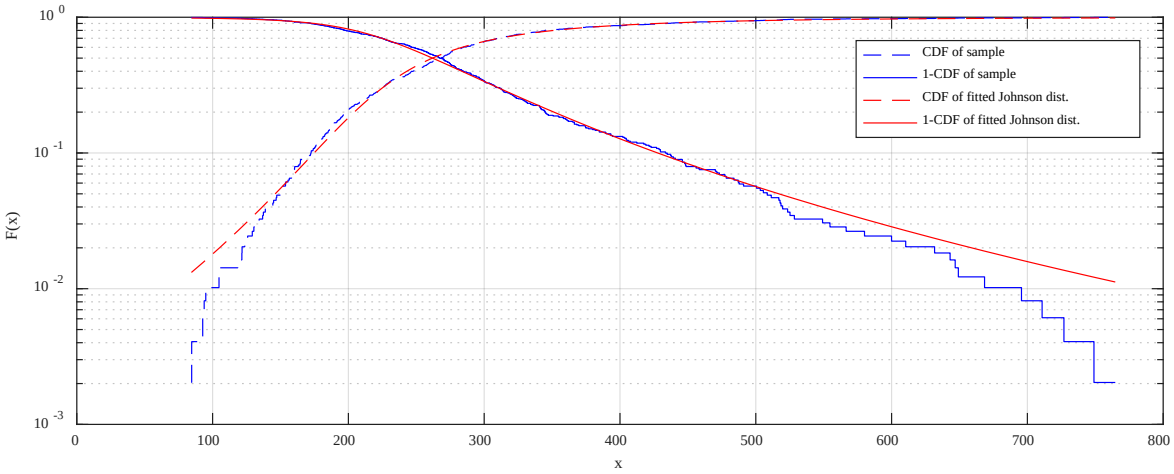

Figure 28 Semi logarithmic CDF and 1-CDF plots for the sample data (blue for 5 m/s wind and severe turbulence) and corresponding CDF and 1-CDF of fitted SU Johnson distribution (red).

Table 4-5 summarizes the obtained results for modelling the obtained results by a Johnson distribution that bounds the tail risk. The four parameters are listed, together with the type of the distribution (bounded and unbounded) and the fitting method (moments or quantiles). The table furthermore lists the p-values for the Anderson-Darling test for the described Johnson distribution.

Wind	γ	δ	ξ	λ	Johnson type and fit method	p value of AD test	Probability of landing short	Probability of landing long
1 m/s, lgt turb.	0.584	1.455	305.130	102.221	SB / Q	0.828	0	0
1 m/s mod turb.	1.475	2.717	277.285	185.892	SB / M	0.645	0	0
1 m/s sev turb	-0.598	2.154	337.068	31.746	SB / Q	0.105	7.043e-12	6.255e-12
2.5 m/s lgt turb.	-0.495	1.297	297.529	48.238	SU / Q	0.607	2.618e-4	2.292e-4
2.5 m/s mod turb.	-0.687	1.692	291.066	81.307	SU / Q	0.499	1.211e-4	1.195e-4
2.5 m/s sev turb	-0.449	1.476	301.097	60.805	SU / Q	0.443	2.142e-4	8.769e-5
5 m/s lgt turb.	-0.871	1.190	200.841	81.481	SU / Q	0.044	7.578e-3	8.708e-3
5 m/s mod turb.	-0.839	1.241	202.556	89.780	SU /Q	0.045	8.760e-3	7.570e-3
5 m/s sev turb.	-0.742	1.094	210.737	70.016	SU /Q	0.023	8.503e-3	8.377e-3

Table 4-5 Parameters for a Johnson distribution describing the touchdown dispersion in different wind and turbulence cases, together with the type and fitting method, the p-value of the Anderson-Darling test as goodness of fit measure and the resulting land short and land long probabilities.

It can be seen that the p-values are significantly larger than for the Gaussian overbound indicating a better fit of the Johnson distribution to the data. For the 1 m/s and 2.5 m/s wind cases the H0-hypothesis cannot be rejected at a 5% significance level. Finally, the table also includes the resulting probabilities of landing short or landing long, based on the chosen Johnson distribution. Note that for the first two cases in the bounded case the probability is zero which is probably an optimistic assertion of the risk. However, comparing the Gaussian overbound values for the land short and long probabili-

ties in those cases the risk is extremely small. In the 2.5 m/s case the land short risks are in a comparable order of magnitude, while the land long risk is assessed to be larger by the Johnson distribution than the Gaussian overbound due to the location of the NTDP closer to the beginning of the touchdown zone. This result indicates that when using the Johnson distribution as model for the FTE performance, it is not sufficient to consider the land short case only because it cannot be safely assumed that this case is driving the probability of landing outside the box.

4.4.1.3 Realistic wind cases

In order to also investigate a set of realistic wind speeds and directions, automatic airport weather reports (METAR) from Munich airport were used as input for the autoland simulations. METARs are generated every 30 minutes (more often if significant changes of the weather conditions occur) and contain information about the mean wind speed and direction. If the difference between the average wind speed and peaks wind speeds in gusts is significant (> 5 kts) gusts are reported additionally. The month of November of the year 2012 was used as input for the simulations that included 1437 weather reports. Turbulence intensity was simulated again by applying the Dryden wind models with $2 \cdot 10^{-1}$ the probability of exceedance of high altitude intensity if the wind speed was below 10 kts, 10^{-1} for wind speeds above 10 kts, 10^{-2} if gusts were reported and remained at or below 20 kts, 10^{-3} if gusts were reported between 21 and 30 kts and 10^{-4} for gusts above 30 kts. The maximum tailwind component considered was 4 kts. Otherwise it can be assumed the approach and landing direction would have been changed. In the cases with a larger tailwind the wind direction was changed by 180° which would be equivalent to changing the landing direction on the runway. For each approach a random sample from a uniform distribution for the aircraft mass and location of the center of gravity in the specified ranges were drawn. All parameters are again summarized in Table 4-6.

Aircraft mass	Aircraft CG	V_{TAS}	Initial altitude	Wind direction	Wind speed	Turbulence intensity
50-64.5 t (uniform distr.)	*15-45% (uniform distr.)*	70 m/s	609.6 m (2000 ft)	*as described*	*as reported*	*as described*

Table 4-6 Parameter set used in autoland simulations to evaluate impact realistic wind scenarios.

Figure 29 shows the obtained touchdown points on the runway. Out of the 1437 simulation runs eight touchdowns occurred at behind the runway (seven of them outside the plot limits) and 14 touchdowns occurred outside the landing box. However, that again is considered to be a weakness of the model and those points would trigger a warning and a go-around of the aircraft in case they happened in reality. Figure 30 shows a QQ-plot (Quantile-Quantile) for the distribution of the touchdown points on the runway. The core of the distribution again appears very close to linear, however, the tails are signifi-

cantly non-linear in this representation hinting at non-Gaussian distributed data. This result is again confirmed by the Anderson-Darling and Kolmogorov-Smirnov test at a 5% significance level.

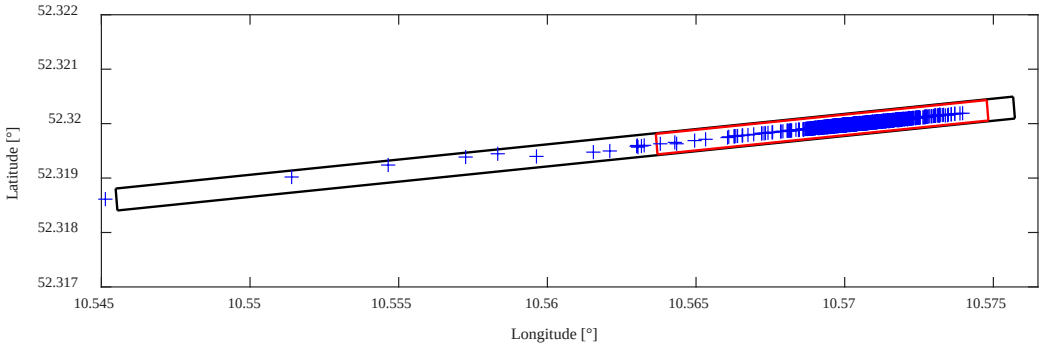

Figure 29 Touchdown points on runway and in relation to the touchdown box for recorded winds from Munich Airport in November 2012 with uniform distributed landing weight and center of gravity location between their respective maximum and minimum values.

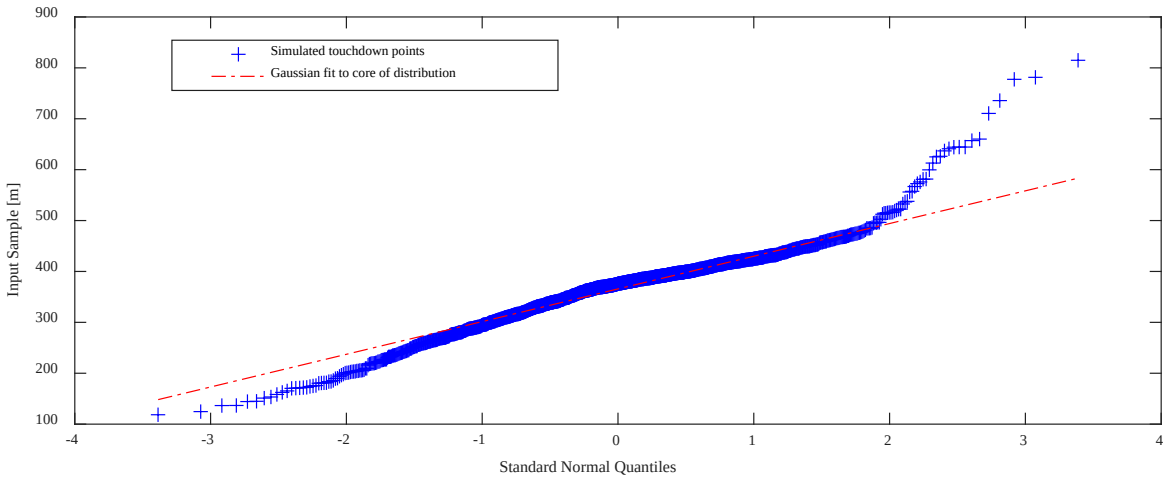

Figure 30 Quantile-quantile plot for simulated touchdown points (recorded winds from Munich Airport in November 2012 with uniform distributed landing weight and center of gravity location between their respective maximum and minimum values) with Gaussian fit for data between the 25th and 75th percentile.

The non-Gaussian distribution of the touchdown points requires again either a Gaussian overbound or the fit of a Johnson distribution to the obtained results. Both methods were applied and the results are shown in Figure 31. The Johnson SU curve with moments fitting method ($\gamma = -0.1987,\ \delta = 1.5788,\ \xi = 351.6510,\ \lambda = 130.5373$) again provides a better fit to the experimental data than the Gaussian overbound ($\mu = 364.53m,\ \sigma_{FTE,overb.} = 147.22m$). Especially for the land-short case the overbound results in a significant over-estimation of the risk of landing outside the touchdown box. On the land-long side both methods yield similar results for estimating the risk of landing long, however, the Johnson curve is more shape-preserving that the Gaussian model.

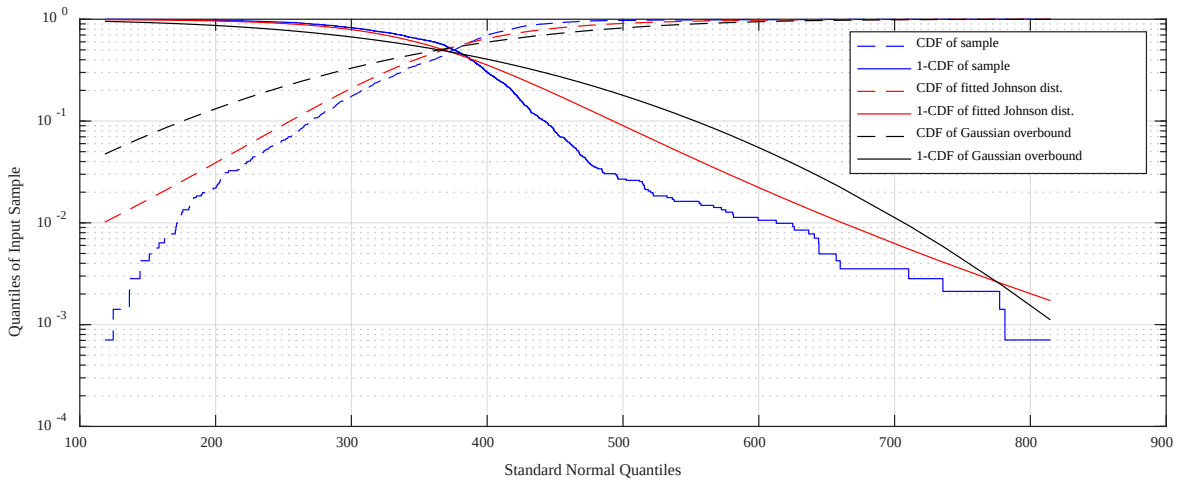

Figure 31 Simulated touchdown points with recorded winds from Munich airport modelled by inflated Johnson curve and Gaussian overbound.

In summary of the discussion of the wind and turbulence influence, it was shown that wind and turbulence intensity have a significant impact on the touchdown point of the aircraft. With a certain prevailing steady wind direction and wind speed the nominal touchdown point varies substantially. For the given aircraft and autopilot model the variation of the touchdown point for a headwind and a tailwind scenario with a steady wind of 5 m/s were in the range of about 200 m. Considering also turbulence in addition to the steady wind causes the touchdown points to vary additionally about the respective nominal touchdown points. In the requirement derivation process this variation is described as standard deviation of a Gaussian distribution. It was, however, found that only the core of the resulting distribution of the touchdown points was close to Gaussian while for the tails the Gaussian distribution was not a good fit (visible in the QQ plots). Thus, an overbound was determined in order to not underestimate the tail probability that is of special interest in this kind of integrity evaluations. Furthermore, it was also found that the touchdown points are more spread out for the land long case than for the land short case (floating of the aircraft in the ground effect) and the overbound of σ_{FTE} is thus usually driven by the land-long case. For all cases it is challenging to define an NTDP. While based on simulations an NTDP can be found by not simulating any wind influence, this may not in general be a good and valid assumption for a specific approach with a steady wind component.

Finally, modelling the touchdown errors by a Johnson distribution yielded significantly better results in terms of goodness of fit. The shape of the distribution was matching the shape of the actual distribution better than a Gaussian distribution. It is therefore preferable to use a Johnson distribution to model the touchdown performance.

4.4.2 Aircraft mass and center of gravity location

In addition to the wind, also the aircraft mass and location of the center of gravity (CG) have an influence on the touchdown performance. These parameters usually vary for each flight. In order to keep the aircraft in safe flying conditions and within the load limits during take-off, cruise flight and touchdown, the range of permissible aircraft masses and corresponding location of the center of gravity is specified in the weight and balance sheet for each aircraft. An example for such a sheet from the manual of the Airbus A320 is given in Figure 32. The weight and CG combinations indicated by the red box in Figure 32 are considered for the simulations of the touchdown performance. The landing weight was varied from 50 t to 64 t and the CG location between 15% and 45% of the mean aerodynamic chord (MAC). For the Airbus A320 this corresponds to CG locations of 16.9 m and 18.1 m behind the nose of the aircraft. No wind influence was considered, the approaches were again started below the glide path and with an initial lateral offset of 102 m. The simulation parameters are again summarized in Table 4-7 and the outcome shown in Figure 33.

Aircraft mass	Aircraft CG	V_{TAS}	Initial altitude	Wind direction	Wind speed	Turbulence intensity
50-64 t (steps of 1 t)	*15-45% (steps of 5%)*	70 m/s	609.6 m (2000 ft)	off	off	off

Table 4-7 Parameter set used in autoland simulations to evaluate impact of center of gravity location and aircraft landing weight.

The touchdown points show a significant dependency on the location of the weight and balance of the aircraft on the touchdown performance. The nominal touchdown point (without any wind influence) varied for the different combinations between 455.5 m (CG at 15% MAC and landing weight 64 t) and 514.5 m (CG at 20% and landing weight 50 t) behind the runway threshold. In general it is observable that the touchdown point is closer to the threshold for more forward CG locations and higher landing weight, and moves further away from the threshold with decreasing weight and CG locations moving aft. As it used to be already difficult to define a meaningful NTDP for the different wind scenarios, the results in this simulation show that also the weight and balance of the aircraft impact the NTDP.

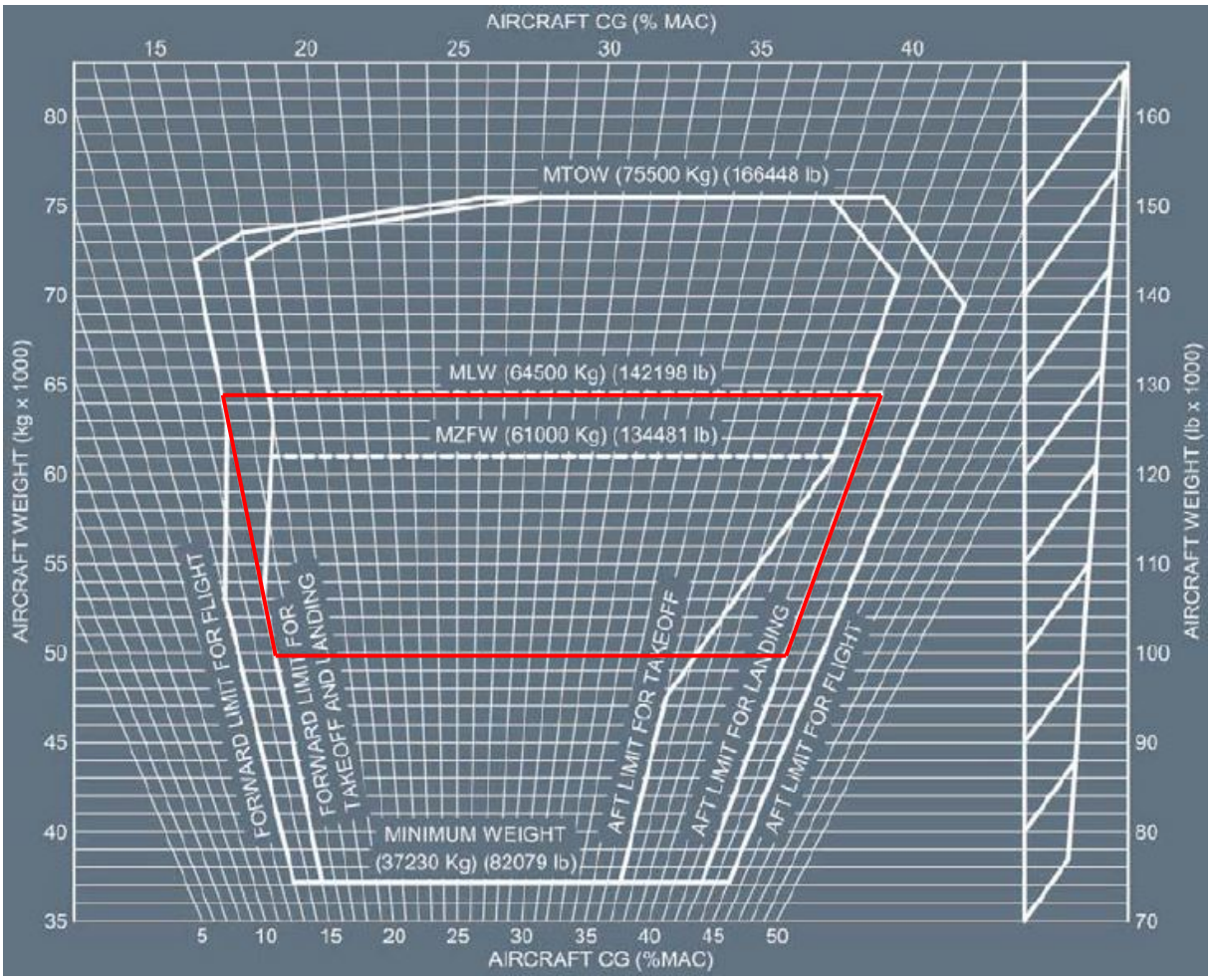

Figure 32 Weight and balance sheet for the Airbus A320 [73]. The area shown in red was used for simulation purposes.

This once again points to the conclusion that it is problematic in the tradeoff between NSE and FTE to assume one fixed NTDP that should hold for all aircraft in all configurations and wind cases. However, the landing weight of the aircraft and the location of the CG are quite well known quantities. It could thus be beneficial to leverage this knowledge inside the aircraft in order to use a more realistic value for the NTDP. This can be done either by following the standard method to assume an NTDP (now chosen once according to weight and balance of the aircraft on approach) with a Gaussian distribution modelling the FTE. The other alternative is to use a better description of the actual touchdown performance, e.g. by modelling it as a Johnson distribution and derive the NSE requirements from these results. The potential benefit of using existing knowledge about landing weight and CG location when doing the Johnson distribution modelling is shown in the next section. A description how the tradeoff between NSE and FTE based on a Johnson distribution can be accomplished follows in Section 4.6.

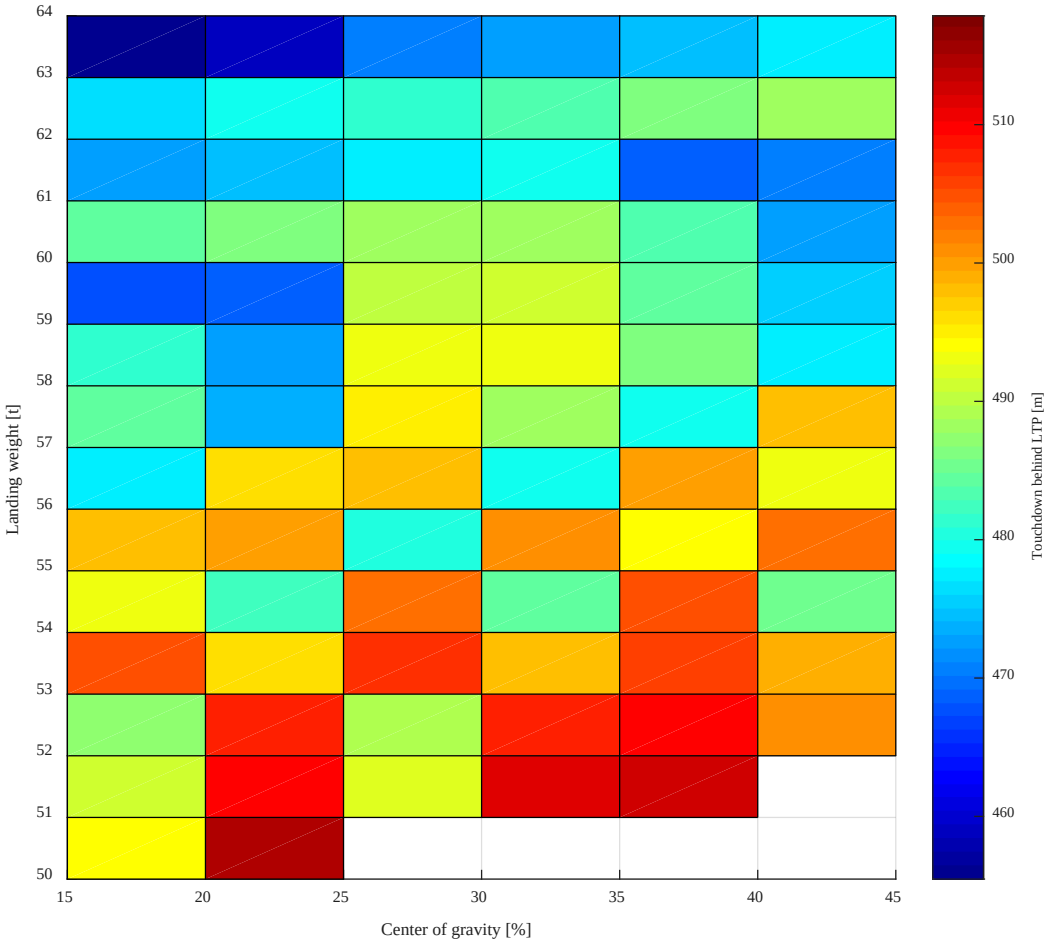

Figure 33 Touchdown point with no wind as function of aircraft mass and center of gravity location.

4.5 EXEMPLARY LEVERAGING OF KNOWLEDGE BY RESTRICTING PARAMETERS

One of the main paradigms followed in this work is to use available information to improve models, reduce conservatism and therefore gain in performance of the autoland system. The autoland simulations in the last section were performed by varying a number of influencing parameters in order to obtain results that somehow cover the whole range of possible parameter combinations. However, the results may not be completely representative for a specific approach with a given set of aircraft parameters, such as weight and center of gravity location. Therefore, it is beneficial to actually take into account known parameters and obtain better and more realistic results. As example, the results from Section 4.4.1.3 (realistic wind scenarios from Munich Airport) are reused and compared to a case where the same parameter set is used for simulations but the landing weight and CG location are fixed at a specific value, 64.5 t and 22.2% as example. Both simulation runs contained 1437 runs (corresponding

to the weather reports for the month of November 2012 downloaded from [74]) and the other parameters used are again summarized in Table 4-8. The results are shown in Figure 34.

Aircraft mass	Aircraft CG	V_{TAS}	Initial altitude	Wind direction	Wind speed	Turbulence intensity
64.5 t	*22.2%*	70 m/s	609.6 m (2000 ft)	*as described*	*as reported*	*as described*

Table 4-8 Parameter set used in autoland simulations to evaluate impact of fixing parameters.

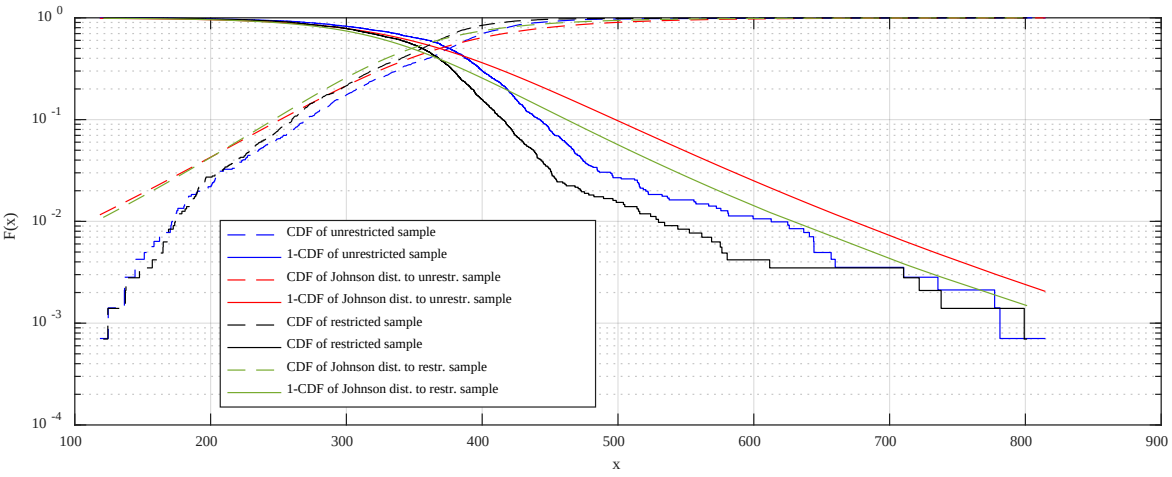

Figure 34 Johnson curves (red and green) modelling the touchdown point distribution for the full range of parameters (blue) and the distribution for a specific loading condition of the aircraft (black).

When restricting the number of parameters varying in the autoland simulations of course also the variation of the touchdown points is reduced. For this case of considering only the wind influence as random influence but not the weight and CG location, the difference in assessing the land short probability changes from $4.959 \cdot 10^{-3}$ to $4.363 \cdot 10^{-3}$. For the land long case, the change from $1.884 \cdot 10^{-3}$ to $1.203 \cdot 10^{-3}$ is somewhat larger than for the land short case. Less variation in the touchdown points can then be leveraged in the trade-off between NSE and FTE error budgets as will be described in the next section. Similar to the aircraft mass and center of gravity location, it is also possible to leverage any knowledge that might be available about the range of expected winds and other parameters not considered in this exemplary study (such as radar altimeter performance, runway slope, etc.).

4.6 APPLICATION TO NSE/FTE TRADE-OFF

The results from the previous sections in this chapter show that the touchdown performance is subject to a variety of different influencing parameters. The obtained results for the simulated touchdown performance cannot, in general, be expected to follow a Gaussian distribution. Therefore, two approaches to describe the obtained simulation results were discussed: Gaussian overbounding and modelling the results by a Johnson distribution.

The former method has the advantage of simplicity. As described in Equation (28) in Section 3.2, the TSE is the root sum square of the NSE and FTE, assuming both can be properly described by a Gaussian distribution. In that way, a trade-off between the two is easily possible. Fitting the touchdown data to a Gaussian distribution may result in underestimating the risk of landing outside of the touchdown box and should therefore be avoided. In order to maintain safety, a Gaussian overbound can be used that has more mass in the tails of the distribution than the sample obtained from the autoland simulations. This method, however, introduces a lot of conservatism and does not yield optimal results.

Furthermore, when evaluating the TSE against the landing box requirement, a mean value for the Gaussian distribution has to be defined, namely the NTDP. The NTDP is also variable depending on the weight and balance as well as external influences, such as steady winds.

The other method discussed was to use a Johnson distribution to model the autoland performance, potentially also with inflating the distribution's shape parameter to ensure that the tail probabilities are not underestimated. For the obtained data this method yielded a significantly better description of the touchdown performance than the Gaussian model. However, when assuming the FTE to be Johnson distributed while the NSE can reasonably be assumed to be Gaussian distributed, the tradeoff between NSE and TSE is not as simple as in the case of two Gaussian distributions. Modelling the joint probability of the sum of two random variables with different independent distributions f and g the joint PDF can be described by the convolution of the two distributions as

$$(f * g)(x) = \int_{-\infty}^{\infty} f(x-y)g(y)dy \tag{56}$$

For the case of touchdown performance evaluation let e.g. $f(x)$ be the Gaussian distributed PDF of the NSE and $g(x)$ the PDF of the Johnson distributed FTE. Then the joint PDF p for the touchdown point x can be described as

$$p(x) = \frac{1}{\sqrt{2\pi}\sigma_{NSE}} \exp\left(-\frac{x^2}{2\sigma_{NSE}^2}\right) * \frac{\delta}{\lambda\sqrt{2\pi}\sqrt{1+\left(\frac{x-\xi}{\lambda}\right)^2}} \exp\left(-\frac{1}{2}\left(\gamma + \delta \sinh^{-1}\left(\frac{x-\xi}{\lambda}\right)\right)^2\right) \tag{57}$$

for the case of a Johnson SU distribution and the NSE with zero mean. In the case of different distributions (as it is the case in this study) it is generally not possible to derive a simple analytic limiting con-

dition for σ_{NSE} as in the case of two Gaussian distributions (the assumption in the derivation of the requirements described in Chapter 3). However, this tradeoff can always be solved numerically, with special care for numerical stability and accuracy of the chosen integration method. The effort of this method is similar in terms of simulation effort. Additional simulations may have to be run when certain parameters are restricted (such as the landing weight and CG) such that in a later trade-off a more realistic model can be used.

The land short condition for the nominal case (previously described in Chapter 3 based on the assumption of Gaussian distributed NSE and FTE) can then be formulated as

$$p(x < 61m) = \int_{-\infty}^{61m} p(x)dx \leq 10^{-6} \tag{58}$$

and similarly for the land long case

$$p(x > 823m) = \int_{823m}^{\infty} p(x)dx \leq 10^{-6} \tag{59}$$

with $p(x)$ from Equation (57) (or with a different PDF for a model other than the Johnson SU) and the land short limit at 200 ft (≈61 m) behind the runway threshold and the land long limit at 2700 ft (≈823 m) behind the threshold. Assuming the parameters from Section 4.4.1.3 with the realistic wind scenarios from Munich Airport (Johnson SU distributed FTE with $\gamma = -0.1987$, $\delta = 1.5788$, $\xi = 351.6510$, $\lambda = 130.5373$ and a Gaussian distributed along-track NSE at touchdown with $\mu_{NSE} = 0$ and $\sigma_{NSE} = \frac{\sigma_{NSE,vert}}{\tan(GPA)} = \frac{1.72m}{\tan(3°)} = 32.82m$) the probability of landing short would be 1.3e-3 and the probability of landing long is 3.5e^{-4}. The PDF of the Gaussian NSE, the Johnson FTE and the convoluted TSE are shown in Figure 35.

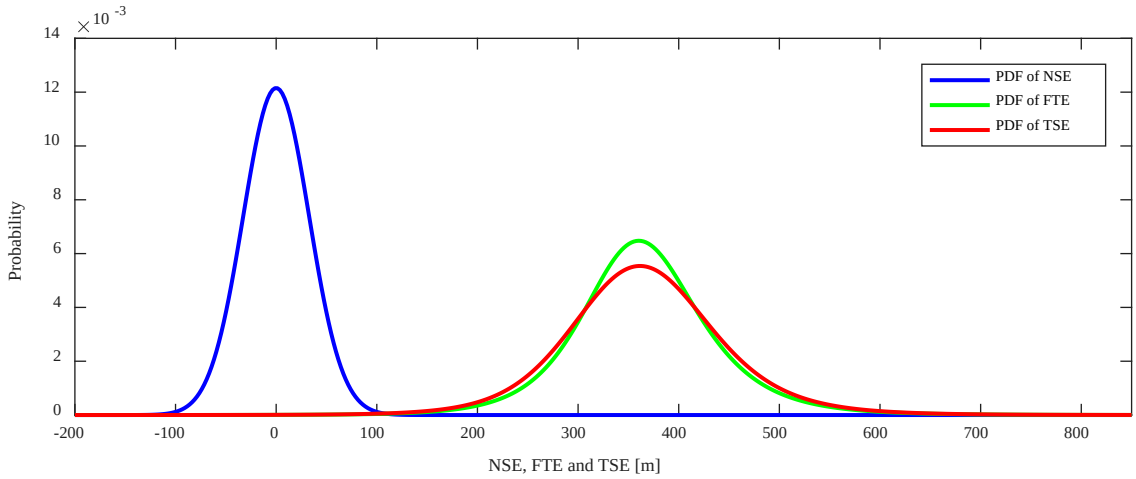

Figure 35 Probability density functions of NSE, FTE and TSE

Note again that for the autopilot and the simulated results at hand the required touchdown performance with a tolerable risk of landing outside of the box with a probability of not more than 10^{-6} could not be achieved.

Apart from the nominal case, also the limit case (according to CS-AWO) condition has to be fulfilled. Deriving a limit case monitoring condition is also possible based on assuming a Johnson distributed FTE. As described in Section 3.1.2, in the limit case condition one influencing parameter is kept at its most adverse value while all other parameters vary according to their expected distributions. Thus, in addition to the nominal variations, an error due to the limit case has to be considered. While the land short limit remains at 200 ft the land long limit for the limit case is extended from 2700 ft to 3000 ft (≈914 m) and the probability of landing outside the box has to be smaller than 10^{-5}. The land short and land long probabilities are varying according to their nominal distributions. Here again, the convolution of a Gaussian distribution (describing the NSE) and a Johnson distribution (describing the FTE) are used as described by Equation (57). The additional vertical position error E_v due to the limit case condition projects into the along-track domain by dividing the error by the tangent of the glide path angle. The land short and land long conditions can then be described as

$$p(x < 61m) = \int_{-\infty}^{61m} p(x)dx + \frac{E_v}{\tan(GPA)} \leq 10^{-5} \tag{60}$$

and

$$p(x > 914m) = \int_{914m}^{\infty} p(x)dx + \frac{E_v}{\tan(GPA)} \leq 10^{-5} \tag{61}$$

As previously described in Chapter 3, when assuming the NSE and FTE to be both normally distributed with known mean and standard deviation an easy limiting condition for the largest tolerable vertical position error E_v, and thus (by assuming a largest allowable projection factor $s_{vert,i}$ from the pseudorange into the position domain) for the largest tolerable pseudorange error can be derived. When considering the actual touchdown performance of an aircraft with a more suitable model it becomes impossible to standardize such a simple limit as the shape of the TSE distribution, and thus also the resulting shape of the limit on the pseudorange error is not known a priori. The limit imposed on the airborne GBAS monitors would rather have to be evaluated and be derived for each aircraft individually.

Finally, also in the malfunction case modelling the FTE as Johnson distributed and the NSE is feasible. In the malfunction case the NSE and FTE are fixed at their 95th percentiles. The limit can then be described as

$$200\,ft \leq NTDP - FTE_{95\%,landshort} - NSE_{95\%} - \frac{E_v}{\tan(GPA)} \tag{62}$$

and

$$NTDP + FTE_{95\%,landlong} + NSE_{95\%} + \frac{E_v}{\tan(GPA)} \leq 3000\,ft \tag{63}$$

Note that due to the asymmetry of the FTE a different value for the land short and land long case needs to be used, while the same value for the 95th percentile of the NSE can be used due to the symmetry of the Gaussian distribution. From Equations (62) and (63) a limiting condition for the vertical error E_v and thus also the range error E_r can be derived as described for the limit case condition.

The discussion in this chapter showed that assuming one nominal touchdown point and one Gaussian distributed performance model for describing the FTE at touchdown for all aircraft in all conditions can be a crude simplification of the actual encountered results. Fitting a Gaussian model to the touchdown distribution is a commonly used approach [11], [75]. However, when deriving NSE requirements with tolerable risks on the order of 10^{-5} to 10^{-9} fitting of the FTE distribution only to a Gaussian distributed core and neglecting deviations from Normality and heavier tails can lead to a significant underestimation of the probability of landing outside the touchdown box and ultimately to NSE requirements that do not in all cases ensure a safe landing.

In this work two approaches to cope with this problem were discussed: the application of the Gaussian overbounding concept to derive a conservative σ_{FTE} that is large enough to safely bound the tail risk. In that way the concept of a simple derivation of requirements can be maintained at the price of having a very conservative description of the FTE performance. The other approach suggested the description of the FTE performance by a more suitable distribution, such as the Johnson SU distribution. In that way the actual FTE performance can be modelled much better than by a Gaussian distribution, requiring significantly less conservatism in the trade-off between FTE and NSE performance. On the other hand, when considering an individual performance of a certain aircraft, and possibly also taking into account available knowledge about parameters, such as aircraft weight and balance, no standardization of a specific NSE performance is possible anymore. Instead, a probabilistic assessment has to be carried out in order to derive the limitations necessary to ensure a safe landing in the nominal, limit and malfunction case. This would, however, enable the largest potential gains in performance that could then be leveraged e.g. to optimize touchdown and roll-out [76]. From a practical implementation perspective, it is likely that the approach of describing the touchdown performance as a Gaussian distribution will be maintained. For the remainder of this work, this concept is therefore applied. It should be noted, however, that with the considerations from this chapter, a change to better fitting models is always feasible.

5 NSE Contribution and Ionospheric Gradient Monitoring

In this chapter, after a very brief discussion of the nominal NSE and its contributors, the issue of monitoring for ionospheric gradients in GBAS is discussed. The first part of this chapter discusses the ionospheric monitor in the ground system that is required for GAST D. A new monitoring architecture for single frequency GBAS ground stations is developed and discussed. The monitoring is based on actual satellite geometry at the airport and, furthermore, on the use of the actual glide path angle of a given approach. This increases the monitoring threshold at most airports and thus improves system availability and continuity and fulfills the task of monitoring for ionospheric gradients in the ground system.

In the second part an airborne monitor for a future dual-frequency GBAS is developed. This monitor is designed as airborne monitor so that it can leverage the actual FTE performance of a specific aircraft in specific conditions as described in the previous chapter. The monitor calculates pseudo-ionospheric delays from dual frequency GBAS corrections and compares them to a similar quantity calculated from dual frequency pseudorange measurements in the airborne system. The monitoring threshold is derived based on the FTE of the aircraft.

Contributions:

In this chapter an ionospheric gradient monitor for single frequency GAST D GBAS ground station is developed by adding an additional monitoring receiver. In contrast to existing algorithms and techniques, the monitoring requirement is not fixed but takes into account the actual current satellite geometry.
Furthermore, a dual frequency ionospheric monitor for future GBAS is developed that operates in the airborne system. Shifting the task of monitoring for ionospheric gradients to the airborne side enables an improved monitoring since no conservative assumptions about the airborne performance have to be made when deriving requirements for monitoring in a ground station.

Publications:

- M. Felux, J. Lee and F. Holzapfel, "GBAS ground monitoring requirements from an airworthiness perspective," *GPS Solutions*, vol. 19, no. 3, pp. 393-401, 7 2014. [14]
- M. Felux, M.-S. Circiu, J. Lee and F. Holzapfel, "Ionospheric Gradient Threat Mitigation in Future Dual Frequency GBAS," *International Journal of Aerospace Engineering*, vol. 2017, pp. 1-10, 2017. [15]
- M. Felux, M.-S. Circiu, D. Gerbeth and M. Caamano, "Ionospheric Monitoring in a Dual Frequency GBAS," in *Proc. IEEE Aerospace Conference*, Big Sky, MT, USA, 2016. [77]
- M. Felux, M.-S. Circiu, D. Gerbeth and M. Caamano, "Experimental Validation of an Ionospheric Monitoring Scheme for Dual Frequency GBAS," in *Proc. ION GNSS+*, Portland, OR, USA, 2016. [78]

In the previous two chapters the derivation process for GBAS navigation requirements and the FTE contribution as first main contributor to the TSE were described and discussed. In this chapter, a thorough view is taken on the contribution of the NSE. The NSE is considered to consist of nominal errors (such as receiver noise and nominal multipath effects for example) and non-nominal errors (such as for example excessive ionospheric delay caused by a large ionospheric gradient). After a short general description of NSE contributors, a more detailed description of the ionospheric gradient problem follows. The rest of this chapter is then dedicated to mitigation strategies for the ionospheric threat, the most challenging part of the NSE bounding and integrity assurance in GBAS. The discussions extend from current single frequency systems to future dual frequency systems and are always aiming at using available knowledge about the nominal NSE (and FTE for the dual frequency monitor), in order to reduce the conservatism in the derivation of requirements. This bears the potential to mitigate availability issued faced by current GBAS due to generalized and usually very conservative assumptions.

5.1 NOMINAL NSE

A comprehensive list of what is considered as nominal NSE contributor is given in [13] and reproduced here for convenience: Nominal noise and multipath as well as radio frequency interference (RFI) below the specified interference mask in the ground and airborne subsystems are considered as contributors to the error budget. Furthermore nominal ionospheric and tropospheric effects are considered. Finally, also a budget exists for nominal ranging source errors including such things as nominal signal imperfections or (small) code-carrier divergence effects caused by the satellite hardware.

In terms of integrity all these effects are accounted for in the protection level concept that was already described in Section 2.2.3.3. Nominal effects are easy to observe as they occur constantly. Therefore it is pretty straight forward to collect large amounts of data and build reliable models characterizing these effects. The situation becomes significantly more challenging when talking about non-nominal errors.

5.2 NON-NOMINAL NSE

Non-nominal error sources as described in [13] are considered to be single or multiple reference receiver hardware failures, a failure of the VDB, a failure of the processor architecture in the ground station, complex hardware and software failures, correlated multipath affecting multiple reference receivers, excessive code-carrier divergence, excessive acceleration of a satellite, erroneous GNSS

navigation data as provided by the satellite, a low power condition of a satellite signal, multiple ranging source faults and finally non-nominal ionospheric gradients.

In terms of integrity there is a variety of mitigation strategies for the different error sources. They consist of monitoring for specific conditions in the airborne and ground subsystems, siting restrictions for reference antennas, non-nominal protection level calculations, or are sufficiently unlikely to occur or are not endangering the safe landing of the aircraft (see limit and malfunction case performance demonstration in Sections 3.1.2 and 3.1.3). The most challenging threat to GBAS, however, remains the threat of ionospheric gradients. Its properties, as well as detection and mitigation strategies are described in the remainder of this section.

5.3 Ionospheric Threat Models and Necessity for an Ionospheric Gradient Monitor

The ionosphere is typically the largest single source of errors in single frequency GNSS navigation. Despite the fact that in a differential GNSS architecture, such as a GBAS, the largest portion of the error is removed by applying the generated corrections, a residual threat resulting from potential spatial decorrelation of the ionospheric influence has to be considered. This is especially important when considering integrity aspects of the system. The ionosphere is an atmospheric layer that begins at an altitude of about 80 km above the surface of the earth and extends to an altitude of about 1000 km. It contains different layers with varying plasma densities. The ionization of the particles in the ionosphere is strongly influenced by the radiation from the sun and the interdependencies with the earth's magnetic field. Thus, strong variations in the concentration of charged particles occur on a daily basis between day and night time. Furthermore, the periodic change of the number of sun spots results in a regular pattern, the so-called solar cycles. These cycles have a periodicity of about 11 years with varying intensity and are numbered starting from the beginning of detailed observations in the year 1755. The current cycle, since the year 2008 is thus number 24. The most significant gradients in the electron concentration of the ionosphere in a GBAS context were observed at the falling edge of cycle 23.

From these past observations it has been seen that the occurrence of strong ionospheric activity affects single frequency GNSS users and can cause potentially large positioning errors. A differential GNSS architecture like GBAS can only mitigate the part of the ionosphere which is common to a user and an aircraft approaching a GBAS station. From a safety point of view the potential spatial decorrelation of the ionospheric impact between the aircraft and ground station is important to characterize and bound. Under quiet conditions the decorrelation is small but in extreme situations gradients could become a potential danger for aircraft during approach and landing. In order to assess the nominal as well as potential worst-case impact on an airborne user, error characteristics need to be evaluated and then

assessed in the GBAS context. For that reason, each country operating a GBAS is required to define its own ionospheric threat model. This model contains a worst case gradient which may be experienced within the region of applicability but also the nominal ionospheric decorrelation for the location in quiet conditions. The nominal decorrelation is considered in the protection level in form of the σ_{vig} parameter (see Equation (22) in Section 2.2.2.3.5). The worst-case gradient is considered for integrity purposes and is the largest gradient from which the GBAS has to protect a user. In a GAST C station integrity parameters (usually σ_{vig} and/or σ_{gnd}) are artificially inflated in order to increase the VPL of a user. The inflation is performed such that the user VPL becomes larger than the VAL for satellite geometries that could result in unacceptably large position errors [54]. In GAST D no parameter inflation is performed, however, a significant monitoring effort is necessary to detect severe ionospheric disturbances and take appropriate action in case of detection. According to the final version SARPS the ionospheric gradient monitoring capability at an installation is determined for each approach. The ground station then broadcasts parameters for a linear error model that describes the largest residual error as a function of the distance of the corresponding runway threshold to the GBAS reference point. A larger distance would result in potentially larger residual errors. The distance between the ground station and the runway threshold can therefore be traded against the availability of the service. Together with a Code-Carrier Divergence monitor in the ground station, and the airborne monitors, it was shown that all monitors combined can achieve effective protection of the users against ionospheric gradients with slopes and speeds corresponding to worst-case observations for mid-latitudes. However, for equatorial regions the ionospheric threat is more severe and remains to be validated for GAST D.

While it would be desirable to have generally valid ionospheric threat models depending mainly on the geomagnetic latitude instead of political boundaries, current regulation requires GBAS threat models on a national level. They are derived based on worst-case historic measurements. This methodology, however, raises several questions in terms of reliability. The reliability of a model can be doubted if only data from a small country and/or data from only a small network are investigated. Furthermore, not all countries have a sufficient amount of historic data available to justify the validity of the model.

Furthermore, even if the models are derived from a reasonably good network with sufficient historic data there is no guarantee that in the future more severe conditions may not arise. For that reason, any established threat space should be continuously monitored and the national threat space updated in case any observations are made which exceed the established models. Effort should also be made to harmonize models with respect to methodology of establishing the parameters, required network density and geomagnetic latitude. The following sections present the threat model parameters and examples of national threat models as they are currently valid at the time of writing.

5.3.1 The ionospheric threat model parameters

An ionospheric threat model in the GBAS context is used to characterize and bound the error contribution in the nominal case, as well as during a worst-case ionospheric condition. Note that the values of all these models only refer to the delay experienced on the L1 frequency. As the ionospheric delay is a function of the total electron content (TEC) and the frequency of a signal, the threat models are different when using signals in the L5 band (the delay and thus the largest gradient is inflated by a factor of about 1.8).

The nominal conditions are described by the parameter σ_{vig} . It is the expected standard deviation of the decorrelation of the ionospheric conditions which occurs over distance due to nominal variations in the ionosphere. The σ_{vig} is used in the calculation of the total ionospheric uncertainty σ_{iono} which was previously described in Equation (22) in Section 2.2.2.3.5. It is repeated here for convenience and readability and is given according to DO-253C [38] Section 2.3.12.3 as

$$\sigma_{iono} = F_{PP} \cdot \sigma_{vig} \cdot (x_{air} + 2\tau \cdot v_{air}) \tag{64}$$

The factor F_{PP} is a vertical-to-slant obliquity factor depending on the elevation of the satellite under consideration, x_{air} is the distance between the GBAS reference point and the aircraft, τ the smoothing filter time constant and v_{air} the horizontal speed of the aircraft. The total ionospheric uncertainty is then further used to calculate the total uncertainty associated with the corrected measurement from a specific satellite and to calculate the protection level as error bound as described in Equation (19) in Section 2.2.3.1.

The worst case decorrelation with distance introduced by an ionospheric gradient is described by the so-called “wedge model” which characterizes an ionospheric gradient as a linear ramp as shown in Figure 36.

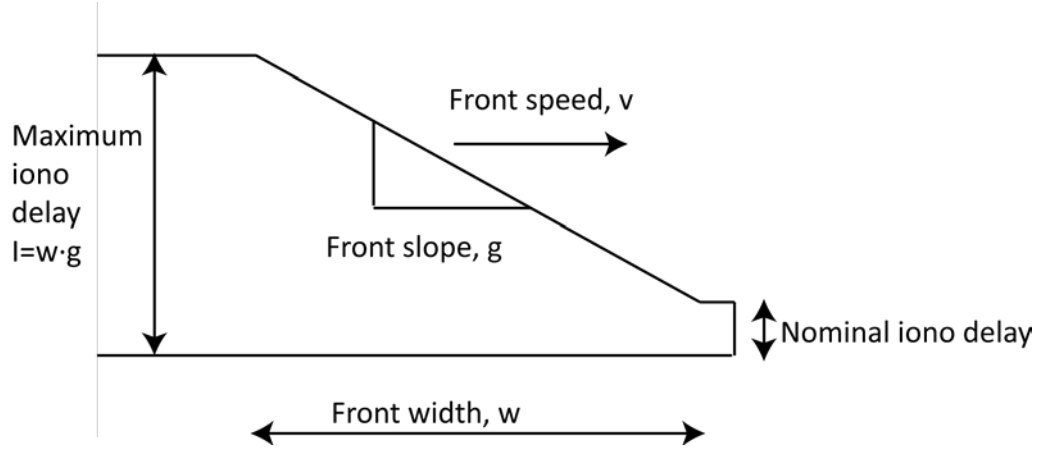

Figure 36 Model of an ionospheric ramp

The ionospheric gradient is characterized by three parameters: the slope g, the width w and the speed v at which the front is moving. These parameters are derived from networks of reference receivers and historical data. From these parameters the largest impact of such a disturbance on a user can be derived in simulations as described e.g. by Harris and Murphy [55].The derivation of these parameters is the task of defining an ionospheric threat model. The results from these assessments for Germany, the Contiguous United States (CONUS) and Korea are described in the following sections and compared afterwards.

5.3.2 CONUS ionospheric threat model

The threat model for the ionospheric impact in the CONUS region was developed by Pullen et al. [43] based on data from the network of Continuously Operating Reference Stations (CORS). An automated process screened for apparent gradient and sorted out a large number of detected events which were caused by obvious receiver or data problems, such as high multipath, cycle slips or other events typically caused by a non-optimal receiver location. Further manual analysis of the remaining events was performed to exclude apparent errors which were not detected by the algorithms. From the remaining set of validated events the ionospheric threat model parameters were derived. The largest gradient from validated data was found in data from 20 November 2003, where a gradient of 412mm/km was observed. Furthermore, a dependency on the elevation el of the satellite was found resulting in a piecewise linear threat model with maximum gradients g given by

$$g \leq \begin{cases} 375 mm/km & \text{for } el < 15° \\ 375 + (el - 15) mm/km & \text{for } 15° \leq el < 65° \\ 425 mm/km & \text{for } el > 65° \end{cases} \tag{65}$$

The corresponding front speeds were found to be below 750 m/s with respect to the ionospheric pierce points in a thin shell ionosphere model and the front width were between 25 km and 200 km.

5.3.3 German ionospheric threat model

The model for Germany was established in 2009 by Mayer et al. [44]. It is based on measurements taken over the period of one solar cycle (11 years) between the years 1998 and 2008. In a first step, a pre-screening of data from latitudes between 45°N and 58°N was performed to find days with high ionospheric activity. Next, a denser network of reference receivers within Germany only was used to derive the threat model parameters. In total 26 events were considered and analyzed. The observations also found some significant gradients, however far from the magnitude found in the CONUS region. The largest gradient was found to be 118 mm/km with a similar dependency on satellite elevation as in the US. The German threat model is thus also described by a piecewise linear model given as

$$g \le \begin{cases} 40\ mm/km \text{ for } el \le 30° \\ 40 + 2.5 \cdot (el - 30)\ mm/km \text{ for } 30° < el \le 70° \\ 140\ mm/km \text{ for } el > 70° \end{cases} \quad (66)$$

The corresponding speeds of the ionospheric events were found to be up to 1200 m/s and thus larger than the 750 m/s found in the CONUS region. However, those high speeds were only observed for events with a slope below 50 mm/km. For events with a larger slope the corresponding front speeds remained below 400 m/s and thus well below the values found in CONUS. The potentially resulting errors for a GBAS GAST C user were thus found to be within an acceptable range.

5.3.4 Korean ionospheric threat model

For South Korea Kim et al. [45] made the assessments of the ionospheric gradient assessment. The largest gradient was found on October 11th 2004 with a slope of 138.5 mm/km. In contrast to the previously described models the Korean results did not show larger gradients for higher elevation satellites. In fact the largest gradient was found on a satellite at just about 25° elevation. It is thus proposed that the threat space for Korea is not elevation dependent but flat such that $g \le 160$ mm/km.

5.3.5 Ionospheric threat model discussions

Figure 37 shows a comparison of the threat models for the CONUS region, Germany and Korea. While all regions are located in mid geomagnetic latitudes, the threat model for CONUS shows significantly larger bounds than the ones for Germany and Korea.

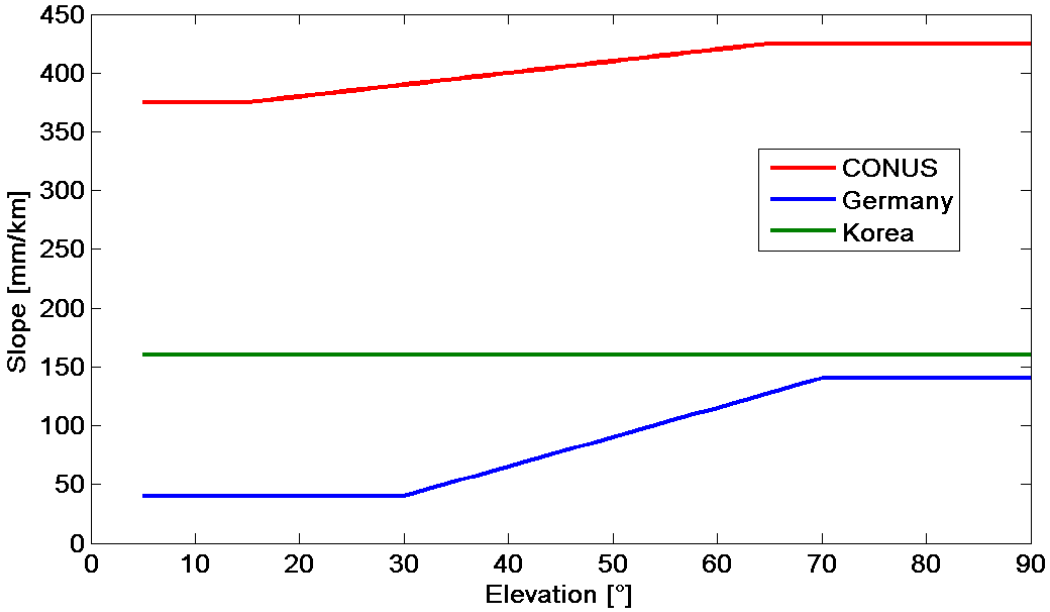

Figure 37 Comparison of ionospheric threat models for CONUS, Germany and Korea

All the events which were shaping the threat spaces were observed in solar cycle 23 after the maximum in the decaying phase in the years 2001-2004. Due to the rare occurrence of significant events the number of data points from which the threat spaces result is very small. In Korea events on 22 and in Germany only 26 days passed the pre-screening and were considered as potentially relevant for the threat space. In the current solar cycle 24 there were to the date of writing no events recorded which exceeded the previously defined boundaries. However, due to the limited knowledge about future ionospheric events and their magnitudes the threat spaces should be continuously reviewed and potentially updated in case new events in the future exceed the bounds of the current models. Such a monitoring is implemented in the US [79].

The ionospheric threat models described here are, however, only based on observations of so-called travelling ionospheric disturbances, i.e. large scale effects typically occurring in auroral to mid-latitudes on a very rare basis. When looking at equatorial regions even steeper gradients can be found. Recent studies on the ionospheric threat space in Brazil found a largest gradient of about 850 mm/km [80]. Gradients in these regions that are significant for GBAS occur much more frequently (on a daily to weekly basis) and are caused by a different phenomenon, called plasma bubble. It is currently unclear whether these phenomena can still be assumed to be non-nominal and how to ensure sufficient protection against these extreme gradients while maintaining an acceptable level of availability. Also studies in the Asia-Pacific region found gradients larger than the ones from CONUS. They have established a threat space assuming gradients up to 600 mm/km [81].

5.4 Monitoring for Ionospheric Gradients in the Ground Subsystem

As described in Section 2.2.3.3 about the integrity in GBAS, several different monitors are included in the GBAS architecture to address different areas of the total ionospheric threat space. Temporal gradients will be detected by either the Code-Carrier-Divergence (CCD) monitor in the ground or airborne subsystem or the airborne Dual Solution Ionospheric Gradient Monitoring Algorithm (DSIGMA). However, there is one scenario where a rising satellite is affected by an ionospheric front which travels in a similar direction and at a similar speed (relating to the speed of the ionospheric pierce points, i.e. the intersection points of the ionosphere with the line of sight vectors between aircraft and satellite) so that it could be potentially undetectable to the CCD and DSIGMA monitors. For that specific situation a non-temporal monitoring scheme for gradients is necessary which can determine if a potentially dangerous ionospheric condition prevails.

5.4.1 The Absolute Ionospheric Gradient Monitor

The method which will be used to detect such an absolute gradient was developed by Khanafseh et al. [32]. It is based on forming double differences of carrier phase measurements between the GBAS reference receivers and pairs of satellites. In a first step, the single difference $\Delta\phi$ is formed:

$$\Delta\phi = \vec{e}^T \vec{x}_b + \Delta\tau + \lambda \cdot \Delta n + \Delta b_I + \varepsilon_{\Delta\phi} \tag{67}$$

In this equation $\vec{e}$ is the unit line of sight vector from the reference receiver to the satellite, $\vec{x}_b$ is the baseline vector between the two reference antennas between which the single difference is formed, $\Delta\tau$ is the differential receiver clock bias between the two reference receivers, λ is the wavelength of the carrier frequency (19 cm for L1), Δn is the single difference of the integer ambiguities of the carrier phase measurements, Δb_I the differential ionospheric delay (the parameter of interest), and $\varepsilon_{\Delta\phi}$ the single difference carrier phase noise. In order to remove the differential receiver clock bias two single differences for two different satellites are used to form a double difference. When rewriting the differential ionospheric delay in terms of a gradient g multiplied with the baseline vector $\mathbf{x}_b$ between the two reference receivers the carrier phase double difference $\Delta^2\phi$ can be written as

$$\Delta^2\phi = \Delta\vec{e}^T \vec{x}_b + \lambda \cdot \Delta^2 n + g \cdot \left|\vec{x}_b\right| + \varepsilon_{\Delta^2\phi} \tag{68}$$

With a precise knowledge of the baseline $\vec{x}_b$ it is possible to subtract the first term on the right hand side of the equation. The remaining parts are now the integer ambiguities, the ionospheric error and the double difference phase noise. Since it is known that the integer ambiguities can only take integer values a test statistic s can be formed as

$$s = \Delta^2\phi - \Delta\vec{e}^T \vec{x}_b - \lambda \cdot \mathrm{round}\left(\frac{\Delta^2\phi - \Delta\vec{e}^T \vec{x}_b}{\lambda}\right) \tag{69}$$

This test statistic measures how well the difference between the double differenced carrier phase measurements and the projection of the line of sight vectors on the baseline agree with a multiple of the integer ambiguity. In an ideal noise and ionospheric free case the test statistic would equal zero. A differential ionospheric error causes the test statistic to increase. Due to the rounding periodic undetectabilities occur at the integer multiples of λ. The double difference phase noise in the measurement impacts the monitor performance significantly. Once the test statistic is small it is impossible to decide if the source of the deviation from zero is due to noise or an ionospheric impact. Experimental validations of the monitor have shown that the carrier phase noise for each antenna has to remain in the range of 3-10 mm, depending on baseline length for the monitor to yield sufficient performance [32]. Note that this value includes corrections for the antenna phase center variations and movements of the antenna due to wind. In order to achieve a false alarm rate low enough to comply with operational requirements, according to the original proposal of the monitor, a prior probability on the order of 10^{-5} of an ionospheric front occurring has to be assumed. After implementation in several test locations and

more extensive testing it was observed, however, that the monitor is very sensitive to what appears to be tropospheric impact. Frequent detections far beyond what's operationally acceptable have been observed [82]. The most recent assumptions taken for closing the validation of the GAST D SARPS assume, that the IGM does not require any prior probability of occurrence and that no significant error can build up before the monitor triggers an alert, even if the time to detect and identify an ionospheric gradient from a tropospheric impact is larger than the time to alert.

5.4.2 Proposal of a New Monitoring Architecture

Another scientific contribution in this work is the new method for ionospheric monitoring proposed here. Is is based on an additional monitoring receiver and is operation in the pseudorange domain. The next sections detail the monitoring principle and the design parameters of the monitor. Thereafter, a review of the assumptions taken in the requirement derivation is given and the use of actual known values for the glide path angle of the approach is suggested. Furthermore, it is proposed to take into account knowledge about the current set of satellites for which corrections are provided, instead of taking the most conservative assumptions. The following Sections 5.4.2.1 to 5.4.2.3 are reproduced from [14]. The notation of variables and references was adjusted to conform to the notation in this thesis.

5.4.2.1 Differential Range Error Monitor

A method for ensuring a limit on the post correction range error in general, "*and mitigating the ionospheric threat in particular, can be based on positioning an additional GNSS receiver at a surveyed location close to the touchdown point of the runway to which approach service is provided. This monitor plays the role of a pseudo user, i.e. it receives and applies GBAS corrections received from the GBAS ground station to correct its own GNSS measurements. The basic idea behind this kind of monitoring is that if an error source, such as an ionospheric disturbance, affects an arriving aircraft in a potentially dangerous way, then the monitor would be affected in a similar way. This is justified since spatial decorrelation between the user and the monitor is minimal, data processing of the raw measurements is the same and the effect does not depend on receiver implementation and airframe characteristics. The smoothed and corrected pseudorange* $\rho_{smt,corr}$ *for each satellite can be described as sum of the theoretical range* r*, an undesired residual range error* E_{range}*, the user clock bias* $c \cdot \Delta t_{user}$ *and a noise term* η *as*

$$\rho_{smt,corr} = r + E_{range} + c \cdot \Delta t_{user} + \eta \tag{70}$$

The theoretical range term can be calculated by precise knowledge of the monitor receiver location and is thus a known parameter. The user clock term is common to all pseudorange measurements. It can therefore be removed from the measurements in the same way as it is done in the calculation of the

pseudorange corrections in the ground systems. This process is called "smoothed clock adjust" and is described in chapter 3.7.1.2.8.3.5 of ED-114A [35]. *After removing the geometrical range portion of* $\rho_{smt,corr}$ *for all satellites in view, the average residual range over all satellites is treated as receiver clock bias. While this is usually not exactly true, it does not influence the performance of the monitor since a range bias which is common to all pseudoranges is mapped into the user clock offset. The remaining parts are the sum of the residual range error and noise. These two cannot be separated and their sum shall be called* E_{test} *, which can be described as*

$$E_{test} = \rho_{smt,corr} - r - \frac{1}{N}\sum_{i=1}^{N} E_{r,i} \tag{71}$$

with N *the number of satellites used. This quantity will be the monitored parameter.*

5.4.2.2 Monitor design

In a next step the threshold value for the monitored parameter, i.e. the largest value for which E_{test} *is still considered nominal, has to be derived. This limit has to fulfill the condition that a possible threat is detected with the required probability of missed detection, and at the same time have a sufficiently low probability of false alarm. The trade-off is shown in the following plot.*

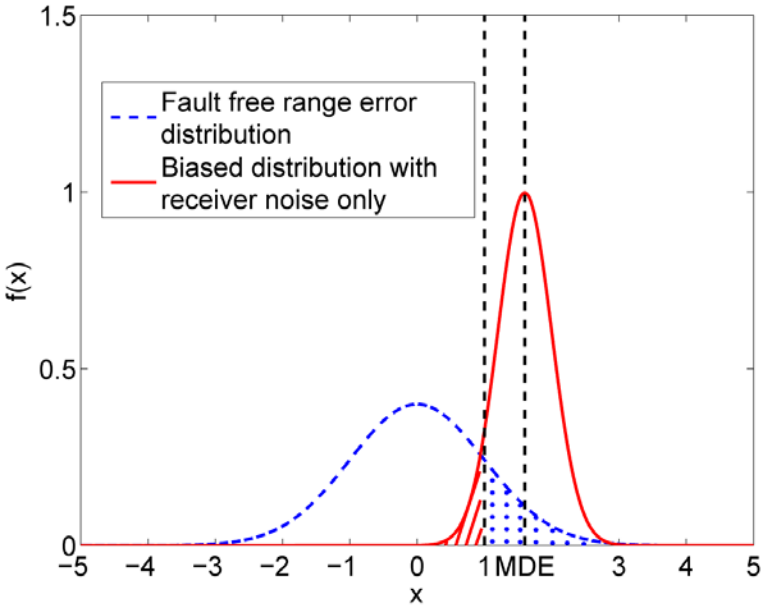

Figure 38 *Example trade-off between probability of missed detection (red shaded) and probability of false alarm (blue dotted). The dashed blue curve shows the expected range error PDF while the red curve shows the expected noise and multipath of the monitoring receiver centered at the minimum detectable error (MDE)*

The properties of this monitor depend on four parameters:

- *The actual expected distribution of the post-corrected range errors is illustrated by the dashed blue curve in the plot above. In the case of the monitor under discussion it is represented by a*

non-biased Gaussian distribution for each pseudorange measurement with standard deviation σ_i *and was described in Equation* (20)*. This model depends on geometry, satellite elevation, altitude difference and distance between the airborne receiver and the GBAS reference point, as well as speed of the aircraft and equipment classification. The parameters used in determining the uncertainty should correspond to the expected error distribution of the signal, i.e. for GAST D using* $\sigma_{gnd,30}$ *from the Type 11 GBAS message* [39] *and a time constant* $\tau = 30$ *seconds to represent the residual noise from the ground system and the appropriate contribution to the ionospheric uncertainty.*

- *The next influencing parameter is the minimum detectable error (MDE) of the monitor where the red curve of the monitor noise probability density function (PDF) is centered. The MDE in this monitoring scheme corresponds to* $E_{r,i,\max}$ *from* (50) *for each satellite. As shown earlier, it depends on airworthiness considerations and is the largest tolerable range error which is attributed to one satellite, such that the aircraft can still operate safely.*
- *Next, the probability of missed detection which is attributed to the monitor has an impact on the overall performance. It is shown as the red shaded area in Figure* 38*. Since in airworthiness considerations the requirement for the fault case is specified for each error with a probability of occurrence greater than* 10^{-9}*, the product of a probability of occurrence and probability of not detecting such a disturbance has to be smaller than* 10^{-9}*.*
- *Finally, the noise and multipath characteristics of the monitoring receiver have a significant impact on the overall performance of the monitor. The lower the noise and multipath characteristics, the larger the monitoring threshold becomes. According to several studies which were performed for evaluation of the GBAS error models, the main concern for ground based receivers is multipath from ground reflections. Hence, strict siting criteria for GBAS reference antennas were developed and multipath limiting antennas are used* [25].

The expected error distribution is defined in Equation (20)*. For the derivation of the MDE from Equation* (50) *we propose to use the actual GPA transmitted in the GBAS message which is typically 3°. When taking a Gaussian noise model for the monitor performance, the detection threshold* E_{monthr} *with the respective* p_{md} *requirement and the standard deviation of the monitor noise* $\sigma_{monitor}$ *can be written as*

$$E_{monthr} = MDE - k_{md} \cdot \sigma_{monitor} \tag{72}$$

with

$$k_{md} = -\Phi^{-1}(0.5 \cdot p_{md}) = -\sqrt{2} erf^{-1}(p_{md} - 1) \tag{73}$$

and $\Phi(x)$ *the standard normal distribution. According to Equation* (73) *the corresponding missed detection multiplier for* $p_{md} = 10^{-9}$ *is* $k_{md} = 6.1$*. The monitoring condition thus becomes*

$$E_{monthr} < \frac{E_{v,iono,\max}}{s_{vert,i}} - 6.1 \cdot \sigma_{monitor,i} \tag{74}$$

for each satellite i*. When allowing some credit to be taken for the fact that those events are very rare, a prior probability* p_{iono} *can be defined such that instead of requiring a missed detection probability* $p_{md} = 10^{-9}$*, only the product of prior probability for an ionospheric event and the probability of missed detection has to meet the requirement* $p_{md} \cdot p_{iono} = 10^{-9}$*. If a meaningful prior probability can be established, e.g. by external monitoring of the state of the ionosphere, we propose to use it in order to achieve better false alarm properties.*

For the derivation of the monitoring threshold we propose that the projection factors $s_{vert,i}$ *in* (74) *should be calculated for each satellite individually as described in the previous section. The resulting largest* $s_{vert,i}$ *at each epoch will always be smaller or equal to 4 which leads to relaxed monitoring requirements since* E_{monthr} *increases with decreasing* $s_{vert,i}$*.*

For $\sigma_{monitor}$ *we suggest to use a model which conforms to the Ground Accuracy Designator (GAD) C requirement intended for GAST-D operations. We use the same model as used in* [38] *which describes the noise as*

$$\sigma_{noise} = \min(0.24\text{m},\ 0.15\text{m} + 0.84\text{m} \cdot e^{-\theta/15.8^\circ}) \tag{75}$$

It is represented by an elevation dependent function which remains constant for satellite elevation angles below 35° to reflect the characteristics of multipath limiting antennas (MLAs) and the siting criteria for GBAS. Although the noise restrictions required for this kind of monitoring are the most stringent ones in terms of GBAS Ground Facility Classification, meeting this requirement has been shown to be possible by Dautermann [83] *with choke-ring antennas and standard receivers in a non-optimal environment which does not meet the GBAS siting criteria.*

5.4.2.3 Monitor performance

In this section an analysis of the different parameters influencing the monitor performance is carried out. Figure 39 *shows the minimum gradient which will be detected by this monitor. It is a function of the MDE of the monitor and the distance* $d_{monitor}$ *between the GBAS reference point and the location of the monitoring receiver. The minimum slope* $g_{\min}$ *of a gradient which has to be detected can then be written as*

$$g_{\min} = \frac{MDE}{d_{monitor}} = \frac{E_{v,iono,\max}}{s_{vert,i}} \cdot \frac{1}{d_{monitor}} \tag{76}$$

with the same notation as in the previous equations. The $s_{vert,i}$ *are calculated according to Equation* (18) *based on a standard GBAS weighting and assuming an aircraft speed of 70 m/s, which is a typical*

approach speed. Out of all satellites in view the $s_{vert,i}$ *for the most limiting satellite, i.e. the satellite with the largest expected test statistic, is taken for a GBAS located at Braunschweig/Wolfsburg airport in northern Germany. The monitor receiver is assumed to be located 5 km from the GBAS reference point in runway direction towards the east. Two different values for the GPA are plotted to show the possible relaxations of the monitoring requirement in comparison to the current 300 mm/km limit. The larger GPA relaxes the constraint on the largest tolerable vertical error as described in Equation* (44) *and thus enlarges the tolerable slope of an ionospheric gradient.*

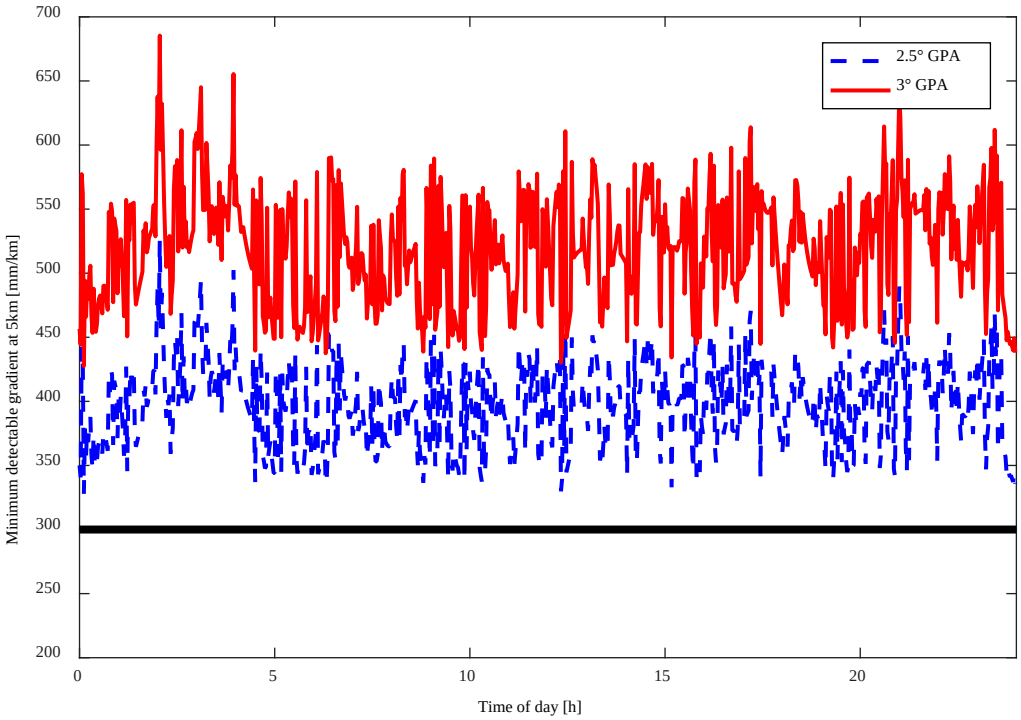

Figure 39 *Minimum size of gradients which will be detected by a monitor located 5km away from the GBAS reference point. The dashed blue curve shows the values for a 2.5° GPA while the red curve shows the required detection for a standard 3° GPA. The black line shows the current requirement.*

The minimum slope of a gradient which needs to be detected considering a 2.5° GPA increases to values typically varying between 350 and 450 mm/km over a day, while at a 3° GPA only gradients as large as 450 to 550 mm/km are serious enough to create a potentially dangerous vertical error. At all times the monitoring thresholds are significantly larger than the currently required 300 mm/km.

Figure 40 *shows the corresponding monitoring threshold over one day which was described in Equation* (74) *with a missed detection probability* $p_{md} = 10^{-9}$. *For comparison two curves are plotted showing again the different monitoring thresholds for a 2.5° or 3.0° GPA. The monitor threshold over the day typically varies between 0.5 m and 1 m for the 2.5° GPA and between 1 m and 1.6 m for the 3° GPA. The peak shortly before 14 h represents a situation where for a short time the largest possible* $s_{vert,i}$ *is as small as 2.57 and the corresponding monitor threshold increases to almost 2 m.*

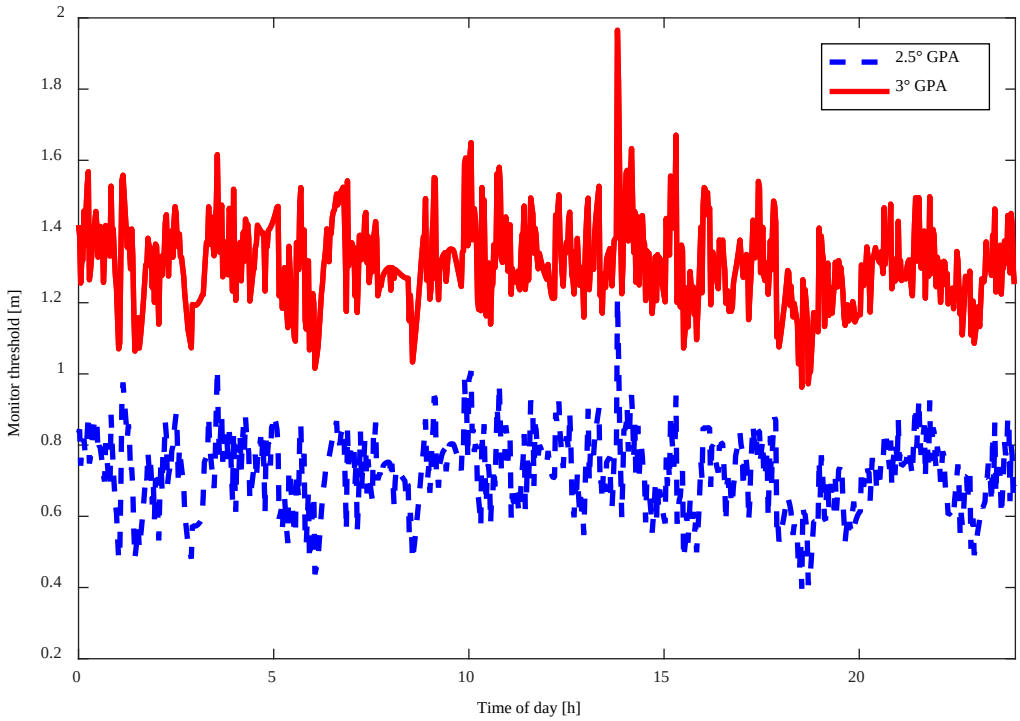

Figure 40 *Monitor thresholds for Braunschweig airport over one day depending on the glide path angle of the approach for the most limiting satellite in view.*

It can be seen that the higher glide path angle increases the monitor threshold by a factor of roughly 1.6 and thus reduces the false alarm probability of the system accordingly. It is therefore very beneficial to consider the actual GPA for an airport, rather than a general worst approach angle for precision approaches. The false alarm probability is another important parameter since the rate of false alarms impacts the availability and continuity of the system. It is represented as the dotted blue surface in Figure 38 *and can be modeled as*

$$p_{fa} = 2 \cdot \Phi\left(\frac{-E_{monthr}}{\sigma_i}\right) \tag{77}$$

with the standard normal distribution Φ*, the monitoring threshold* E_{monthr} *from Equation* (74) *and the expected standard deviation of the smoothed, corrected pseudorange* σ_i *for the most critical satellite* i*. Note that Figure* 38 *only shows the one-sided probability. The factor 2 in Equation* (77) *takes into account the fact that the errors can be positive or negative. Figure* 41 *shows the false alarm probability over a day corresponding to the monitoring thresholds from Figure* 40 *for a 3° GPA.*

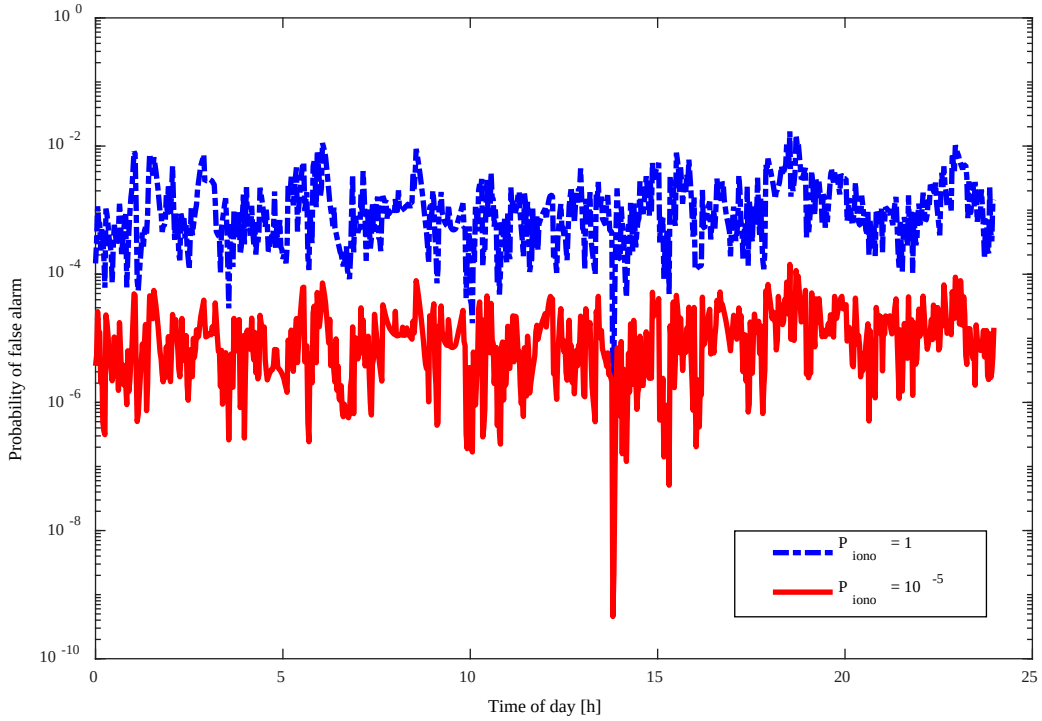

Figure 41 *Probability of false alarm depending on prior probability P_{iono} of occurrence of an ionospheric disturbance. Both results assume a 3° GPA for the approach.*

The dashed blue curve shows the case if no prior probability for the occurrence of an ionospheric disturbance is defined. In this case the false alarm probability mostly stays in the range of 10^{-2} to 10^{-5}. For an operational system these values are large, despite the fact that flagging one satellite would not necessarily limit the availability of the whole GBAS, since usually there are between 6 and 12 satellites available for navigation. However, if some credit is taken for the fact that these storms happen very rarely, performance of this monitor improves significantly. Previous work on this issue, such as [32] *or* [33] *used a value of 10^{-5} for the assumed probability of occurrence. This limits the required probability of missed detection to just 10^{-4} and reduces the k-factor in Equation* (72) *from 6.1 to 3.7 and thus relaxes the monitoring problem. The results for the false alarm probability assuming this prior probability for an ionospheric disturbance is shown in red in Figure* 41. *It decreases down to values in the range of 10^{-4} to 10^{-6}. However, a standardized way of determining such a probability has not yet been developed and needs to be investigated. Due to the more frequent observation of ionospheric storms, scintillations and plasma bubbles in the high and low latitudes as opposed to the mid-latitudes, such a probability should be defined locally together with the ionospheric threat model or determined by external information, such as ionospheric parameters from a space based augmentation system (SBAS).*

The results shown above are an example for performance at a certain location. However, the monitoring thresholds and the associated false alarm probabilities do not change substantially in different locations around the earth and at different latitudes. This is a result of the selection of the worst possi-

ble geometry at any location for the derivation of a conservative monitor threshold. Figure 42 *shows the simulated thresholds over one day for three selected airports in different regions.*

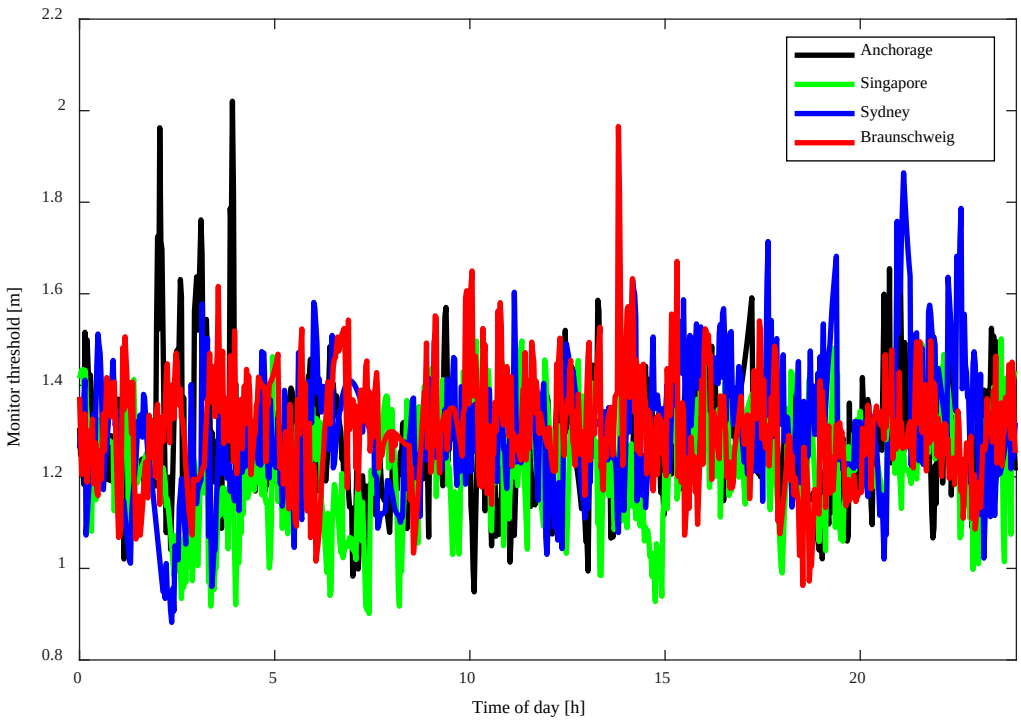

Figure 42 *Monitor thresholds for the most limiting satellite in view over one day at different latitudes. Anchorage as example for a polar region airport (Latitude 61°N), Singapore for an equatorial airport (1°N) and Sydney as example for mid-latitude (33°S) compared to Braunschweig assuming a 3° GPA*

Anchorage is located at a northern latitude of 61°, Singapore is located very close to the equator at 1° North and Sydney is located at 33°S in the equatorial to mid-latitude region. Together with Braunschweig (at 52°N) those airports represent the typical range in which GBAS stations are expected to be located. The monitor thresholds tend to be the lowest in Singapore (green curve). The times when the monitoring threshold decreases below 1 m for the most critical satellite correspond to epochs when many satellites are visible (13 or 14). At these epochs it is possible to select subsets which create larger values for s_{vert} *than at times when there are fewer satellites available. Sydney shows a monitoring threshold very similar to that of Braunschweig. Only for one short period of about 20 minutes around 2 h 30 min it drops below a value of 1 m. During this time there are also 13 satellites visible while at most other epochs the number is mostly between 12 and 8. For Anchorage there are four spikes visible between 2 h and 4 h where the threshold becomes very large. At these epochs there are 11, 9, 7 and 10 satellites visible while most of the time there are at least 10 satellites available, sometimes up to 14. In a similar way as could be observed at the other locations, a smaller number of available satellites generally increases the monitoring threshold. However, the effect is not as visible as in the other example sites because due the location far up north more satellite subsets are excluded in the geometry screening process.*" [14]

5.4.2.4 Discussion of the monitor

The proposed method requires either an additional reference receiver or at least one of the nominal reference receivers placed far away from the others. While current GBAS layouts try to keep the locations of the receivers rather close together for operational and maintenance reasons such a reference receiver layout may be considered in the future if the benefits in ionospheric monitoring outweigh the operational difficulties and help bringing the availability to operationally acceptable levels.

Taking the actual glide path angle instead of a conservative 2.5° assumption already brings a significant benefit and reduces the unnecessary conservatism in the monitor. When it comes to the definition of a monitoring threshold and the projection of the pseudorange into the position domain plays again an important role. As the ground station has to support all aircraft without knowing which satellites are actually used it has to be conservative and assume a value for $s_{vert,i}$ that is surely not exceeded by any aircraft. By evaluating all subsets it is possible to take reduce the conservatism and derive a worst case value for all possible subsets. This facilitates the monitoring task significantly, however, it is still a very conservative approach for most aircraft as they will typically use a better geometry than the worst case.

Credit for the actually used geometry and thus projection factor can only be taken at the aircraft where the receiver is aware of the satellites in use. The concept for single frequency GBAS is standardized but no decision is taken how future GBAS service types using signals from two frequencies and multiple constellations will look like. There it is possible to move the task of ionospheric monitoring to the airborne system and thus leverage the knowledge about the actual geometry in use. Such a monitoring scheme is developed and presented in the following section.

The proposed ionospheric monitor would also form part of the mitigation strategy of the ionospheric threat and, in order to become operational, would have to undergo a more thorough validation, especially about the mitigation of the applicable threat space together with all other monitors.

5.5 AIRBORNE MONITORING FOR IONOSPHERIC GRADIENTS

This section constitutes another original contribution of this work by expanding the concept of using available information for ionospheric monitoring and describing how this task may be achieved in future dual frequency GBAS. The method was first presented in [77] and expanded in [78] and [15] on which this section is based (numbering and references adjusted to conform with the notation in this work).

In Section 5.4 a method for monitoring for ionospheric gradients in the GBAS ground station and its potential improvement considering knowledge about the available ranging sources was presented. This method was specifically designed to support GAST D users, i.e. single frequency GPS only users. In this service type *"a significant number of different monitors in the ground and airborne systems may result in limited availability due to frequent trips, especially in equatorial and polar regions prone to high ionospheric activity. A challenge for GNSS users are ionospheric scintillations. This effect leads to degraded signal tracking quality in the receiver or loss of lock to several satellites and thus results in degraded satellite geometries. Use of signals from multiple GNSS constellations will provide significantly increased robustness against this kind of events due to the large number of satellites and thus low sensitivity to the loss of individual signals"* [15]. The previously described threat of ionospheric gradients *"can be addressed by means of dual frequency positioning, eliminating the ionospheric delay (to a first order which is sufficient for GBAS operations) in GNSS measurements. GPS introduced signals on a second frequency usable for safety of life applications with the latest generation of satellites (Block IIF). Galileo provides those signals on all its satellites from the beginning. Combining measurements from two frequencies, however, comes at the cost of significantly increasing the residual noise in the position solution due to the combination of the two noisy pseudorange measurements on L1/E1 and L5/E5a* [52]. *It is thus a likely scenario that even in future GBAS with dual frequency capability positioning in the nominal case will be based on single frequency measurements* [53]. *In that case an effective monitoring for ionospheric gradients is necessary. [..]*

Assuming that the ground station provides corrections for two frequencies and the aircraft receiver is also able to track signals on two frequencies an effective ionospheric monitoring is possible. The proposed method marks a fundamental change in where the monitoring is to be performed. While in GAST C it is the sole responsibility of the ground station to bound the errors at the airborne receiver the iono monitoring task is shared between ground and airborne GBAS subsystems in GAST D. In the method proposed here it is the sole responsibility of the airborne systems to monitor for ionospheric gradients. This allows for a more realistic error bounding because the current navigation performance (and aircraft performance) can be exploited and less conservative assumptions have to be made. [..]

5.5.1 Concept of the Airborne Ionospheric Monitor

The basic idea of the proposed monitoring is to simply compare the ionospheric delay estimate at the ground station with an ionospheric delay estimate at the aircraft. In the airborne system it is possible to directly estimate the experienced ionospheric delay $\tilde{I}_{air,i}$ *experienced on* $\hat{\rho}_{L1,i}$ *based on the smoothed pseudorange measurements* $\hat{\rho}_{f,i}$ *on frequency f and satellite i as*" [15]

$$\tilde{I}_{air,i} = \frac{f_{L5}^2}{f_{L1}^2 - f_{L5}^2}(\hat{\rho}_{L5,i} - \hat{\rho}_{L1,i}) \tag{78}$$

The ionospheric delay experienced at the ground station cannot be directly computed from the received corrections due to the way the corrections are generated. The smooth clock adjust process (previously described in Equation (4) in Section 2.2.2.2 removes all delays common to all pseudorange measurements from one reference receiver, notably also the common ionospheric delay. "*Nevertheless, a pseudo-ionospheric delay estimate* $\tilde{I}_{PRC,i}$ *for each satellite i can be formed from the GBAS corrections in the same way as when estimating the actual ionospheric delay on the L1 frequency from pseudorange measurements replacing the measured pseudorange with the received corrections from the ground station:*

$$\tilde{I}_{PRC,i} = \frac{f_{L5}^2}{f_{L1}^2 - f_{L5}^2} \cdot [(PRC_{L5,i} + \Delta t \cdot RRC_{L5,i}) - (PRC_{L1,i} + \Delta t \cdot RRC_{L1,i})] \tag{79}$$

In the same way as the applied correction would contain the pseudorange correction PRC and the range rate correction RRC multiplied with the time difference between the current time of measurement and the time of generation of the corrections Δt*, these quantities are used also in the monitor. The indices L1 and L5 indicate the frequency for which the corrections were formed and f the central frequency of the respective signals.*

In a next step these two quantities have to be made comparable. For that reason we remove the average of all N airborne iono delay estimates [for which corrections are available] *per constellation to obtain a pseudo airborne ionospheric delay measure* $I_{air,i}$ *which is given by*

$$I_{air,i} = \tilde{I}_{air,i} - \frac{1}{N}\sum_{i=1}^{N} \tilde{I}_{air,i} \tag{80}$$

In order to account for the fact that the airborne system may use only a subset of the satellites to which the ground system provides corrections we repeat this process also with the pseudo delay estimates from the ground station using only the set of satellites used in the airborne pseudo iono delay estimate. Similar to Equation (80)*, the pseudo iono delay from the corrections is then*

$$I_{PRC,i} = \tilde{I}_{PRC,i} - \frac{1}{N}\sum_{i=1}^{N} \tilde{I}_{PRC,i} \tag{81}$$

These two estimates are now comparable and can be used to form a test statistic $I_{test,i}$ as

$$I_{test,i} = \left| I_{air,i} + I_{PRC,i} \right| \tag{82}$$

Note that the two quantities are added (a more intuitive guess would be to subtract them and compare to zero) due to the fact that the pseudo delay estimate from the corrections would have opposite sign from the value derived from the pseudorange measurements. In the nominal case (i.e. without a significant ionospheric gradient) the test statistic is small and would mostly consist of noise. With increasing decorrelation of the ionospheric delay experienced at the ground station and the airborne user this quantity would increase.

The previously described test statistic is only valid if the navigation is based on signals in the L1/E1 frequency band. It is, however, also possible to support positioning based on L5/E5a which may under certain circumstances be a desired mode. In that case a user would experience an ionospheric delay on each measurement that is $\beta = \frac{f_{L1}^2}{f_{L5}^2} \approx 1.8$ times larger than on L1/E1. Additionally, the monitoring threshold will be even tighter in that case. Thus, navigating based on L5/E5a is significantly more challenging in terms of integrity and is not considered further in this study.

5.5.2 Monitoring threshold

After having defined a test statistic as measure for a difference in ionospheric delay a threshold needs to be defined above which it is unsafe to use the signals from a certain satellite or set of satellites. A meaningful derivation of a monitoring threshold comes from the operation, namely the requirements for a safe landing. For a landing to be considered safe, the aircraft has to touch down inside the so-called "touchdown box", i.e. not less than 200 ft and not more than 2700 ft behind the runway threshold and not less than 5 ft from either runway edge with a probability of not less than $1\text{-}10^{-6}$ in the nominal case. Two more cases are defined that also have to be considered, namely the limit and the malfunction case. In the limit case one parameter is kept at is most adverse value while all other influencing parameters vary according to their nominal distributions. In the malfunction case an undetected error occurs. In both cases the aircraft has to land within the touchdown box, where the land long limit is extended to 3000 ft behind the runway threshold.

These requirements are defined at aircraft level and thus only part of the total error budget can be attributed to the navigation system. The other main question in automatic landings, apart from how well the navigation system can determine the position of the aircraft, is how well the autopilot can land the aircraft on a desired spot. As the landing performance depends on both systems there is a possibility to trade off autopilot and navigation system performance. Note that this tradeoff is, however, only possible if the monitoring for disturbances occurs onboard the aircraft. In the case of the current service types the ground station plays an important role in mitigating part of the threat space.

Thus, it is not possible to take actual aircraft performance into account in those systems as the ground station has to support all aircraft types.

In [78] *we showed the derivation of the monitoring threshold considering a single satellite being affected by an ionospheric gradient. This was done by starting from the requirement that the aircraft has to land within the touchdown box and the land short case (i.e. landing not too close to the runway threshold) is considered to be the driving constraint. The along track error is a function of the nominal touchdown point* $NTDP$ *, the nominal flight technical error* FTE *(i.e. how well the autopilot can place the aircraft onto the desired landing spot), the nominal navigation system error* NSE *(nominal errors due to noise, multipath, nominal ionosphere and troposphere decorrelation) and an additional error caused by an undetected error in form of a bias, e.g. cause by an ionospheric gradient. It is assumed that a vertical position error* E_v *maps into an along track position error* E_{atrk} *at touchdown by the simple geometric relation*

$$E_{atrk} = \frac{E_v}{\tan(GPA)} \tag{83}$$

where GPA *is the glide path angle (normally 3°). In the malfunction case the aircraft has to land in the touchdown box with complete certainty. Taking the nominal* NSE *and* FTE *as Gaussian distributed random variables could of course never satisfy this condition. In that case they are fixed at their* 95^{th} *percentiles* [62]. *The requirement for the land short case can now be formulated as*

$$200 \text{ ft} \leq NTDP - \frac{NSE_{vert,ff,95\%} + E_{v,iono}}{\tan(GPA)} - FTE_{ff,95\%} \tag{84}$$

Where $NSE_{vert,ff,95\%}$ *and* $FTE_{ff,95\%}$ *are the nominal navigation and flight technical errors at the* 95^{th} *percentile of their Gaussian distributions. This is illustrated in Figure* 43

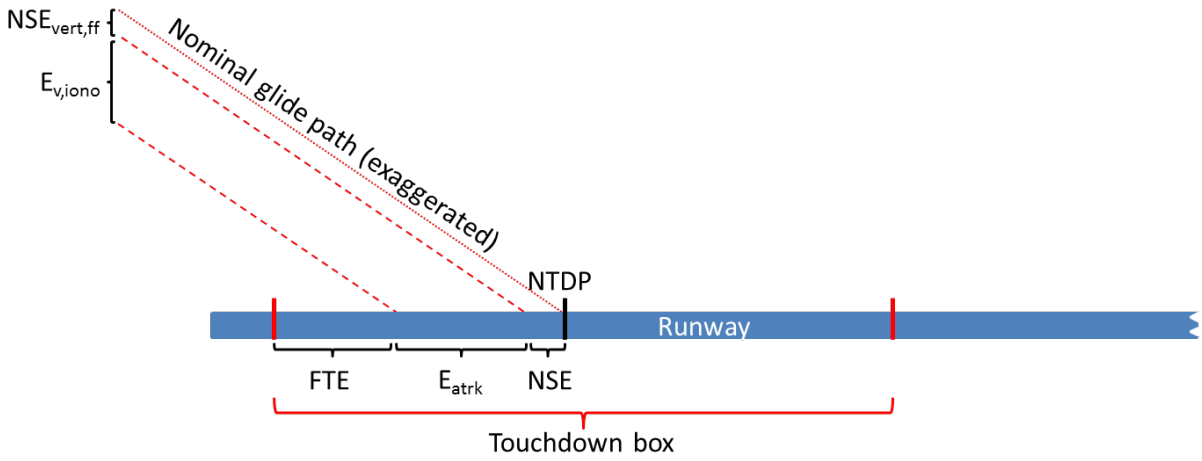

Figure 43 *Derivation of the largest allowable vertical error* $E_{v,iono}$ *and illustration of the contributing error sources for automatic landings.*

The $NSE_{vert,ff,95\%}$ is a vertical position error and can be derived from the protection level equation [38] *as*

$$\sigma_{NSE,vert,ff} = \frac{VPL}{K_{ffmd}} = \frac{VPL}{5.81} \tag{85}$$

where K_{ffmd} is the fault free missed detection multiplier for the integrity risk of $2 \cdot 10^{-7}$ allocated to the protection level. Note that the VPL is a bound for the instantaneous nominal vertical position error and depends on the satellite geometry, as well as the expected ranging performance for the satellites. At all times it needs to remain below the so-called vertical alert limit (VAL) that is limited by a value of 10 m for the final approach and landing [4].

The nominal touchdown point is usually considered to be located 1290 ft behind the runway threshold and $\sigma_{FTE} = 180\,ft$ is assumed to be a conservative value for all aircraft using [13]. *With all those assumptions it is now possible to derive a limit on the largest vertical position error $E_{v,iono}$ due to an ionospheric anomaly from Equation* (84). *Assuming VPL=VAL=10*m *and GPA=3° the resulting condition would be $E_v \leq 8.4$*m. *Taking a less conservative value of VPL=5*m *and leaving all other parameters constant, the resulting condition would already be relaxed to $E_v \leq 10.1$*m *and for a realistic value for a multi-constellation case of VPL=2.5*m *it would be further relaxed to $E_v \leq 10.9$*m .

Now this limit in the position domain needs to be translated into a limit in the pseudorange domain since the previously described test statistic is calculated per satellite. The pseudorange measurements ρ and the user position and clock estimate x are related by the weighted pseudoinverse **S** *of the geometry matrix* [previously described in Section 2.2.3.2] *such that*

$$x = \mathbf{S} \cdot \rho \tag{86}$$

A weighting matrix W containing the fault-free variances of the expected residual pseudorange errors is used to give lower weight to satellites with larger expected uncertainties. The **S***-matrix is defined as*

$$\mathbf{S} = (\mathbf{G}^{\mathrm{T}}\mathbf{W}\mathbf{G})^{-1}\mathbf{G}^{\mathrm{T}}\mathbf{W} \tag{87}$$

and the contribution of a single satellite i to the position estimate vertical to the approach track is given by

$$s_{vert,i} = s_{3,i} + s_{1,i} \cdot \tan(GPA) \tag{88}$$

where $s_{k,i}$ denotes the entry in the k^{th} row and i^{th} column of the **S***-matrix.*

In the case of a single satellite affected by an undetected ionospheric gradient a limit on the pseudorange error $E_{r,iono,i}$ on that particular satellite would thus be

$$E_{r,iono,i} \leq \frac{E_{v,iono}}{\left| s_{vert,i} \right|} \tag{89}$$

It is interesting to note that based on this equation a pseudorange error may become arbitrarily large as long as the weight assigned to that satellite through the $s_{vert,i}$ *is small enough. A typical behavior of values for* $s_{vert,i}$ *as function of the elevation of the satellite is shown in Figure* 44 *where we simulated the geometry of a combined GPS and Galileo constellation with 31 and 27 satellites, respectively, during our test flight described later [..]. At about 45° elevation the* s_{vert} *of two satellites become almost zero, leading to very large pseudorange error limits.*

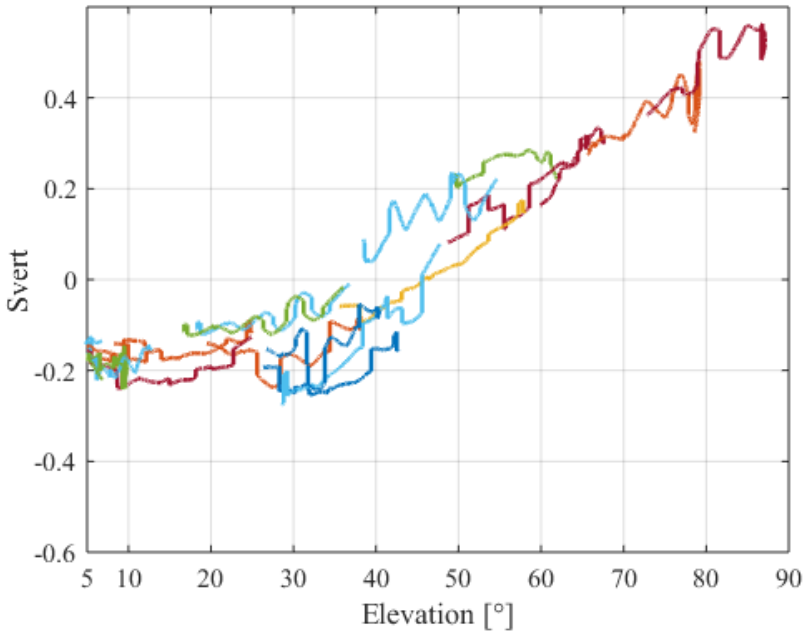

Figure 44 *S_vert as a function of the elevation of the satellites for a future combined GPS and Galileo constellation with 31 and 27 satellites, respectively*

With a missed detection probability of 10^{-9} *attributed to the monitor and assuming that the noise in the test statistic follows a Gaussian distribution the monitoring condition is given as*

$$I_{test,i} \le \frac{E_{v,iono}}{\left|s_{vert,i}\right|} - 6.1 \cdot \sigma_{monitor,i} \tag{90}$$

The test statistic $I_{test,i}$ *as defined in Equation* (82) *contains the airborne measurement noise* $\sigma_{air,f}$ *from the smoothed pseudorange measurements on both frequencies* f *, and in addition the noise contained in the pseudorange corrections* $\sigma_{gnd,f}$ *for both frequencies. The noise in the proposed monitor can thus be described as*

$$\sigma_{monitor,i} = \frac{f_{L5}^2}{f_{L1}^2 - f_{L5}^2} \sqrt{\sigma_{gnd,L1}^2 + \sigma_{gnd,L5}^2 + \sigma_{air,L1}^2 + \sigma_{air,L5}^2} \tag{91}$$

In [78] *we showed that this monitoring condition can be fulfilled rather easily. Even with the minimum number of just 5 satellites and noise from our experimental system that is expected to be larger than*

that of an operational GBAS the monitoring was possible and did not cause false alarms due to very low monitoring thresholds.

Unfortunately, assuming only a single affected satellite may not sufficiently bound potential errors caused by ionospheric disturbances. It is possible that more than one satellite could be affected by an ionospheric front. For that reason a look on the scenario that two satellites are affected simultaneously is taken. In this case the error from both affected satellites would project from the pseudorange into the position domain according to Equation (86)*. A limit on the sum of both pseudorange errors of the affected satellites i and k based on Equation* (89) *then becomes*

$$E_{r,iono,i} + E_{r,iono,k} \leq \frac{E_{v,iono}}{\left| s_{vert,i} + s_{vert,k} \right|} \tag{92}$$

Finally also the noise of both estimates needs to be considered and the monitoring condition thus can get much more stringent:

$$I_{test,i} + I_{test,k} \leq \frac{E_{v,iono}}{\left| s_{vert,i} + s_{vert,k} \right|} - 6.1 \cdot \sqrt{\sigma^2_{monitor,i} + \sigma^2_{monitor,k}} \tag{93}$$

Note that in this case the test statistic can increase if the pseudo iono estimates on the two satellites have the same sign. At the same time the noise contribution in the monitoring condition increases. The sum of the s_{vert} can either increase or decrease depending on the sign of the values as shown previously in Figure 44*. The worst case would occur when the satellites with the two largest s_{vert} with the same sign have constructively adding pseudo iono delays.*

This monitoring concept can of course also be expanded to assuming more affected satellites. A generalized monitoring condition for N affected satellites would then be

$$\sum_{i=1}^{N} I_{test,i} \leq \frac{E_{v,iono}}{\left| \sum_{i=1}^{N} s_{vert,i} \right|} - 6.1 \cdot \sqrt{\sum_{i=1}^{N} \sigma^2_{monitor,i}} \tag{94}$$

Note that the more affected satellites are considered in the monitoring, the more challenging it becomes. However, on the other hand, the more satellites are assumed to be affected by a gradient and are not excluded from the position solution, the less likely the scenario becomes. In Equation (94) *no credit is taken for the low prior probability of such a scenario occurring but this might be considered for the future. Furthermore, the monitoring is conservative in the way that it does not consider the actual separation of satellites in terms of azimuth angle. In the case of an ionospheric front, only satellites in certain azimuth regions would be affected, however we consider only the s_{vert} values, irrespective of the azimuth.*

In the following section an exemplary evaluation during one of our flight trials is presented. The contributing factors are analyzed more in detail with the example at hand to illustrate the effects inherent to this monitoring scheme.

5.5.3 Evaluation in Flight Trials

The German Aerospace Center (DLR) is operating an experimental GBAS station consisting of four reference receivers tracking GPS and Galileo L1/E1 and L5/E5a signals. It is located at the Braunschweig research airport in northern Germany. The layout of the reference receiver locations is shown in Figure 45.

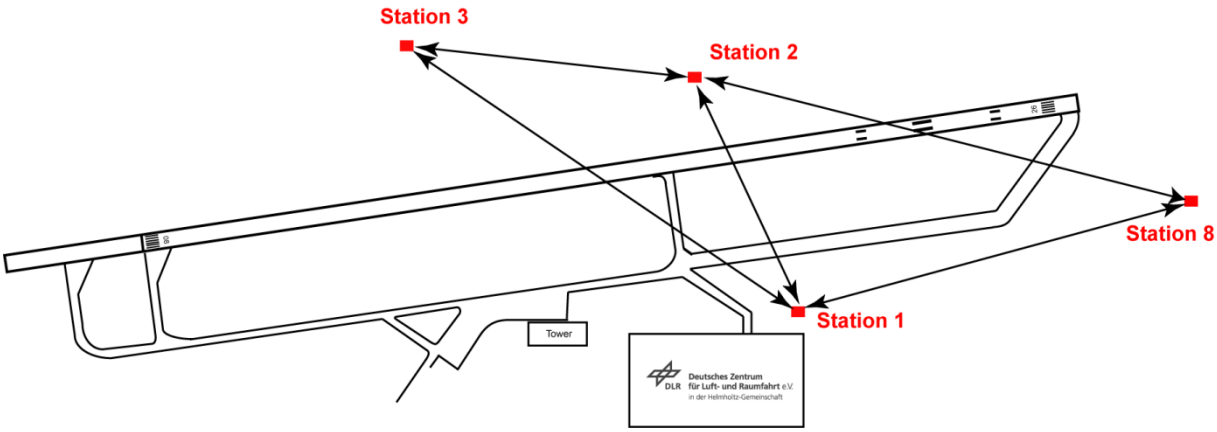

Figure 45 Layout of the GBAS reference stations at Braunschweig Airport as used during the flight trials

In November 2016 a flight test with a Dornier DO-228 aircraft (a twin-engine turboprop aircraft) was performed in the vicinity of Braunschweig. The flight lasted for about two hours and consisted of about one hour of maneuvering and flying the aircraft at different bank angles, followed by one hour of five approaches and extended traffic patterns. The ground track of the flight is shown in Figure 46. One of the purposes of the test was to evaluate the signal tracking performance in steep turns with bank angles of up to 60°. The data of that part of the flights shows frequent loss of lock events and very limited continuously tracked signals. That first part (shown in black in Figure 46) is therefore omitted in the following evaluations. Only the second half of the flight where normal maneuvering was performed (shown in green) is used.

Figure 47 shows a skyplot of the GPS Block IIF and Galileo satellites as observed during the test flight. There were 11 different satellites visible, at most 10 of them at the same time. This number is somewhat typical for a single full constellation. With a fully deployed Galileo constellation and all GPS satellites providing also L5 signals in the future, the number of visible satellites in Braunschweig would vary between 18 and 21.

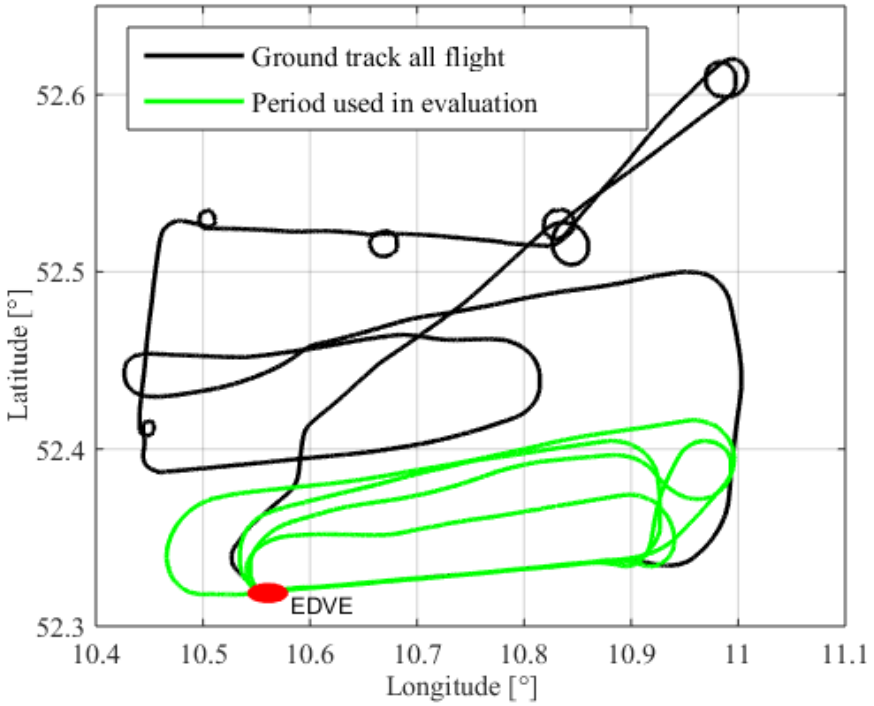

Figure 46 *Ground track of the test flight around Braunschweig (ICAO identifier EDVE). The part used for the evaluation is shown in green*

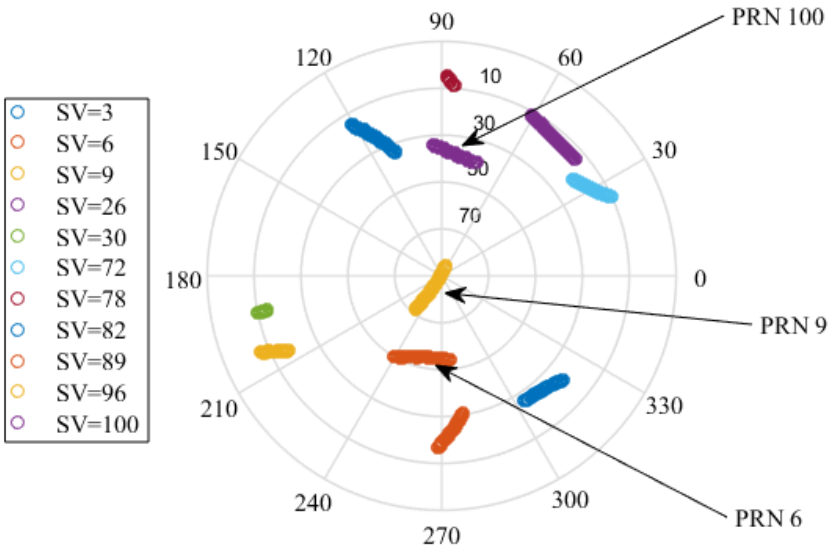

Figure 47 *Skyplot of the combined GPS (SV 1-32) / Galileo (SV 71-100) constellation providing L1/E1 and L5/E5a signals as observed during the flight trial*

We start the evaluations with assumptions on the σ_{air} *and* σ_{gnd} *which were experimentally derived from our ground and airborne systems for each of the two frequencies and each of the two constellations individually as previously presented in* [52], [84] *and* [53]. *For the whole flight and all satellites in the single affected satellite case the test statistic (the monitoring condition for* $i = 1$ *in Equation* (94) *) is fulfilled, except one short instance that will be discussed later.*

Figure 48 *shows the number of used satellites in subplot a) and the test statistics with the corresponding monitoring thresholds for L1/E1-based navigation for the three selected satellites marked in the skyplot in Figure* 47. *The drops in the number of satellites occur during turns where tracking of low elevation satellites is lost due to signal blockage by parts of the aircraft. Subplot b) shows the results for PRN 6, a satellite at elevations between 50° and 55°. In the particular geometry this satellite had a very small* s_{vert} *leading to an extremely large monitoring threshold mostly in the range of 100 m to 200 m (note the different scale of the y-axis for this subplot). As the satellite plays almost no role for the determination of the vertical position a potential error could become very large and not affect the user much. The threshold decreases to a value of about 3.7 m shortly before 16h at the short period of time when the number of used satellites went down to 7. At that moment PRN 6 became a rather important satellite leading to a small threshold. The sharp drop in the monitoring threshold for all satellites at that time indicates a rather strong dependence on the number of satellites available in case that number is small. If many satellites are available, losing one or two of them for the position solution does not have a large impact anymore. Shortly before 15.8h and at 16h there are small spikes in the test statistic. They appear small due to the large scale of the y-axis but reach values of up to 7 m. These spikes result from excessive multipath or a cycle slip and were detected by the onboard GBAS monitor. However, for illustration purposes we did not exclude the data from the plot. Due to the average removal in the test statistic as described in Equation* (80) *an effect on one satellite would be visible in the test statistic of all other satellites as well.*

This is the case as can be seen in subplot c) showing the results for PRN 9 where spikes occur at the same times. PRN 9 is a very high elevation satellite between 72° and almost 90° elevation. At all times it is the satellite with the highest elevation. From a geometrical perspective PRN 9 is a very important satellite and thus has a rather large s_{vert} *According to Equation* (89) *this results in a small tolerable pseudorange error for that satellite and thus a low monitoring threshold throughout the flight. Due to the average removal in forming the test statistic the threshold for that satellite is exceeded twice just before 16h, however, that effect by a cycle slip would have been excluded by other monitors and is again in the data just for illustration purposes.*

The results for PRN 100, a Galileo satellite, are shown in subplot d). Note that the average removal is performed per constellation and thus the spikes from subplots b) and c) do not occur in subplot d). The elevation of the satellite varies between 35° and 40°. While it has quite a large weight in the beginning it quickly becomes smaller and thus the monitoring threshold increases fast to larger values.

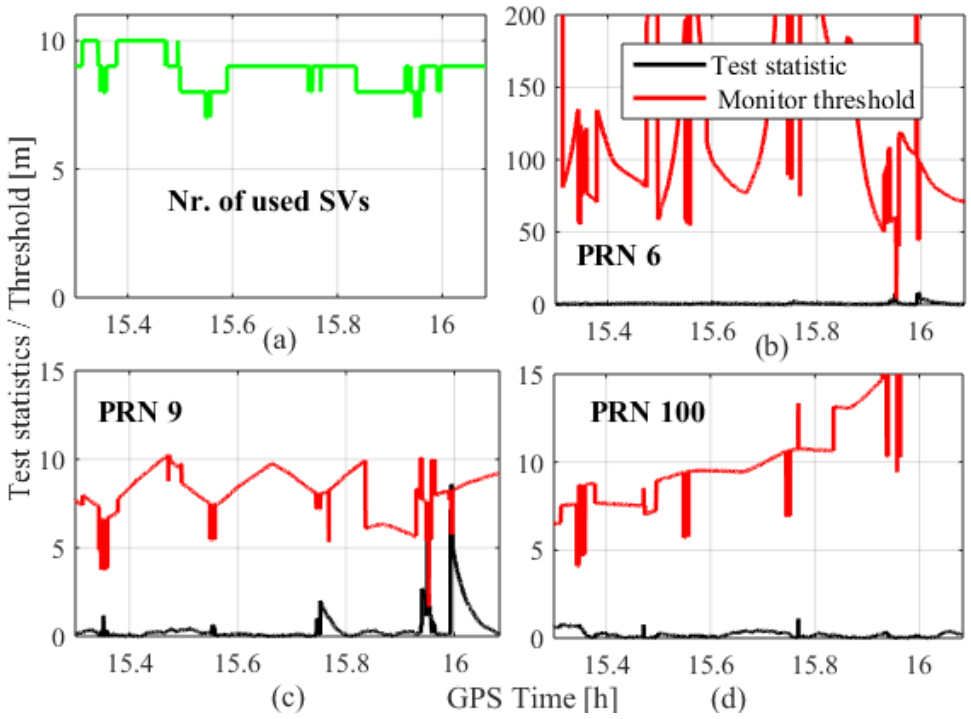

Figure 48 *Test statistic and monitor threshold for three example satellites*

Figure 48 *showed exemplary results for the monitoring condition for a single affected satellite. The case of more than one affected satellites will probably have to be considered for monitoring as well. We therefore also considered the case of two affected satellites, i.e.* $i = 2$ *in Equation* (94).

Figure 49 *shows the minimum over all thresholds for all possible subsets of two affected satellites during the flight test in red, together with the test statistic in black. The solid lines of the monitoring thresholds are using our own experimentally derived characterization of noise in the corrections and airborne measurements, while the dashed lines assume the performance that can be expected from an operational GBAS station with multipath limiting antennas in carefully protected sites and from airborne equipment with a reasonably good airborne antenna performance as presented* [53]. *These models can be considered realistic, while the performance of our own equipment is slightly worse and thus yields conservative results. It can be noted again that the monitoring threshold has sharp drops whenever we lose satellites in turns. At about 15.35h and 15.95h the monitoring threshold even becomes negative and thus of course makes the monitoring completely impossible assuming our own noise models. The black curve is the corresponding test statistic that is regularly exceeding the threshold whenever a drop in the number of used satellites and thus in the monitoring threshold occurs. However, recall that the experimental thresholds in red were derived from the actual measurements during the flight with a maximum of 10 satellites. Looking into the future and simulating complete dual frequency GPS and Galileo constellations with 31 and 27 satellites, respectively, the situation looks very much different. This is shown in the same plot in green. The monitoring threshold now reaches a minimum of 7.8 m at about 15.75h. With two full dual frequency capable constellations the monitoring*

thresholds will be large enough to provide sufficient margin to prevent false alarms due to noise effects for the case of two affected satellites.

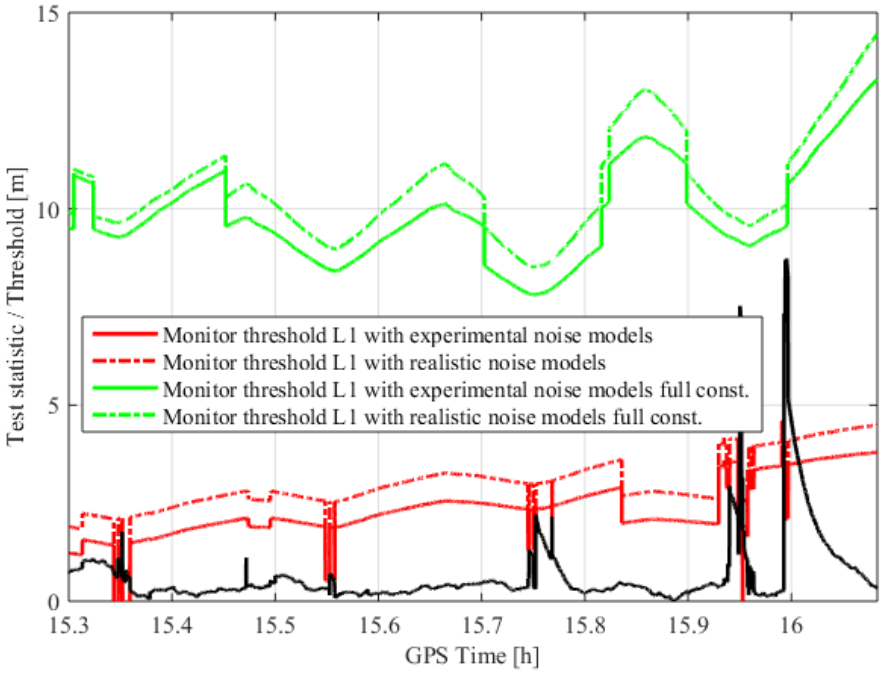

Figure 49 *Monitoring thresholds for the case of two affected satellites with the constellation as seen during the flight trials (red) and simulated full GPS + Galileo constellation (green)*

This concept can be further extended to three and four affected satellites. This of course places a greater burden on the monitoring and yields again decreasing monitoring thresholds. Figure 50 *shows simulated monitoring thresholds for the aircraft positions during the test flight assuming two, three and four affected satellites in black, red and green, respectively. As expected, the monitoring threshold keeps decreasing while more satellites are assumed to be affected.*

But even in the case of four affected satellites the threshold just reaches values of around 4m and thus remains above the threshold for two affected satellites and for the limited constellation we observed during the flight test.

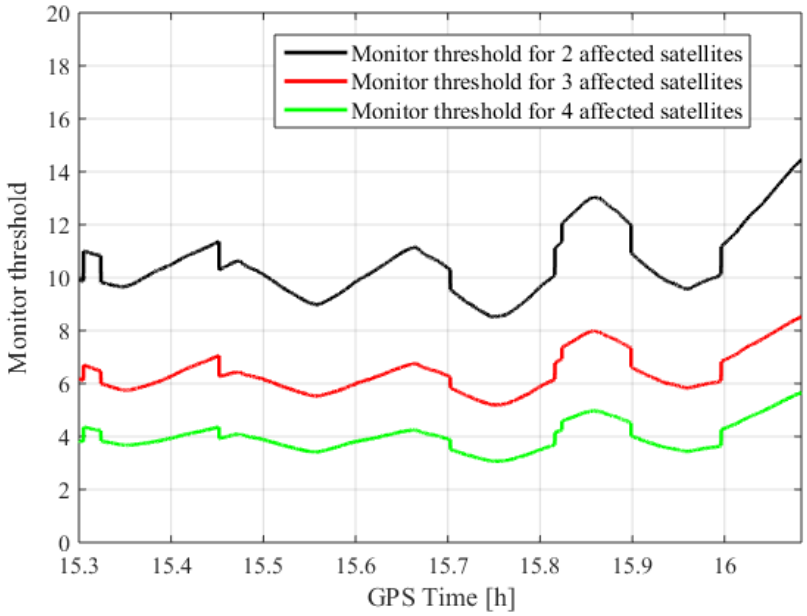

Figure 50 *Monitor thresholds assuming two full dual frequency capable constellations and 2, 3 and 4 simultaneously affected satellites*

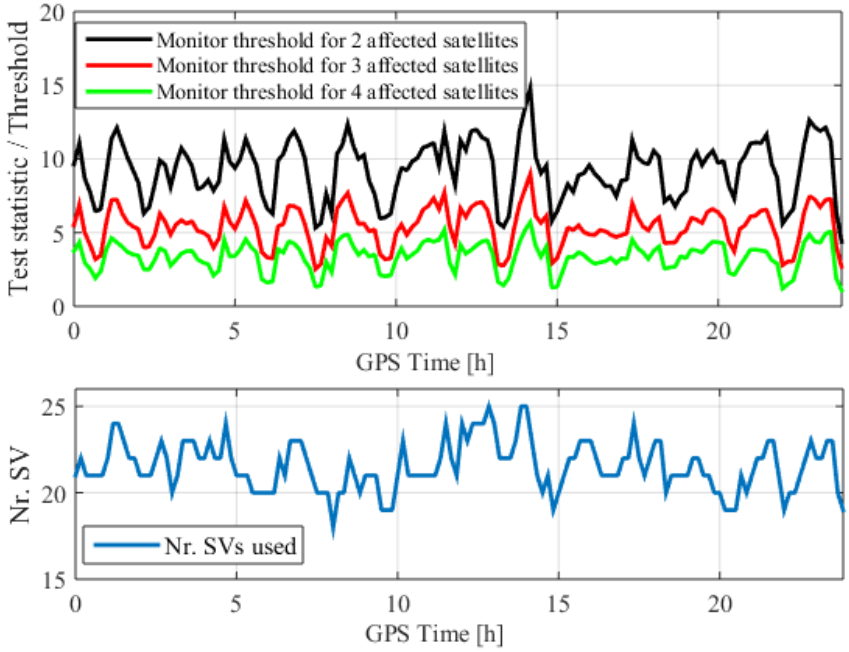

Figure 51 *Monitoring threshold for Troll (Antarctica at 72° Southern Latitude) as example for a location with less favorable satellite geometry and the effect on the monitoring*

Now the results so far only showed an example of a short time period in mid-latitudes with a rather good satellite geometry. For that reason we also examined the effect of the satellite geometry in less favorable locations and chose as example Troll Research Station in Antarctica located at 72° southern latitude. The results are shown in Figure 51. *Due to the lack of high elevation satellites the geometries become weaker in the vertical domain and thus lead to somewhat larger* s_{vert} *values. However, the monitoring for the 2 and 3 affected satellite case still seems to be possible, for the 4 affected case there*

are times, e.g. around midnight, where the threshold is rather small. At all times the threshold remains positive and thus makes the monitoring possible in principle depending on the assumed noise in the measurement." [15]

5.5.4 Discussion of the monitor

The monitor developed and presented in this section provides a robust and effective way of detecting the presence of ionospheric gradients in a future dual frequency GBAS. It leverages the knowledge about the set of used satellites and thus does not make unnecessarily conservative assumptions. This became possible since the monitoring was shifted to the airborne side. A downside of the monitor is the increase in complexity of the airborne processing and the associated increased costs for development and certification of the airborne equipment. An alternative way of mitigating the ionospheric gradient threat is to remove the ionospheric delay in the positioning algorithm by means of forming an ionosphere free combination of the pseudorange measurements. This would result in a decreased nominal positioning performance due to the combination of the noise and multipath on the two frequencies. Furthermore, it would require a complete validation of the signals on the L5/E5a bands for GBAS positioning, while in the concept proposed here the second frequency would only be used for monitoring purposes. It seems thus more likely that the single frequency positioning will be maintained also in the future. In that case, the proposed method will form the core of the ionospheric mitigation strategy.

In this chapter, two ways of reducing the conservatism in the derivation of NSE requirements were developed and discussed. It was shown that by including knowledge available into the system monitoring conditions can be relaxed while maintaining the original level of safety.

6 CONCLUSIONS AND OUTLOOK

6.1 SUMMARY AND CONCLUSIONS

This work was performed in the context of supporting the development and standardization of GBAS as primary guidance system for precision approaches and landings. In order to achieve this, the developments in this work were performed with the aim to take into account as much available knowledge as possible in order to not rely on conservative assumptions. As a side condition, any changes to standard systems should be kept as small as possible in order to maintain compatibility with existing systems as much as possible and ensure that standardization and certification remains possible.

In the beginning, an overview of approach classifications and guidance systems for aircraft is given. A short discussion of the ILS as currently most used technology with a discussion of its issues is followed by a description of GBAS as future guidance system. Based on satellite navigation, it has the potential to provide significantly more flexibility in defining approaches and reducing technical and operational restrictions that limit runway capacity but that are necessary for the ILS. As first original contribution in this thesis, an in-flight comparison of the performance of ILS and GBAS was carried out showing the significant performance improvement and reduction of external influences on the quality of the approach guidance signals.

The next chapter summarizes the requirements for automatic landings and shows how the GBAS requirements for the approach service type D (supporting CAT-III operations) were derived. The main concept is derived from the fact that the aircraft has to land within the predefined touchdown box on the runway. This has to be ensured for the nominal case, when all parameters influencing the touchdown performance vary according to their expected distributions, for the limit case when one parameter is kept at its most adverse value while all others vary nominally, and for the malfunction case when an undetected error occurs. As the requirement to land in the touchdown box is defined at aircraft level, this total error budged needs to be allocated between the autopilot performance and the navigation system performance. This summary is followed by a critical review of the assumptions taken and sug-

gests some changes in order to take into account available knowledge about certain parameters instead of relying on worst-case assumptions. This leads to a potential relaxation of the current ground monitoring requirements and ultimately can improve the availability of GBAS. These suggested changes constitute another original contribution of this work.

As the total system error needs to be allocated between the autopilot and navigation system error budgets, the next chapter focuses on the description and evaluation of the FTE. For the derivation of the current GBAS requirements one nominal touchdown point and one Gaussian distributed dispersion around that point are considered and deemed representative for all aircraft in all loading conditions and wind situations. In this work, after a brief description of the phases of an approach and the autopilot modes an exemplary simulation to evaluate the FTE of a given autopilot model is shown. The influence of different wind scenarios and weight and balance configurations for automatic landings is investigated. It is also shown that applying available knowledge, such as weight and loading conditions of the aircraft on approach, reduces the spread in the touchdown points. This can then be leveraged when deriving the NSE requirements from a given FTE performance. The results of the simulations are also in line with previous studies, showing that the FTE performance cannot in general be assumed to be Gaussian distributed. In the course of this work it is therefore concluded that, instead of just fitting a Gaussian distribution to the data, a different modelling is required in order to not underestimate the risk of landing outside the touchdown box. The methods proposed here in order to achieve this are deriving a Gaussian overbound instead of a Gaussian fit or alternatively, to model the touchdown points by a Johnson distribution that is better suitable to describe skewed data that are typically observed. Using the Gaussian overbound has the advantage that it allows a simple tradeoff between two Gaussian distributed errors (NSE and FTE), but has the disadvantage that it requires a significant amount of conservatism and thus results in unnecessarily stringent NSE requirements. The Johnson modelling has the advantage of appropriate modelling and therefore requiring less conservative assumptions. On the downside, the derivation of requirements needs to be done numerically and it is not possible to derive simple standard requirements for the GBAS monitors. The improved modelling of FTE and the potential changes to the allocation between NSE and FTE budgets are another original contribution developed within the context of this thesis.

The final chapter before these conclusions is dedicated to the GBAS navigation system errors. A brief discussion of the error sources is followed by a description of the problem of ionospheric gradients and the challenges they pose to a differential GNSS architecture like GBAS. For each country where a GBAS is placed, a GBAS threat model needs to be derived. This threat model defines the gradients against which the system has to be robust. For the GAST D an ionospheric gradient monitor will be used that is based on double differenced carrier phase measurements. This monitor faces a variety of challenges and is currently one of the main issues in terms of GBAS availability. In the frame of this work an alternative means of monitoring for ionospheric gradients was developed as another original contribution. The concept is based on an additional monitoring receiver and makes use of the proposed

relaxations due to the use of available knowledge that were identified in chapter 0. It is shown that in that way the monitoring performance can be significantly improved. The second part of this chapter is focused on future GBAS generations that will make use of multiple GNSS constellations and two navigation frequencies. With the use of those dual frequency methods it is possible to estimate and eliminate the ionospheric delay, however, at the price of combining the noise and multipath effects of the two measurements. So while offering robustness against the ionospheric threat the nominal performance is degraded. For that reason it is likely that also in the future positioning will be based on single frequency methods and the second frequency is used only for ionospheric monitoring. In this context a monitoring algorithm for ionospheric gradients between the ground station and the aircraft was developed. The development of this monitoring scheme is the final original contribution of this thesis. It is suggested that the task of monitoring for ionospheric gradients is completely shifted to the airborne system (while for GAST C it is the ground station's responsibility and for GAST D a shared responsibility between ground and airborne systems). In that way when defining the monitoring thresholds all knowledge about the current NSE and potentially also FTE performance can be leveraged such that the monitor does not need to make overly conservative assumptions for many parameters.

The developments in this work can potentially support the development of GBAS and improve system availability. They were orientated at providing solutions that are technically easy to implement and at the same time simple to standardize. An optimal tradeoff between NSE and FTE could be achieved with a tight integration of the autopilot and the GBAS board equipment. From an integration perspective this seems difficult, however, may be an option if operational benefits can be shown to outweigh the necessary effort and definition of interfaces. Finally, the developments for the dual frequency ionospheric monitor are supporting the developments ongoing in and international research effort to develop GBAS to globally reach the same reliability as ILS. Reaching this goal is essential to ultimately replace ILS with GBAS and exploit all the benefits of GNSS-based navigation to cope with the challenge of limited airport capacity for an increasing amount of traffic.

6.2 OUTLOOK

GBAS is currently in an early implementation stage. Thus, there is still great potential to further improve and fine-tune existing service types C and D as operational experience becomes more and more available and potential issues arise. Based on the contributions made in this work, the following further studies about specific aspects are suggested:

- As shown in the contribution described in Section 2.3, GBAS guidance is much smoother and less prone to errors by signal distortions due to preceding aircraft or aircraft on the ground. The smoother guidance on the approach can potentially be leveraged in the design of the autopilot control laws. Not

having to account for the same level of disturbances may result in flare laws that can potentially reduce the dispersion of the touchdown points. Such an improvement can then directly be used for an improved trade-off between the autopilot and navigation system performance.

- In Section 3.4 a review and discussion of the requirement derivation process is given, along with another contribution of this thesis, namely suggestions for improvements in the requirement derivation process for GBAS ground monitors. It was shown that the true value of the GPA for a given approach and a worst projection factor s_{vert} for the set of satellites lead to relaxed monitoring requirements in the ground system. With more GNSS constellations becoming available, it may also be possible to further restrict the VAL for the final approach to smaller numbers and thus enable the ground station to leverage the budget that becomes available for yet less stringent requirements.

- In Chapter 4 the modelling of touchdown performance of aircraft was discussed. In this work, only one aircraft type was studied exemplary. It is certainly of interest to expand this study to a variety of other aircraft and other aerial vehicles that may have significantly different performance characteristics. Furthermore, the simulations in this work were performed based on an autopilot model that did not meet the touchdown requirements. It would be interesting to redo these simulations with higher fidelity models that are more representative of actual autopilot implementations. In order to actually apply the proposed method this study should be extended to obtain touchdown distributions that are highly realistic and cover more aspects than those studied in this work. The simulations may be improved by considering different aircraft configurations and taking into account the changes in the reference approach speed with respect to aircraft mass. Furthermore, especially the radar altimeter that is used for vertical guidance at the final stage of the approach should be properly modeled and included in the simulations. Along with it, studies about the terrain just before the runway and the slope of the runway typically have a significant influence on the touchdown point. All these points were beyond the scope of the example shown in this thesis. They are, however, of great interest for further application of the trade-off between NSE and FTE performance.

- Section 5.4 presented a new monitoring concept for ionospheric gradients in single-frequency GBAS, based on an additional monitoring receiver as far as possible from the other GBAS reference receivers. This concept can be further expanded to use information from other receivers at larger baselines and potentially even external to GBAS. It may be feasible to share the measurements from several GBAS stations within a country or a geographic region. In that way a highly effective monitoring based on reference stations that provide excellent signal quality, are permanently monitored, and are located in secure areas can be achieved.

- Section 5.5 presented the concept for monitoring for ionospheric gradients in a dual frequency GBAS. It was shown that monitoring gets more challenging with an increasing number of satellites that may be affected at the same time. Determination of a monitoring threshold requires a maximum number of satellites that are simultaneously affected by the same ionospheric anomaly. Further long-

term studies about the characteristics of ionospheric anomalies, especially in equatorial regions, about the number of impacted satellites need to be carried out to determine this number. As this concept was developed theoretically and tested only in simulations, the method should then be tested under real ionospheric disturbance scenarios to validate the theoretical performance.

On a more general perspective on GBAS, there still are many interesting areas and topics open for research, ranging from the development of a full concept of operations for dual frequency and multi constellation primary and fallback modes along with the required integrity concepts to the potential to use higher capacity and secure data transmission schemes. After the technical development, it is essential to also demonstrate and leverage operational improvements (e.g. for noise abatement, fuel savings, or capacity improvements) to no just create a system that provides the same service as ILS but actually provides benefits to its operators and users.

LITERATURE

[1] European Commission, *Flightpath 2050 Europes Vision for Aviation,* 2011.

[2] Federal Aviation Administrtion (FAA), "FAA Aerospace Forecast Fiscal Year 2017-2037," 2017.

[3] International Civil Aviation Organization (ICAO), *Proposed Amendment to Annex 10, Volume I,* 2016.

[4] International Civil Aviation Organization (ICAO), *ICAO Annex 10 - Aeronautical Telecommunications,* 2014.

[5] C. A. Shively and R. Niles, "Safety Concepts for Mitigation of Ionospheric Anomaly Errors in GBAS," in *Proc. ION NTM,* San Diego, CA, USA, 2008.

[6] W. Schuster and W. Ochieng, "Harmonisation of Category-III Precision Approach Navigation System Performance Requirements," *Journal of Navigation,* vol. 63, no. 4, pp. 569-589, 10 2010.

[7] M. Felux, T. Dautermann and H. Becker, "GBAS landing system - percision approach guidance after ILS," *Aircraft Engineering and Aerospace Technology,* vol. 85, no. 5, pp. 382-388, 2013.

[8] M.-S. Jeong, J. Bae, H.-S. Jun and Y. J. Lee, "Flight test evaluation of ILS and GBAS performance at Gimpo International Airport," *GPS solutions,* vol. 20, no. 3, pp. 473-483, 2016.

[9] European Aviation Safety Agency (EASA), *Certification Specifications for All-Weather Operations,* CS-AWO, 2003.

[10] Federal Aviation Administrtion (FAA), *Criteria for Approval of Category III Weather Minima for Takeoff, Landing, and Rollout,* AC 120-28D, 1999.

[11] A. Shakarian, "Application of Monte-Carlo Techniques to the 757/767 Autoland Dispersion Analysis by Simulation," in *Proc. AIAA Guidance and Control Conf.*, Gatlinburg, TN, USA, 1983.

[12] B. Belabbas, T. Dautermann, G. Looye and J. Kladetzke, "GBAS based autoland system: A bottom up approach for GAST-D requirements," in *Proc. IEEE/ION PLANS,* Indian Wells, CA, USA, 2010.

[13] J. Burns, B. Clark, R. Cassell, C. Shively, T. Murphy and M. Harris, "Conceptual Framework for the Proposal for GBAS to Support CAT III Operations," ICAO NSP WGW WP11, Montréal, CA, 2009.

[14] M. Felux, J. Lee and F. Holzapfel, "GBAS ground monitoring requirements from an airworthiness perspective," *GPS Solutions,* vol. 19, no. 3, pp. 393-401, 7 2014.

[15] M. Felux, M.-S. Circiu, J. Lee and F. Holzapfel, "Ionospheric Gradient Threat Mitigation in

Future Dual Frequency GBAS," *International Journal of Aerospace Engineering*, vol. 2017, pp. 1-10, 2017.

[16] M. Felux, T. Dautermann and H. Becker, "GBAS Approach Guidance Performance - A Comparison to ILS," in *Proc. ION ITM*, Newport Beach, CA, USA, 2013.

[17] International Civil Aviation Organization (ICAO), *Aircraft Operations, Volume I, Flight Procedures*, 2006.

[18] International Civil Aviation Organization (ICAO), *ICAO Annex 6 - Operation of Aircraft*, 2013.

[19] International Civil Aviation Organization (ICAO), *ICAO Annex 14 - Aerodromes*, 2014.

[20] International Civil Aviation Organization (ICAO), *ICAO State Letter on Approach Classifications*, 2012.

[21] German Federal Bureau of Aircraft Accident Investigation (BFU), "Bulletin - Status Report," pp. 24-36, November 2011.

[22] "AviationSafety Network - Accident report," [Online]. Available: http://aviation-safety.net/database/record.php?id=19880102-1&lang=en. [Accessed 31 August 2017].

[23] Civil Aviation Authority of New Zealand, "NZ 60 'Erroneous' Glideslope Capture, Autocoupled Approach and Go-Around," Incident Report 00/2518 B767-319ER ZK-NCJ, 2002.

[24] Bureau d'Enquêtes et d'Analyses pour la sécurité de l'aviation civile (BEA), "Approach above glide path, interception of ILS sidelobe signal, increase in pitch angle commanded by autopilot," Serious Incident Report F-ZU120313E, 2013.

[25] Federal Aviation Administrtion (FAA), *Siting Order for Ground Based Augmenation System (GBAS)*, Order 8664.1, 2010.

[26] B. Pervan, S. Pullen and I. Sayim, "Sigma estimation, inflation, and monitoring in the LAAS ground system," in *Proc. ION GPS*, Portland, OR, USA, 2000.

[27] J. Lee, S. Pullen, G. Xie and P. Enge, "LAAS sigma-mean monitor analysis and failure-test verification," in *Proc. ION GNSS*, Salt Lake City, UT, USA, 2001.

[28] P. Truffer, "skyguide GBAS status report," in *LATO Meeting*, Brétigny-sur-Orge, France, 2013.

[29] S. Pullen, G. Gao, C. Tedeschi and J. Warburton, "The Impact of Uninformed RF Interference on GBAS and Potential Mitigations," in *Proc. ION ITM*, Newport Beach, CA, USA, 2012.

[30] J. Warburton and C. Tedeschi, "GPS privacy jammers and RFI at Newark: Navigation team AJP-652 results," in *12th Int'l. GBAS Working Group Meeting* , Atlantic City, NJ, USA, 2011.

[31] D. Guenter and J. Dennis, "Initial operational experience with CAT I ground based augmentation system (GBAS)," in *Proc. ICNS*, Herdon, VA, USA, 2015.

[32] S. Khanafseh, F. Yang, B. Pervan, S. Pullen and J. Warburton, "Carrier Phase Ionospheric Gradient Ground Monitor for GBAS with Experimental Validation," in *Proc. ION GNSS*, Portland, OR, USA, 2010.

[33] B. Belabbas and M. Meurer, "Carrier Phase and Code Based Absolute Slant Ionosphere Gradient Monitor for GBAS," in *Proc. ION GNSS*, Nashville, TN, USA, 2012.

[34] R. R. Hatch, "The synergism of GPS code and carrier measurements," in *Proc. Third Int. Geodetic Symp. Satellite Doppler Positioning*, 1982.

[35] EUROCAE, *Minimum Operational Performance Specification for Global Navigation Satellite Ground Based Augmentation System Ground Equipment to Support Category I Operations*, ED-114A, 2013.

[36] Federal Aviation Administrtion (FAA), *Category I Local Area Augmenation System Ground Facility - NON-FED Specification*, FAA-E-AJW44-2937A, 2005.

[37] M. Felux, M. S. Circiu, B. Belabbas, M. Meurer, M. Stanisak, C. Milner, Y. Jiang, A. Guilbert and A. Philipp, "Concept for a Dual Frequency Dual Constellation GBAS," in *Proc. ION GNSS+*, Tampa, FL, USA, 2015.

[38] RTCA, *Minimum Operational Performance Standards for GPS Local Area Augmentation System Airborne Equipment*, DO-253C, 2009.

[39] RTCA, *GNSS-Based Precision Approach Local Area Augmentation System (LAAS) Signal-In-Space Interface Control Document (ICD)*, DO-246D, 2008.

[40] L. Gratton, B. Pervan and S. Pullen, “Orbit Ephemeris Monitors for Category 1 LAAS,” in *Proc. IEEE PLANS*, Monterey, CA, USA, 2004.

[41] T. A. Skidmore and F. Graas, "An Investigation of Tropospheric Errors On Differential GNSS Accuracy and Integrity," in *Proc. ION GNSS*, Long Beach, CA, USA, 2004.

[42] J. Christie, P.-Y. Ko, B. Pervan, P. Enge, J. D. Powell and B. Parkinson, "Analytical and Experimental Observations of Ionospheric and Tropospheric Decorrelation Effects for Differential Satellite Navigation during Precision Approach," in *Proc. ION GPS*, Nashville, TN, USA, 1998.

[43] S. Pullen, Y. S. Park and P. Enge, "Impact and mitigation of ionospheric anomalies on ground-based augmentation of GNSS," *Radio Science*, vol. 44, no. 1, 2009.

[44] C. Mayer, B. Belabbas, T. Pannowitsch, N. Jakowski, M. Meurer, W. Dunkel and O. Weber, "Ionosphere Threat Space Model Assessment for GBAS," in *Proc. ION GNSS*, Savannah, GA, USA, 2009.

[45] M. Kim, Y. Choi, H.-S. Jun and J. Lee, "GBAS ionospheric threat model assessment for category I operation in the Korean region," *GPS Solutions*, vol. 19, no. 3, pp. 443-459, 2015.

[46] Global Positioning Systems Directorate, Systems Engineering & Integration, *Interface Specification, Navstar GPS Space Segment/Navigation User Interfaces*, IS-GPS-200H, 2013.

[47] P. Misra and P. Enge, Global Positioning System, Lincoln, MA, USA: Ganga-Jamuna Press, 2006.

[48] T. Murphy, M. Harris and S. Beauchamp, "Implications of 30-Second Smoothing for GBAS Approach Service Type D," in *Proc. ION ITM*, San Diego, CA, USA, 2010.

[49] M. Felux, T. Dautermann and B. Belabbas, "Towards Full GAST-D Capability - Flight testing DLR's Experimental GBAS Station," in *Proc. ION ITM*, Newport Beach, CA, USA, 2012.

[50] H. Konno, *Design of an aircraft landing system using dual-frequency GNSS*, Ph.D. dissertation, Dept. Aero. Astro., Stanford Univ., Palo Alto, CA, USA, 2007.

[51] M.-S. Circiu, M. Felux, P. Remi, L. Yi, B. Belabbas and S. Pullen, "Evaluation of Dual Frequency GBAS Performance using Flight Data," in *Proc. ION ITM*, San Diego, CA, USA, 2014.

[52] M.-S. Circiu, M. Felux, B. Belabbas, M. Meurer, J. Lee, M. Kim and S. Pullen, "Evaluation of GPS L5, Galileo E1 and Galileo E5a Performance in Flight Trials for Multi Frequency Multi Constellation GBAS," in *Proc. ION GNSS+*, Tampa, FL, USA, 2015.

[53] D. Gerbeth, M.-S. Circiu, M. Caamano and M. Felux, "Nominal Performance of Future Dual Frequency Dual Constellation GBAS," *International Journal of Aerospace Engineering*, vol. 2016, pp. 1-20, 2016.

[54] J. Lee, M. Luo, S. Pullen, Y. S. Park, P. Enge and M. Brenner, "Position-Domain Geometry Screening to Maximize LAAS Availability in the Presence of Ionosphere Anomalies," in *Proc. ION GNSS*, Fort Worth, TX, USA, 2006.

[55] M. Harris and T. Murphy, "Putting the Standardized GBAS Ionospheric Anomaly Monitors to the Test," in *Proc. ION GNSS*, Savannah, GA, USA, 2009.

[56] S. Beauchamp, S. Casler, L. Almeida and M. Brenner, "Airborne DSIGMA Range Monitor Performance Validation Update," in *WP6 of the ICAO NSP GWG/1*, Montréal, QC, Canada, 2016.

[57] M.-S. Circiu, M. Felux, D. Gerbeth, M. Caamano and M. Meurer, “Assessment of Different Dual-frequency Dual-constellation GBAS Processing Modes based on Flight Trials,” in *Proc. ION GNSS+*, Portland, OR, USA, 2016.

[58] S. Thoelert, M. Vergara, M. Sgammini, C. Enneking, F. Antreich, M. Meurer, D. Brocard and C. Rodriguez, "Characterization of nominal signal distortions and impact on receiver performance for GPS (IIF) L5 and Galileo (IOV) E1/E5a signals," in *Proc. ION GNSS+*, Tampa, FL, USA, 2014.

[59] Federal Aviation Administrtion (FAA), *Determination of Instrument Landing System (ILS) Glidepath Angle, Reference Datum Heights (RDH)*, Order 8240.47D, 2015.

[60] J. Bredemeyer, T. Kleinmann and H. Kraemer, "ILS interference measurements and dynamic receiver behaviour," in *Proc. 14th Int. Flight Inspection Symp.*, Toulouse, France, 2006.

[61] European Aviation Safety Agency (EASA), *Certificaion Specifications for Large Aeroplanes*, CS-25, 2010.

[62] B. Clark and B. DeCleene, "Alert Limits: Do we Need Them for CAT III?," in *Proc. ION GNSS*, Fort Worth, TX, USA, 2006.

[63] Boeing Commercial Airplanes, "Volume I: GBAS CAT II Requirements Development Research Program Overview and Summary of Results," D6-83447-1, 2005.

[64] RTCA, *Minimum Performance Standrads Airborne Low-Range Radar Altimeters*, DO-155, 1974.

[65] P. Spiegel, B. Braun, J. Dambeck and F. Holzapfel, "Altimeter Slant Range Analysis and Compensation," in *Proc. ION ITM*, San Diego, CA, USA, 2014.

[66] M. Altenscheidt, "Private conversation with Mark Altenscheidt, Chief of Boeing Fleet Air Berlin, Captain on B737-800," September 2010.

[67] U. S. Department of Defence, "Flying Qualities of Piloted Aircraft," MIL-HDBK-1797, 1997.

[68] F. J. Massey, "The Kolmogorov-Smirnov Test for Goodness of Fit," *Journal of the American Statistical Association,* vol. 46, no. 253, pp. 68-78, March 1951.

[69] T. W. Anderson and D. A. Darling, “A test of goodness of fit,” *Journal of the American statistical association,* vol. 49, no. 268, pp. 765-769, 1954.

[70] B. S. Levy, P. Som and R. Greenshaw, "Analysis of Flight Technical Error on Straight, Final Approach Segments," Mitre Corp., Bedford, MA, USA, 2006.

[71] N. L. Johnson, "Systems of frequency curves generated by methods of translation," *Biometrika,* vol. 36, no. 1-2, pp. 149-176, 1949.

[72] D. L. Jones, *Johnson Curve Toolbox for Matlab: analysis of non-normal data using the Johnson family of distributions,* Univ. Southern Florida, 2014.

[73] Airbus, "A318/A319/A320/A321 Flight Crew Operating Manual," 2012.

[74] "Ogimet," [Online]. Available: http://www.ogimet.com/metars.phtml.en. [Accessed 12 July 2016].

[75] G. Looye and H.-D. Joos, "Design of autoland controller functions with multiobjective optimization," *Journal of guidance, control, and dynamics,* vol. 29, no. 2, pp. 475-484, 2006.

[76] M. Felux, J. Lee und F. Holzapfel, „Total System Performance for GBAS based Automatic Landings,“ in *Proc. Pacific PNT*, Honolulu, HI, USA, 2015.

[77] M. Felux, M.-S. Circiu, D. Gerbeth and M. Caamano, "Ionospheric Monitoring in a Dual Frequency GBAS," in *Proc. IEEE Aerospace Conference*, Big Sky, MT, USA, 2016.

[78] M. Felux, M.-S. Circiu, D. Gerbeth and M. Caamano, "Experimental Validation of an Ionospheric Monitoring Scheme for Dual Frequency GBAS," in *Proc. ION GNSS+*, Portland, OR, USA, 2016.

[79] S. Jung and J. Lee, "Long-term ionospheric anomaly monitoring for ground based augmentation systems," *Radio Science,* vol. 47, no. 4, 7 2012.

[80] M. Yoon, J. Lee, S. Pullen, J. Gillespie, N. Mathur, R. Cole, J. R. Souza, P. Doherty and R. Pradipta, "Equatorial Plasma Bubble Threat Parameterization to Support GBAS Operations in the Brazilian Region," *Navigation,* vol. 64, no. 3, pp. 309-321, 9 2017.

[81] S. Saito, S. Sunda, J. Lee, S. Pullen, S. Supriadi, T. Yoshihara, M. Terkildsen and F. Lecat, "Ionospheric delay gradient model for GBAS in the Asia-Pacific region," *GPS Solutions,* vol. 21, no. 4, pp. 1937-1947, 01 October 2017.

[82] J. McDonald, D. Weed and B. Johnson, "Observed Nominal Atmospheric Behavior Using

Honeywell’s GAST D Ionosphere Gradient Monitor," ICAO NSP/WGW WP16, Montréal, QC, Canada, 2014.

[83] T. Dautermann, M. Felux and A. Grosch, "Approach service type D evaluation of the DLR GBAS testbed," *GPS Solutions*, vol. 16, no. 3, pp. 375-387, 2012.

[84] M.-S. Circiu, M. Felux, S. Thoelert, F. Antreich, M. Vergara, M. Sgammini, C. Enneking and S. Pullen, "Evaluation of GPS L5 and Galileo E1 and E5a Performance for Future Multi Frequency and Multi Constellation GBAS," in *Proc. ION ITM*, Dana Point, CA, USA, 2015.

APPENDIX I – GBAS PERFORMANCE REQUIREMENTS

In this appendix the most important GBAS performance requirements are reproduced from the ICAO Annex 10 GBAS standards and recommended practices (Table 3.7.2.4-1 in [4]).

Typical operation	Accuracy horizontal 95% (Notes 1 and 3)	Accuracy vertical 95% (Notes 1 and 3)	Integrity (Note 2)	Time-to-alert (Note 3)	Continuity (Note 4)	Availability (Note 5)
En-route	3.7 km (2.0 NM)	N/A	$1 - 1 \times 10^{-7}$/h	5 min	$1 - 1 \times 10^{-4}$/h to $1 - 1 \times 10^{-8}$/h	0.99 to 0.99999
En-route, Terminal	0.74 km (0.4 NM)	N/A	$1 - 1 \times 10^{-7}$/h	15 s	$1 - 1 \times 10^{-4}$/h to $1 - 1 \times 10^{-8}$/h	0.99 to 0.99999
Initial approach, Intermediate approach, Non-precision approach (NPA), Departure	220 m (720 ft)	N/A	$1 - 1 \times 10^{-7}$/h	10 s	$1 - 1 \times 10^{-4}$/h to $1 - 1 \times 10^{-8}$/h	0.99 to 0.99999
Approach operations with vertical guidance (APV-I)	16.0 m (52 ft)	20 m (66 ft)	$1 - 2 \times 10^{-7}$ in any approach	10 s	$1 - 8 \times 10^{-6}$ per 15 s	0.99 to 0.99999
Approach operations with vertical guidance (APV-II)	16.0 m (52 ft)	8.0 m (26 ft)	$1 - 2 \times 10^{-7}$ in any approach	6 s	$1 - 8 \times 10^{-6}$ per 15 s	0.99 to 0.99999
Category I precision approach (Note 7)	16.0 m (52 ft)	6.0 m to 4.0 m (20 ft to 13 ft) (Note 6)	$1 - 2 \times 10^{-7}$ in any approach	6 s	$1 - 8 \times 10^{-6}$ per 15 s	0.99 to 0.99999

NOTES.—

1. The 95th percentile values for GNSS position errors are those required for the intended operation at the lowest height above threshold (HAT), if applicable. Detailed requirements are specified in Appendix B and guidance material is given in Attachment D, 3.2.

2. The definition of the integrity requirement includes an alert limit against which the requirement can be assessed. For Category I precision approach, a vertical alert limit (VAL) greater than 10 m for a specific system design may only be used if a system-specific safety analysis has been completed. Further guidance on the alert limits is provided in Attachment D, 3.3.6 to 3.3.10. These alert limits are:

Typical operation	Horizontal alert limit	Vertical alert limit
En-route (oceanic/continental low density)	7.4 km (4 NM)	N/A
En-route (continental)	3.7 km (2 NM)	N/A
En-route, Terminal	1.85 km (1 NM)	N/A
NPA	556 m (0.3 NM)	N/A
APV-I	40 m (130 ft)	50 m (164 ft)
APV- II	40 m (130 ft)	20.0 m (66 ft)
Category I precision approach	40 m (130 ft)	35.0 m to 10.0 m (115 ft to 33 ft)

3. The accuracy and time-to-alert requirements include the nominal performance of a fault-free receiver.

4. Ranges of values are given for the continuity requirement for en-route, terminal, initial approach, NPA and departure operations, as this requirement is dependent upon several factors including the intended operation, traffic density, complexity of airspace and availability of alternative navigation aids. The lower value given is the minimum requirement for areas with low traffic density and airspace complexity. The higher value given is appropriate for areas with high traffic density and airspace complexity (see Attachment D, 3.4.2). Continuity requirements for APV and Category I operations apply to the average risk (over time) of loss of service, normalized to a 15-second exposure time (see Attachment D, 3.4.3).

5. A range of values is given for the availability requirements as these requirements are dependent upon the operational need which is based upon several factors including the frequency of operations, weather environments, the size and duration of the outages, availability of alternate navigation aids, radar coverage, traffic density and reversionary operational procedures. The lower values given are the minimum availabilities for which a system is considered to be practical but are not adequate to replace non-GNSS navigation aids. For en-route navigation, the higher values given are adequate for GNSS to be the only navigation aid provided in an area. For approach and departure, the higher values given are based upon the availability requirements at airports with a large amount of traffic assuming that operations to or from multiple runways are affected but reversionary operational procedures ensure the safety of the operation (see Attachment D, 3.5).

6. A range of values is specified for Category I precision approach. The 4.0 m (13 feet) requirement is based upon ILS specifications and represents a conservative derivation from these specifications (see Attachment D, 3.2.7).

7. GNSS performance requirements intended to support Category II and III precision approach operations necessitate lower level requirements in the technical appendix (Appendix B, section 3.6) to be applied in addition to these signal in space requirements (see Attachment D, 7.5.1).

8. The terms APV-I and APV-II refer to two levels of GNSS approach and landing operations with vertical guidance (APV) and these terms are not necessarily intended to be used operationally.

The following tables summarize the maximum alert limits in the final approach segment for the lateral (FASLAL) and vertical (FASVAL) domains. They are reproduced from the RTCA DO-253C document "Minimum operational performance requirements for GPS local area augmentation system airborne equipment" (tables 2-14 and 2-15 from [38]).

Lateral alert limit (m)	Horizontal distance of aircraft position to the LTP/FTP (D in m)
FASLAL	$0 \leq D \leq 873$
$0.44 \cdot D$ + FASLAL-3.85	$873 < D \leq 7500$
FASLAL+29.15	$D > 7500$

Vertical alert limit (m)	H_p (Product of sin(GPA) and the slant range distance from the aircraft position to GPIP (m)
FASVAL	$H_p \leq 60.96$
$0.095965 \cdot H_p$ + FASVAL – 5.85	$60.96 < H_p \leq 408.432$
FASVAL + 33.35	$H_p > 408.432$

APPENDIX II – COMMON BIAS PROJECTION INTO THE CLOCK

A common bias on all measurements maps only into the receiver clock, not into the position. This can be shown by examining the measurement model

$$\rho = H \cdot \begin{pmatrix} x \\ y \\ z \\ t \end{pmatrix} + \eta$$

where ρ is the nx1-dimensional pseudorange measurement vector, x, y, z the 3-dimensional position and t the receiver clock estimate, η an nx1-dimensional noise and error term and H the nx4-dimensional geometry matrix with the geometric unit row vectors between satellites and user position and a "1" in the fourth column for the receiver clock. Now let ρ_1 and ρ_2 be two measurement vectors with $\rho_1 = \rho_2 + k \cdot \begin{pmatrix} 1 \\ \vdots \\ 1 \end{pmatrix}$.

Then $\rho_1 = H \cdot \begin{pmatrix} x \\ y \\ z \\ t \end{pmatrix} + \eta$ and $\rho_2 = H \cdot \begin{pmatrix} \tilde{x} \\ \tilde{y} \\ \tilde{z} \\ \tilde{t} \end{pmatrix} + \eta$. Subtracting those two equations from one another yields

$$0 = H \cdot \begin{pmatrix} x - \tilde{x} \\ y - \tilde{y} \\ z - \tilde{z} \\ t - \tilde{t} \end{pmatrix} + k \cdot \begin{pmatrix} 1 \\ \vdots \\ 1 \end{pmatrix}.$$

Since H has full column rank (rk(H)=4) it is per definition impossible to make a linear combination of the first three columns adding up to the fourth column. Since $H(:,4) = \begin{pmatrix} 1 \\ \vdots \\ 1 \end{pmatrix}$ it is necessary that $(x - \tilde{x}) = (y - \tilde{y}) = (z - \tilde{z}) = 0$. This implies that position [x, y, z] is not changed if a common bias on all measurements is added.